Switchable photovoltaic properties in ferroelectric PZT thin films

Propriétés photovoltaïques commutables dans des couches minces ferroélectriques de PZT

Thèse de doctorat de l'université Paris-Saclay

École doctorale n° 575 : electrical, optical, bio : physics and engineering (EOBE)
Spécialité de doctorat : Electronique et Optoélectronique, Nano- et Microtechnologies
Graduate School : Sciences de l'ingénierie et des systèmes. Référent : Faculté des sciences d'Orsay

Thèse préparée au **Centre de Nanosciences et de Nanotechnologies, (**CNRS/Université Paris-Saclay), sous la direction de **Philippe LECOEUR**, Professeur, et le co-encadrement de **Sylvia MATZEN**, Maître de conférences

Thèse soutenue à Paris-Saclay, le 21 Mars 2022, par

Komalika RANI

Composition du Jury

Laurent DANIEL Professeur des universités, Université Paris-Saclay (GeePs)	Président
Houssny BOUYANFIF Maître de conférences-HDR, Université de Picardie (LPMC)	Rapporteur & Examinateur
Bohdan KUNDYS Chargé de recherche-HDR Université de Strasbourg, CNRS (IPCMS)	Rapporteur & Examinateur
Maryline GUILLOUX-VIRY Professeur des universités, Université de Rennes 1 (ISCR)	Examinatrice
Hélène MAGNAN Ingénieure de recherche CEA (SPEC)	Examinatrice
Philippe LECOEUR Professeur, Université Paris-Saclay (C2N)	Directeur de thèse

THÈSE DE DOCTORAT

NNT : 2022UPAST047

DOCTORAL SCHOOL
Electrical, Optical, Bio:
Physics and Engineering
(EOBE)

Titre : Propriétés photovoltaïques commutables dans des couches minces ferroélectriques de PZT

Mots clés : ferroélectrique, film mince, dispositif, photovoltaïque, oxyde

Résumé : Les films minces ferroélectriques (FE) sont largement étudiés pour leur application possible dans le domaine du photovoltaïque (PV). Ils sont particulièrement prometteurs pour des applications PV en raison de leur tension photoinduite élevée en circuit ouvert et de leur effet photovoltaïque commutable. Théoriquement, une commutation à 100 % du photocourant peut être obtenue en faisant varier la direction de la polarisation ferroélectrique à travers la couche ferroélectrique. Ceci est particulièrement intéressant pour des applications telles que les mémoires photo-ferroélectriques. La commutation du photocourant dans les films ferroélectriques intégrés entre électrodes n'est cependant pas toujours atteinte en raison de paramètres extrinsèques tels que la nature de l'interface électrode-ferroélectrique (contact Schottky) ou la présence de défauts chargés non mobiles dans le film ferroélectrique. De plus, le mouvement de défauts chargés, tels que des lacunes d'oxygène, sous l'influence des champs électriques appliqués peut également avoir un effet sur le photocourant commutable. Il n'est pas facile de distinguer toutes ces contributions (polarisation, interfaces, défauts) sur la réponse photovoltaïque des dispositifs ferroélectriques, et on sait peu de choses sur le lien quantitatif entre photocourant et polarisation ferroélectrique.

Dans ce travail, une étude approfondie de la commutation des propriétés PV des films minces épitaxiés de titanate-zirconate de plomb Pb(Zr,Ti)O3 (PZT) a été réalisée afin d'étudier quantitativement le rôle de la polarisation ferroélectrique. Des films de PZT de 100 nm d'épaisseur ont été élaborés par ablation laser pulsé (PLD) et intégrés dans une géométrie de condensateur entre électrodes inférieure et supérieure. Le courant photoinduit dans les dispositifs PZT a été mesuré sous éclairage UV (énergie au-dessus de la bande interdite du PZT) et dans différents états de polarisation en soumettant les dispositifs à des champs électriques croissants afin d'obtenir des états électriques distincts tout en mesurant simultanément leur valeur de polarisation. Une étude comparative de différentes interfaces a également été réalisée, incluant Pt et ITO comme électrodes supérieures, SrRuO3 (SRO) et LaSrMnO3 comme électrodes inférieures, ainsi que l'insertion d'une couche diélectrique de SrTiO3 à l'interface PZT/électrode. Ce travail a fourni une détermination quantitative des parties commutables et non commutables du photocourant. Plus précisément, l'étude de la dépendance du photocourant en fonction de la polarisation rémanente commandée électriquement a montré que (1) le photocourant dépend linéairement de la partie commutable de la polarisation ferroélectrique et que (2) l'analyse de cette dépendance permet d'extraire quantitativement la valeur de polarisation non commutable dans la couche FE. Une telle polarisation affecte fortement la commutation des propriétés PV dans les FE et est par ailleurs assez difficile à sonder par les caractérisations ferroélectriques classiques. De plus, l'étude comparative de différentes interfaces a également révélé la contribution de l'interface électrode-ferroélectrique sur les propriétés PV, ce qui peut induire des commutation et amplitude de photocourants très différentes.

En conclusion, ces résultats sont donc particulièrement intéressants pour l'optimisation des films minces FE afin d'obtenir des propriétés PV commutables, ce qui pourrait avoir de fortes implications pour les futures applications de mémoire photo-ferroélectrique. De plus, la méthode développée d'étude de la commutation des photocourants fournit des informations importantes sur le comportement ferroélectrique dans tous les types de couches ferroélectriques, dans lesquelles la polarisation non commutable pourrait être importante mais difficile à étudier autrement.

Title : Switchable photovoltaic properties in ferroelectric PZT thin films

Keywords : ferroelectric, thin film, device, photovoltaic, oxide

Abstract : Ferroelectric (FE) thin films are being explored for their possible use in photovoltaic (PV) applications. This is due to their high open-circuit voltage and switchable photovoltaic effect, which make them attractive for PV applications. Theoretically, 100% switching of the photocurrent can be achieved by varying the direction of the ferroelectric polarization through the ferroelectric layer. This is particularly intriguing for applications such as photo-ferroelectric memory. The presence of switchability in integrated ferroelectric films between electrodes, however, is not always achieved due to extrinsic parameters such as the nature of the electrode-ferroelectric interface (Schottky contact) or the presence of non-mobile charged defects in the ferroelectric film. In addition, the movement of charged defects, such as oxygen vacancies, under the influence of applied electric fields can have an effect on switchable photocurrent as well. It is not an easy process to disentangle all these contributions (polarization, interfaces, defects) to the photovoltaic properties of ferroelectric devices, and little is known about the quantitative link between photocurrent and ferroelectric polarization.

In this work, a thorough investigation of the switchability of the PV properties of epitaxial lead zirconate titanate Pb(Zr,Ti)O3 (PZT) thin films has been carried out in order to study quantitatively the role of ferroelectric polarization. 100 nm thick PZT films were grown using pulsed laser deposition (PLD) and integrated into a capacitor geometry between bottom and top electrodes. The photoinduced current in the PZT devices was investigated under UV illumination (above the PZT band gap) and in different polarization states by poling the devices under increasing electric fields in order to achieve distinct electrical states while simultaneously monitoring their polarization value. A comparison study of different interfaces was also carried out, including Pt and ITO as top electrodes, SrRuO3 (SRO) and LaSrMnO3 as bottom electrodes, as well as the insertion of SrTiO3 dielectric layer at the PZT/electrode interface. This work has provided a quantitative determination of the switchable vs unswitchable parts of photocurrent. More precisely, the study of the dependence of the photocurrent as function of electrically controlled remanent polarization has shown that (1) the photocurrent depends linearly on the switchable part of the ferroelectric polarization and that (2) the analysis of this dependence allows extracting quantitatively the pinned polarization value in the FE layer. Such pinned polarization strongly affects the switchability of the PV properties in FEs and is otherwise rather difficult to probe by classical FE characterizations. In addition, the comparison study of different interfaces also revealed the contribution from the electrode-ferroelectric interface on the PV properties, which can induce different switchability and amplitude of photocurrents.

In conclusion, these results are thus particularly relevant for the optimization of FE thin films to achieve switchable PV properties which could have far-reaching implications for future photo-ferroelectric memory applications. In addition, the developed method of investigation of photocurrents switchability provides important insights on the ferroelectric behavior in all types of ferroelectric layers, in which pinned polarization could be significant but difficult to investigate otherwise.

Acknowledgment

This is a teamwork that we witnessed in the form of a manuscript. And I would like to acknowledge all of them.

It would have not been possible to write this doctoral thesis without the assistance and immense support of the OXIDE team, Materials department at C2N. I would like to express my sincere appreciation to Dr. Philippe Lecoeur for supporting this thesis as a thesis director. Thank you for providing me with all the resources and for the continuous motivation.

I would like to convey heartfelt gratitude towards my co-supervisor Dr. Sylvia Matzen, for her patience, unwavering support, encouragement, constant drive, being available to share deep knowledge through discussions whenever and wherever feasible. I was so fortunate to have Dr. Sylvia Matzen as my supervisor. She was there for boosting me from every single failure and trust me with this project. She is so organized and dedicated researcher, also a bronze medalist CNRS 2021. She has taught me a great deal. She always told me "You can do this". I always cherish going every day to the laboratory with her in her car and sharing everything I feel like. She is the best as a person and supervisor. I would like to stay in touch for life, personally and professionally.

Also, a big thanks to our coolest researcher Dr. Thomas Maroutian for the scientific discussions, sharing his technical knowledge about PLD. He is a knowledgeable and down to earth person, who is always available to help you with all the queries and provide you with the solution. I remember my first some months in the C2N, I was so scared in a new country so far from my home (India), he made me feel at ease in Sylvia's absence and assisted me in getting started the work. I really enjoyed working with him. I will always remember you whenever I will make band diagrams. Thank you for making me do better with band diagrams and all the suggestions during my thesis writing.

A special thanks to Dr. Guillaume Agnus for sharing his technical knowledge, LabVIEW and helping me setting up the equipment's for electrical measurements. Despite his busy schedule he was a great help. I am grateful for his assistance, support, and advice for the future. And thanks to the other permanent member of OXIDE group namely Dr. François Pesty and Dr. Pascal Aubert.

I would like to give a special thanks to be Dr. Stephane Gable (probably in September), with whom I begin my Ph.D. journey together under same supervisors and in the same office. It was such a pleasure to work with him. We have spent these years sharing knowledge (scientific, nonscientific), extensive discussions about our countries, culture, food, games, goals, and what not. You made this Ph.D. journey so memorable and easy going by being present. I would also like to express my gratitude to other colleagues Dr. Hela Al Mabrouk, Dr. Priya, Sukanya, Dr. Alicia Ruiz-Caridad, Abdelnour Benamar, Dr. Giovanni Magno, Dr. Loic Guillemot, Dr. Etienne Thiebaut, Laura Diebold, Ali El Boutaybi, Sopheasith Hem, Amine Mamouni, Subhajit Roy, Simon Rouvet, Fluorian Didier, Dr. Romain Bude and Alexandre Zing for their moral support and memorable moments we share during this journey.

In France, I am blessed to have many wonderful friends who treat me like family. I am grateful and thankful to each one of them for joining me on this trip and make it more fruitful for me, especially in the difficult times like covid. A big thank you to be Dr. Mahima Chaudhary for all the care and support during my thesis and covid time. She is gem of a person. I consider myself fortunate to have known you and have made a friend for life. I am thankful to Dr. Shweta Mehndiratta, Dr. Kartik Soni, Thea Soni, Dr. Ayush Shrivastava, Dr. Sanket Kalmakar, Dr. Saurabh, Dr. Amulya Priya, Irene Cortinovis, Dr. Mihir Sahasrabudhe, Maha, Monica, Jaya, Dr. Simli, Dr. Shallu Rani, Dr. Pragya Vishwakarma, Dr. Ankush Bhatia, Sonali Khurrana, Twinkle Bhatiya, Dr. Pranav, Priyam, Pranjal Bhadti, Abhijit Tagade, Amrut, Payal for the wonderful times and constant moral support.

A special thanks to Dr. Sumit Kumar, who has been an inspiration to me through all my life. Always motivated me to achieve more and see big picture in life. We started our Ph.D. together in the same city and defended together in March with a big smile on our faces. He was always by my side in my low times, encouraging me to find new sources of energy. I am blessed to have found a person like him who wants to see me successful beyond limits. This 3.5 years of exploring the world together, meeting new people, having new experiences, TMB trekking to writing thesis together we have come a long way enjoying this journey and that I wish to be continue this journey with you.

Now, I will take a moment to acknowledge a special friend that I have lost recently, late Dr. Yogendra Singh (Yogi), a talented researcher with an inquisitive mind. With his guidance, I was able to obtain a Ph.D. position at the first place in France. He selflessly helped everyone he met during his 29 years of life span. Always smiling, full of knowledge and always do funny things around, making everyone smile. He had a distinct way of connecting with everyone he ever encountered. I feel fortunate to had Yogi as a friend. May his soul rest in peace. Om Shanti.

Last but not the least a very big support from my family in India, motivating me from another continent, being patient, and always praying for my well-being so that I can achieve what I have dreamt of. Their blessing paves my way to successfully obtained a Ph.D. degree. And my closest friends, Monika Mishra, Harsh Khatwani, Sagar Thukral and Parul, who have been thus far motivating me at every step, are happier than me with my success.

Thank you all.

A tribute to my dearest friend Late Dr. Yogendra Singh!

Introduction

Ferroelectric thin films have a great potential in photovoltaic (PV) applications [1], owing to their high open-circuit voltage and switchable photovoltaic effect. The switchability property of the bulk PV effect (BPVE) in ferroelectrics enables an application beyond the generation of energy. The direction of the ferroelectric polarization can control the sign of the photocurrent in a ferroelectric thin film, theoretically allowing for 100% switchability of the photocurrent with the polarization, which is very interesting for potential applications such as photo-ferroelectric memories. It has previously been demonstrated that the photocurrent follows a loop (as a function of the poling voltage) similar to a ferroelectric hysteresis loop, indicating a direct relationship between photocurrent and electrically poled polarization for various ferroelectrics such as $BaTiO_3$ [2], $BiFeO_3$ [3], $Pb(Zr_{1-x},Ti_x)O_3$ (PZT) [2,4–6], $PbTiO_3$-based solid solutions [7] and FE superlattices [8]. Furthermore, the photocurrent switchability in integrated ferroelectric films between electrodes is not always achieved due to extrinsic parameters. For example, ferroelectric–electrode interfacial effects (Schottky barrier) [5,9,10], non-mobile charged defects, and the migration of charged defects, such as oxygen vacancies, under an applied electric field, can also affect the switchable photocurrent [1,11,12]. The mechanism of the PV effect in ferroelectric thin films is thus complex and can include several contributions which are experimentally difficult to disentangle: the so-called bulk PV [13] effect related to the noncentrosymmetry in a FE, the presence of depolarizing field due to partially unscreened polarization, and the presence of a built-in electric field in the material with various possible origins (such as gradient of charges, or Schottky potential barrier at interfaces giving a similar mechanism as classical PV effect in semiconductor p-n junctions).

The main objective of this thesis is to study the switchable properties of ferroelectric oxide thin films (PZT) integrated into capacitor geometry. In this work, switchable and non-switchable behavior of polarization and root cause of this behavior are discussed. It also includes different possible PV effects involved in FE devices. Switchability can be affected by intrinsic properties such as polarization and extrinsic properties such as electrodes/interfaces and defects. This works covers this specific property for the optimization of FE thin films, not only to achieve switchable PV properties but also to understand their ferroelectric response which indeed is beneficial for future photoferroelectric memory devices.

Outline of the thesis

- Chapter 1: This chapter includes an introduction on ferroelectric materials with perovskite structure, with a focus on PZT, and a detailed review of literature presenting these materials' progress and discussing why it is essential to stick to the fundamentals to understand better the physics of complex mechanisms related to photovoltaic effects in ferroelectrics.
- Chapter 2: This chapter provides a brief introduction of the techniques used for the growth and the characterization of the oxide thin films, including pulsed laser deposition (PLD), atomic force microscopy (AFM), and X-Ray diffraction (XRD). The structuration of the thin films into capacitor devices using photolithography and sputtering processes is presented. Moreover, electrical characterizations of PZT thin films integrated into capacitor geometry are described to investigate their dielectric, ferroelectric, and photovoltaic properties.
- Chapter 3: This chapter covers the general characterization of ferroelectric thin film specifically on a Pt/PZT/SRO//STO capacitor device. First, the surface morphology and crystal structure were studied using atomic force microscopy and x-ray diffraction. Then the ferroelectric and photovoltaic properties under two UV sources were analyzed.
- Chapter 4: In this chapter, a careful investigation of the polarization-dependent photocurrent of epitaxial lead zirconate titanate PZT thin films has been carried out. These measurements have shown that 1) the photocurrent depends linearly on the switchable part of the ferroelectric polarization and that 2) the analysis of this dependence provides important insights on the switchable and unswitchable internal electric fields in the FE material (the latter being necessarily related to pinned FE polarization). Such pinned polarization strongly affects the switchability of the PV properties in FEs and is otherwise rather difficult to probe by classical FE characterizations. These results are thus particularly relevant for the optimization of FE thin films, not only to achieve switchable PV properties but also to understand their ferroelectric response.
- Chapter 5: This chapter investigates the influence of the electrode/ferroelectric interface on photocurrent switchability in PZT capacitors. It includes the surface and structural properties of PZT films deposited on different electrodes. It also presents a comparison study between the top electrodes of Pt and ITO on PZT ferroelectric films grown on SRO and LSMO bottom electrodes. The effect of a STO buffer layer at the top and bottom electrode/ferroelectric interfaces is analyzed. The polarization screening efficiency in the different heterostructures is also extracted and compared.
- Chapter 6: This chapter provides a general conclusion and insights into perspectives.

Table of contents

Chapter 1

State of the art

Contents

1.1 Ferroelectric material

Ferroelectrics are versatile materials that possess spontaneous polarization, that occurs in the absence of an applied electric field [14,15]. One of the most significant features of ferroelectric materials is ferroelectricity which is the capacity to switch spontaneous polarization using an electric field. Since the discovery by Valasek et al. of ferroelectricity in Rochelle salt in 1921 [16], some of the most studied recently ferroelectric materials are $BiFeO_3$ (BFO), $BaTiO_3$ (BTO), $PbZr_{1-x}Ti_xO_3$ (PZT), etc. Ferroelectrics (FEs) are characterized by reversible spontaneous electric polarization, whose magnitude and direction can be precisely controlled by electric field but also by varying the temperature, composition, or pressure [17], enabling numerous applications including non-volatile ferroelectric memories [18]. In addition, the coupling between electric polarization and strain or magnetization makes ferroelectrics particularly interesting for the development of devices, such as sensors and actuators [19]. The study of light-matter interaction in FEs has shown the existence of novel phenomena, such as the unconventional photovoltaic effect [20–22], and the photostrictive effect (nonthermal photo-induced deformation) [23–26]. More recently, photo-ferroelectric materials have received renewed attention in thin films, offering rich physics and a wide range of exciting potential applications [27,28]. In particular, the capability to tune photo-induced effects through the in-situ control of electric polarization in FEs (tuning photocurrent [4,29] or photostriction [30]) offers an additional degree of freedom in the control of materials functionalities with interesting, applied perspectives [27,31].

This chapter includes an introduction on ferroelectric materials with perovskite structure, with a focus on PZT, and a detailed review of literature presenting these materials' progress and discussing why it is essential to stick to the fundamentals to understand better the physics of complex mechanisms related to photovoltaic effects in ferroelectrics.

1.1.1 Ferroelectric oxides

In a solid, crystallinity is defined by the spatial arrangement of the atoms. Due to the variation in the arrangements of the atoms and interatomic bonds, the lattice symmetry can be centrosymmetric or non-centrosymmetric. Out of the 32 existing crystal classes (Figure 1.1), 11 are centrosymmetric, and 21 are non-centrosymmetric. Among these last ones, 20 are piezoelectric and exhibit changes in their properties under mechanical stress. Among these 20 piezoelectric classes, some show a spontaneous electrical polarization that appears below a critical temperature (T_c) and are known as pyroelectric materials. Among the pyroelectric materials, some can further be ferroelectric, with a remanent polarization that can be switched under an applied electric field. All the ferroelectric materials are thus piezoelectric as well as pyroelectric, but the reverse is not true. The transition temperature of ferroelectric material is known as Curie temperature (T_c), over which the crystal is centrosymmetric. Below T_c, the crystal acquires a non-centrosymmetric structure and exhibits ferroelectricity. In the case of ferroelectric crystals with ABO_3 perovskite structure (Figure 1.2), the unit cell is cubic above T_c with the type ‘A’ cations sitting at the cube-corner position, the type ‘B’ cations sitting at the body-center position, and oxygen atoms sitting at face-centered positions. When the temperature of a perovskite material is lowered below T_c, the unit cell is not cubic anymore and gets a lower symmetry, as a result of oxygen octahedra rotations/distortions and/or relative shifts of B cation away from the octahedron center. This gives rise to polar unit cells, with a macroscopic resultant electrical polarization. As a result, the ferroelectric perovskite material undergoes a transformation from a paraelectric centrosymmetric structure to a ferroelectric noncentrosymmetric structure that is frequently tetragonal or rhombohedral. Below T_c, in the tetragonal phase, for example, the material shows a switchable remanent polarization between up and down states as shown in Figure 1.2.

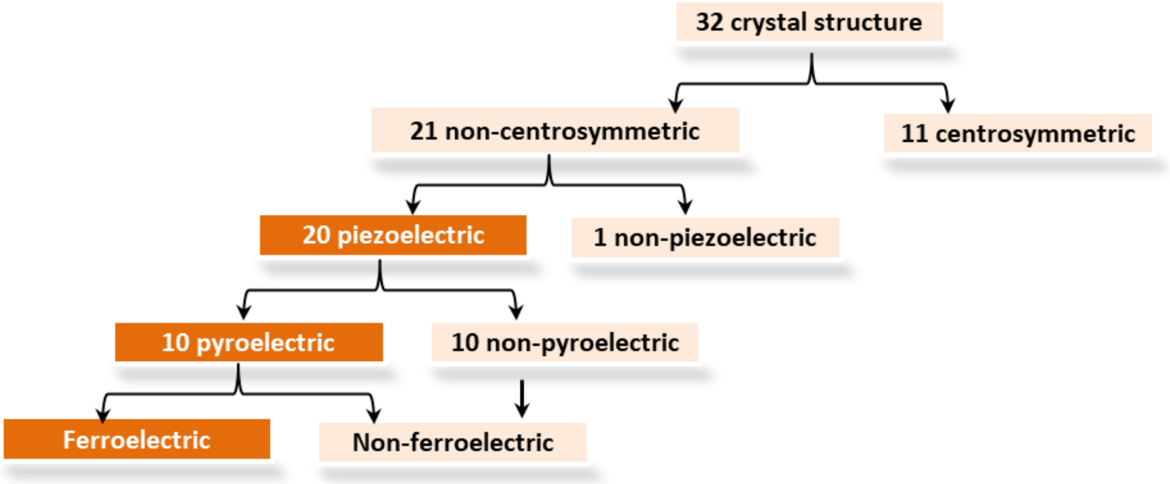

Figure 1.1. Flow chart of 32 crystal classes.

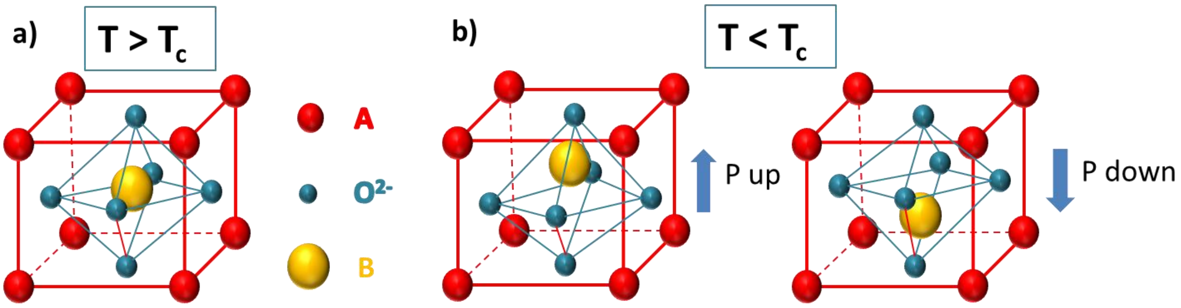

Figure 1.2. Ferroelectric ABO_3 perovskite structure in a) cubic phase above T_c, b) tetragonal phase below T_c for up and down polarization states.

Measurement of the displacement current that flows in response to an applied electric field can be used to probe polarization switching. More details about the measurement of polarization can be found in the second chapter of this thesis. Starting from a zero-polarization state with ferroelectric domains oriented randomly (Figure 1.3), the polarization in a ferroelectric material increases with the applied electric field. First the domains orient and align their polarization along the applied electric field, and the global polarization reaches a spontaneous polarization (P_s) state pointing upwards for a positive applied electric field. Then the ferroelectric polarization will continue increasing linearly with the applied electric field. When the electric field intensity decreases, some domains can disorient and the ferroelectric polarization within each domains decreases, resulting in a smaller but nonzero polarization at zero fields, called remnant polarization (P_r). Increasing further the field in the opposite (negative) direction results in a downward polarization state. The ferroelectric polarization follows thus a hysteresis loop as a function of the applied electric field. The field required to bring the polarization to zero during the switching is called the coercive field, E_C. The polarization-electric field hysteresis loop (shown in Figure1.3) is a fundamental feature of a ferroelectric.

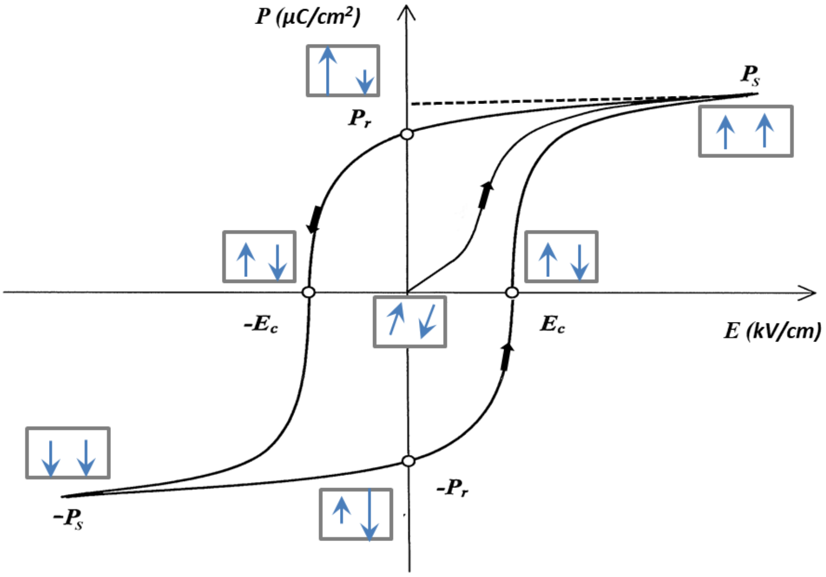

Figure 1.3. Typical P-E hysteresis loop of a ferroelectric material below its Curie temperature (T_c). Above Tc, the crystal has no spontaneous polarization.

1.1.2 Lead Zirconate titanate ($PbZr_{1-x}Ti_xO_3$)

$PbZr_{1-x}Ti_xO_3$ (PZT) has a perovskite structure as shown in Figure 1.4. PZT is a solid solution of lead titanate ($PbTiO_3$) and lead zirconate ($PbZrO_3$). It possesses some of the most vital ferroelectric characteristics of any material discovered to date and could be adjusted to the application by adding dopants. As a result, it is the most often utilized material in industrial applications, including actuators, sensors, energy harvesters, and non-volatile memories [32].

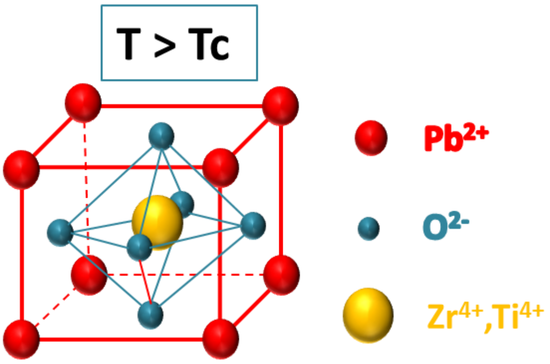

Figure 1.4. The perovskite unit cell structure of PZT in the cubic phase.

Importantly, the properties of PZT are strongly dependent on the cation Zr:Ti ratio. Figure 1.5 shows that, for the value of x < 0.48, x > 0.52 and 0.48 < x < 0.52, PZT exhibits a rhombohedral, tetragonal, and MBP (morphotropic boundary phase) phases [33–36]. In the whole composition range, the critical temperature is above 200°C, making PZT useful for applications at room temperature.

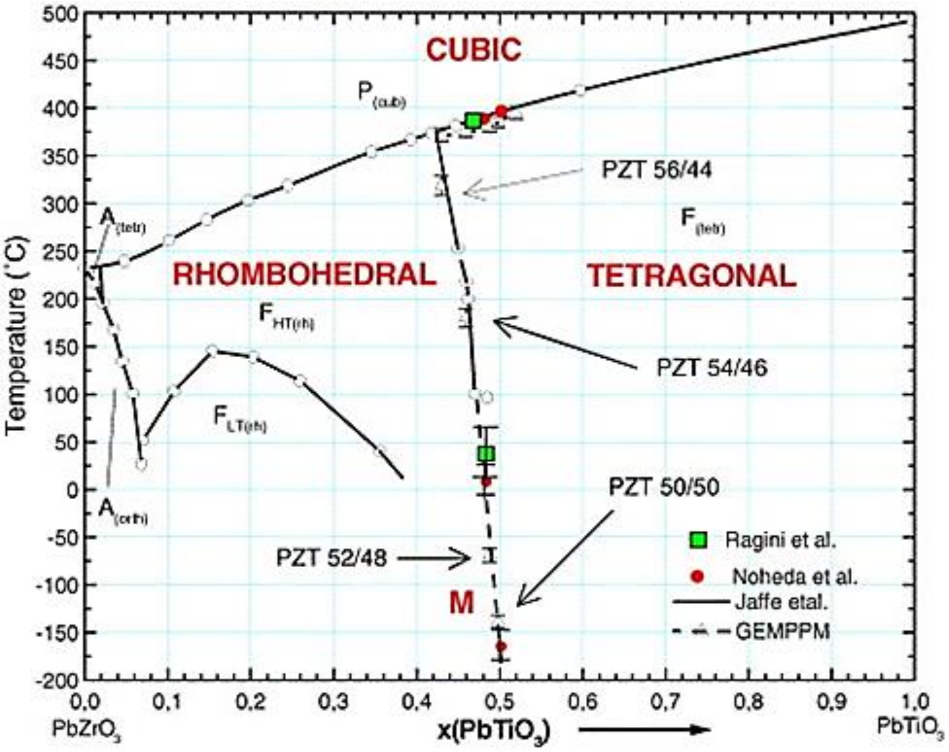

Figure 1.5. The crystal structure of PZT depends on the percentage x of Ti [37].

The typical ratio between the out-of-plane ‘c’ parameter and in-plane ‘a’ lattice parameter is found to be 1.05 and 1.01 for the 20/80 and 52/48 composition respectively. These two compositions are the most studied and used for different applications because the 20/80 composition provides a high remnant ferroelectric polarization value, while the 52/48 shows enhanced electromechanical and dielectric properties related to the high polarizability of the material at the MPB.

1.1.3 Ferroelectric thin film integrated into a capacitor

A ferroelectric material can be considered as a wide bandgap semiconductor and PZT as a n- or p-type semiconductor because of its defect chemistry. From previous analysis of transport mechanism through PZT films grown in our group, PZT has been found to behave like a n-type semiconductor [38]. In a capacitor geometry, a ferroelectric thin film is sandwiched by metal electrodes, forming a Metal/Ferroelectric/metal (MFM) structure. Both interfaces are characterized by Schottky contacts and associated depletion regions [39]. An example of MFM structure can be seen in Figure 1.6 showing schematics of energy band diagram for Pt/PZT/$SrRuO_3$. A MFM structure can be regarded as two back-to-back Schottky diodes. The

PZT film (~100nm) is thick enough to avoid the overlapping of the two depletion regions associated with Schottky contacts. Each Schottky contact is characterized by a built-in potential V_{bi} and a potential barrier height ϕ_B. In the Pt/PZT/SRO MFM structure, PZT has a bandgap in the 3.2-3.9 eV range depending on the composition, and the barrier height can be approximated to 1 V for Pt/PZT and 0.5 V for PZT/SRO interfaces, giving rise to some asymmetry [40]. From previous analysis of transport mechanism through PZT films grown in our group, Pt/PZT and PZT/SRO interfaces exhibit experimental barrier heights of 0.72 eV and 0.38 eV [38].

In the case of a ferroelectric-electrode interface, the built-in potential of the Schottky junction is modified by the ferroelectric charges. By treating the ferroelectric polarization as a sheet charge placed within the ferroelectric at a finite distance from the electrode interface, the modified built-in field V'_{bi} can be expressed as follows [41,42]:

$$V'_{bi} = V_{bi} \pm \left(\frac{P\delta}{\epsilon 0 \epsilon r}\right) \qquad (1.1)$$

Where V_{bi} denotes the built-in potential in the absence of the ferroelectric polarization, δ is the thickness of the interface layer (distance between the polarization surface charge and the physical interface with the electrode), ε_0 is the permittivity of free space, and ε_r is the static dielectric constant [41,42]. In the present MFM structure for n-type PZT, the built-in potential at the top Pt/PZT interface increases for up polarization state (polarization pointing towards the Pt interface) (Figure 1.6b).

The Schottky effect induces a reduction of the potential barrier, resulting in an apparent potential barrier Φ_{app} depending on the maximum electric field at the interface (E_m) and the dynamic (high-frequency) dielectric constant (ε_{op}) [39]:

$$\phi_{app} = \phi_B - \sqrt{\frac{qE_m}{4\pi\varepsilon_0\varepsilon_{op}}} \qquad (1.2)$$

When considering the effect of the ferroelectric polarization, the electric field E_m can be further expressed, under zero applied electric field, by [41]:

$$E_m = \sqrt{\frac{2qN_{eff}V'_{bi}}{\varepsilon_0\varepsilon_{st}}} \pm \frac{P}{\varepsilon_0\varepsilon_{st}} \qquad (1.3)$$

Where N_{eff} is the effective charge density in the depleted region, V'_{bi} the modified built-in potential (given in (1.1)) and P the ferroelectric polarization.

The effect of the ferroelectric polarization on the apparent potential barrier can be rewritten by considering that the second term in equation (1.3) is dominant (assumption valid since the apparent built-in potential is ~1 eV and there is a low amount of free charges) [4]:

$$\phi'_{app} = \phi_B \pm \sqrt{\frac{qP}{4\pi\varepsilon_{op}\varepsilon_0^2\varepsilon_{st}}} \qquad (1.4)$$

In addition to changes of potentials at interfaces, the presence of a ferroelectric polarization also gives rise to a depolarizing field (E_{dep}) in the bulk of the thin film because of the incomplete screening of the polarization charges at the interfaces (more information about the depolarizing field is given in chapter 4). For negative poling case for example (negative voltage applied to the top Pt electrode), when polarization is directed upwards, a downwards depolarizing field is induced, pointing opposite to the polarization as shown in Figure 1.6b.

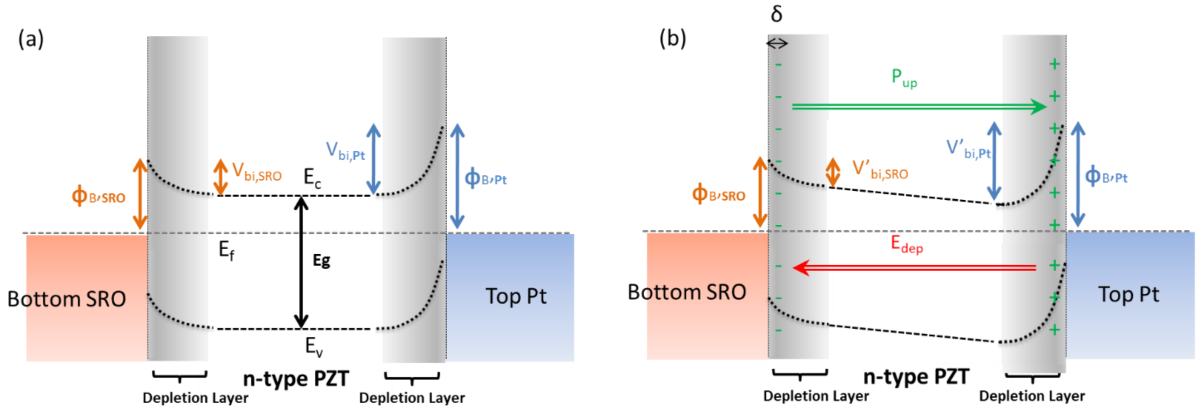

Figure 1.6. Schematic of a Metal/Ferroelectric/Metal structure with a ferroelectric thin film (PZT) sandwiched between the top (Pt) and bottom (SRO) electrodes. (a) Band diagram showing the Schottky contacts at each interface and (b) the effect of the ferroelectric polarization for a up polarization state (in particular $V'_{bi,Pt} > V_{bi,Pt}$).

1.2 Photovoltaic effect in the perovskite ferroelectric oxides

Around half a century ago, the ferroelectric photovoltaic (PV) effect was identified in non-centrosymmetric ferroelectric materials [43] and is fundamentally different from that of typical p-n junctions. In a ferroelectric material, ferroelectricity produces by itself a separation of photo-excited charges caused by light absorption, allowing the generation of very high photovoltage. Additional PV mechanisms such as PV effect due to the Schottky barrier at the ferroelectric/electrode interface can also be present in a ferroelectric material sandwiched between electrodes. The first section will introduce the charge separation mechanisms in conventional p-n photovoltaic cells exhibiting interface-induced photovoltaic effects. Then, the other photovoltaic mechanisms which can occur in a ferroelectric material will be discussed in detail, along with state-of-the-art for various ferroelectrics.

1.2.1 Classical PV effect in p-n junction

Silicon-based solar cells have p-n junctions formed by doping the same semiconductor with impurities to create hole-rich (p-type) and electron-rich (n-type) areas. The p-type and the n-type regions merge at equilibrium through a narrow depletion junction. In Figure 1.7 a, free charges are generated when photons with energies higher than the bandgap are absorbed. The photogenerated charges are separated by the internal electric field, E_{bi}, induced by the energy barrier at the depletion interface layer and give rise to short circuit current I_{sc} and open-circuit voltage V_{oc} which is limited by the difference in quasi-Fermi levels of electrons and holes and cannot exceed the bandgap energy, Eg, of the material. The PV mechanism in p-n junction is thus interface-related.

The maximum efficiency of a single p-n junction is determined to be 31% of incoming light in the case of an energy gap of Eg = 1.35 eV [39,44], commonly known as the Shockley-Queisser limit. In the p-n junctions PV effect, the main limitation is that the open-circuit voltage V_{oc} cannot exceed the bandgap value but the short circuit current density J_{sc} can be of the order of mA/cm^2. The PV effect in the p-n junction's operating principle also applies to metal-semiconductor junctions. Ferroelectrics can also be used as an alternative to improve the efficiency of solar cells. As mentioned earlier, the lack of center of symmetry in ferroelectrics helps in the separation of photogenerated carriers as illustrated in Figure 1.7 b. The main advantage of the FE-based PV effect is that the open-circuit voltages (V_{oc}) can exceed the material's bandgap, reaching values up to kV. Unlike the p-n junction, the PV effect in FE is based on single bulk material. This phenomenon is also known as bulk photovoltaic effect in the case of non-centrosymmetric crystals (BPE).

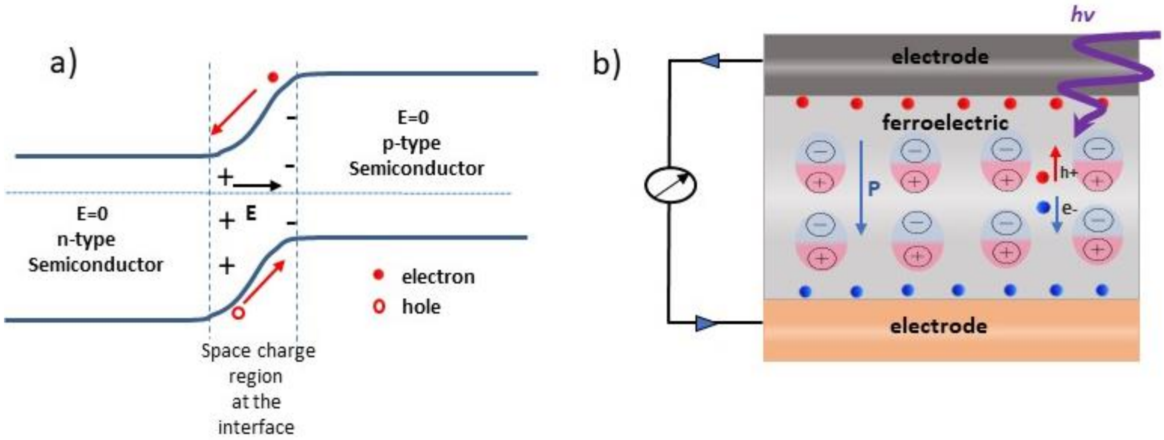

Figure 1.7. Photovoltaic effect schematics in a) a semiconductor p-n junction and b) ferroelectric-based capacitor device.

1.2.2 Bulk photovoltaic effect (BPVE)

The BPVE appears as a steady-state photocurrent generated in the bulk region of the FE material, resulting from the lattice non-centrosymmetry [45–48].

Many ferroelectrics can be thought of as wide bandgap semiconductors, comparable to silicon. In 1956, the first photovoltaic effect in ferroelectrics was discovered on $BaTiO_3$ (BTO) [20]. Glass et al. proposed the first theory for the photovoltaic effect in ferroelectrics in 1974 [22,49], to describe photoinduced current in $LiNbO_3$ (LNO) non-centrosymmetric crystals and proposed that the photocurrent is directly related to the intensity of light I_l (W). The steady state photoinduced current can be written as

$$Jsc = k\alpha I_l \qquad (1.5)$$

Where k is the Glass constant (A.cm/W) and α is the absorption coefficient (cm^{-1}). The photoinduced currents measured in LNO single crystals are of the order of nano ampere.

The photo-induced current is related to the film thickness, as shown by the relationship [50]:

$$Isc \sim A\alpha\Phi * \exp(-\alpha d) \qquad (1.6)$$

Where, ϕ is the photon flux density per second, d the film thickness and A is a constant depending on many parameters such as the internal field, quantum efficiency, the lifetime of charge carriers, their mobility, and energy. Since, the current increases when the thickness decreases, the use of thin-film is preferred to increase the PV efficiency of the device.

The BPVE current depends on the polarization of light with respect to the ferroelectric polarization. As it exhibits a second-order nonlinear optical response, it is described by a third rank tensor under linearly polarized illumination [43,51–53]. Hence, the contribution of BPVE to the photocurrent and its dependency on the light wave polarization vector can be written as

$$J_{sc} = \beta_{ijk}^{L} e_j e_k^{*} I \qquad (1.7)$$

Where, β_{ijk}^{L} is BPVE third rank tensor for linearly polarized light, e denotes polarization vector in direction j and k and I is the intensity of light [52].

The light-induced voltage of up to kV is a unique feature of this photovoltaic effect [54]. The open circuit photovoltage Voc arising from photocurrent depends on the electrode spacing (d) and the conductivity (σ), [45]:

$$Voc = Jsc\left(\frac{d}{\sigma}\right) \qquad (1.8)$$

Where, σ is the combination of dark conductivity (σ_d) and photoconductivity (σ_{ph}):

$$\sigma = \sigma_d + \sigma_{ph} \qquad (1.9)$$

Internal energy gap levels or, as in other sensitive cases, oxygen deficiency [55] can affect the values of photo-induced voltages.

1.2.3 Depolarization field induced PV effect

In ferroelectric thin films sandwiched between electrodes, screening of spontaneous polarization occurs at the metal/ferroelectric interface. Polarization bound surface charges are partially compensated by free charge carriers of the metal electrodes, resulting in incomplete screening. Due to that there induces an electric field opposite to polarization known as Depolarizing field (Ed), reducing amplitude of polarization [56–58]. As the depolarization field is inversely related to the distance between charged surfaces, its effect on PV properties is more significant in ferroelectric thin film (<100 nm) than bulk [59,60].

The internal electric field in the ferroelectric capacitor may arise from electrode/ferroelectric contact, defects within the ferroelectric layer and the depolarization field. According to reference [56] the depolarization field is expressed as:

$$E_{dep} = \frac{P}{\epsilon_{FE}} \frac{\frac{2\epsilon_{FE}}{l}}{\frac{2\epsilon_{FE}}{l}+\frac{\epsilon_e}{l_s}} \qquad (1.10)$$

Where P is the polarization, ϵ_{FE} the dielectric permittivity of the ferroelectric material, l is the thickness of ferroelectric film. ϵ_e and ls denotes dielectric permittivity and screening length of the electrode, respectively. It is evident from Equation (1.10) that depolarization field is clearly dependent on the electrode characteristics, i.e., screening length and dielectric permittivity. In 1969, Chen noticed a photocurrent in the direction opposite to the spontaneous polarization in single crystal $LiNbO_3$ under UV illumination and considered an unidentified internal electric field to be the source, [49] that was later specified as depolarization field. This sparked further investigation on the depolarization-induced PV effect mechanism. In 2009, Qin et al. established a detailed model in which ferroelectric material and contacting electrodes were taken into account as a whole [60].

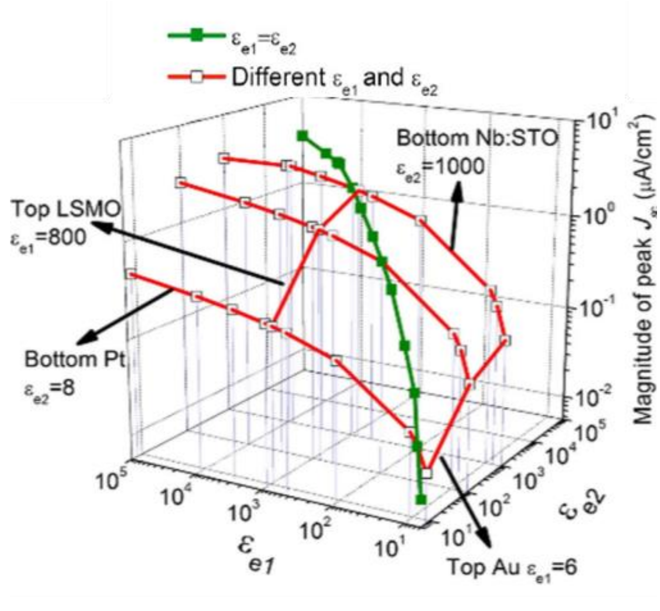

Figure 1.8. Calculated results showing effect of dielectric constant of top and bottom electrodes on peak of photocurrent density in PLZT thin films [60].

It has been estimated that thin films sandwiched between electrodes with infinite dielectric constants can achieve an extremely high photovoltaic efficiency of up to 19.5 percent using a semiconductor-based model with ferroelectric charge distribution that includes polarization surface charges, Schottky effect-based space charges, and screening charges [60]. Theoretical results shown in Figure 1.8 reveal that electrodes with large dielectric constant, e.g., conductive oxides such as LSMO, induce higher photocurrent, by virtue of weakening the polarization screening effect. Regardless of all uncertainties, depolarization induced charge separation mechanism can clearly explain the switchable photovoltaic effect through studying the polarity of PV output.

1.2.4 Schottky contact-induced PV effect

The effect of electrodes and interfaces on the photovoltaic attributes of ferroelectrics is a two-sided trait. Not only electrodes can influence the depolarization field, they can also induce an interfacial built-in field. Schottky barrier effect is based on an interfacial effect, similar to the p-n junction effect, generally formed at the ferroelectric/electrode interfaces, and the barrier height and width can be modulated by polarization. When a ferroelectric thin film is placed between two similar or different electrodes with high work functions which act as two back-to-back Schottky contacts, a built-in electric field (E_{bi}) is generated at the interfaces which can act on the separation of photoexcited charges [4,5,29,61]. Due to the similarity of the film thickness and depletion layer width, this effect is particularly noticeable in ferroelectric thin films. Schottky barrier effect may enhance switchability of the PV effect because ferroelectric polarization charges [10,60] or charged defects [62] can alter the Schottky barrier height. The difference between Schottky barriers at metal/ferroelectric interfaces determines both the direction and value of PV response in a ferroelectric-based PV device with the ferroelectric film sandwiched between two electrodes [60]. As a result, the Schottky barrier's contribution to the PV effect is significant for asymmetric interfaces [63]. PV responses from identical Schottky contacts would otherwise cancel each other out owing to the fact that they run in opposing directions. Zheng et al. [64] proposed a simple model for PZT capacitors with symmetric interfaces to distinguish the contributions of the Schottky barrier and depolarization on PV effect by measuring the photocurrent in up-poled (I_{up}) and down-poled (I_{down}) films.

$$I_{Ebi} = \left(\frac{Iup+Idown}{2}\right) \qquad (1.11)$$

$$I_{Edep} = \left(\frac{Iup-Idown}{2}\right) \qquad (1.12)$$

Where I_{Ebi} and I_{Edep} represent the contribution of the built-in field E_{bi} and depolarizing field E_{dep} on the short-circuit photocurrent, respectively.

1.2.5 Domain walls PVE

Ferroelectric materials can be improved in terms of photovoltaic performance by using naturally existing potential barriers in the material structure. Ferroelectric domains are separated by a domain wall that permits transit between two neighboring domains with different polarization directions.

Yang et al. [65](2010) demonstrated that $BiFeO_3$ (BFO) thin films with an ordered array of 71° or 109° domain walls can generate a photovoltage Voc = 16 V greater than the bandgap, as well as an in-plane photocurrent density Jsc = 120 A cm^{-2} flowing in the opposite direction of the polarization. More crucially, when the electrodes are parallel to the domain walls, the photovoltage grows in direct proportion to the number of parallel domain walls, but when the electrodes are perpendicular to the domain walls, the photovoltage decreases (Figure 1.9). A potential drop occurs at domain walls as a result of polarization rotation at domain interfaces, with the 180° domain walls having the biggest potential drop, followed by the 109° domain walls, and the 71° domain walls having the lowest potential drop [65,66]. As a consequence, the role of domain walls on PV effect is proposed: the potential drop in the domain walls generates an extremely large electric field ($5x10^6$ Vm^{-1}). Furthermore, because of the high electric field present in the domain walls, another assumption can be done: charge recombination is expected to happen at a much slower rate in the domain walls, and domain walls produce the majority of the anomalous photovoltaic (APV) effects while the BPVE is ignorable [66].

Various physical and numerical evidences, on the other hand, brought the domain wall hypothesis into doubt. Using Atomic Force Microscopy (AFM) to investigate the local effects of photoelectrons on a single crystal of $BiFeO_3$ (BFO), Alexe et al. found that there are no significant differences in photocurrent on domains and at domain walls, implying that recombination speed is uniform throughout the sample [67]. Furthermore, a recent study [68] found that photocurrent is impacted by the polarization direction of the incident light, which contradicts the domain wall theory, which predicts photocurrent as a function of the potential drop at the domain walls.

Another interesting discovery by Bhatnagar et al. shows the significant role of photoconductivity on the photovoltage for all measurements geometries (electrodes parallel or perpendicular to the DWs). Voc varies with increasing temperature in the form of a decaying exponential, in agreement with the conductivity which increases exponentially at higher temperature [69]. In the perpendicular geometry, the high dark and photoconductivity's of the DWs are preventing a large open circuit voltage since these are connecting the collecting electrodes.

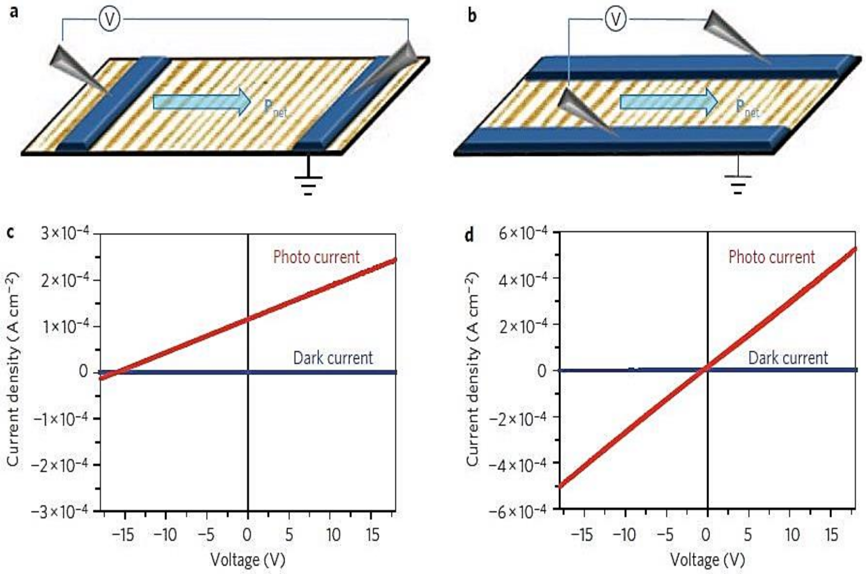

Figure 1.9. Schematics and IV characteristics of the BFO illuminated with white light, in parallel (a, c) and perpendicular configuration (b, d) with respect to the domain wall [65].

1.3 Factors affecting PV properties in FE

The photovoltaic properties of ferroelectric materials have been shown to be dependent on many factors such as the polarization, thickness, domain walls, defects, the bandgap of the FE, ferroelectric/electrode interface. In the following chapter, factors affecting the PV properties are detailed.

1.3.1 Polarization

Polarization is an intrinsic property of ferroelectric materials, which can be switched under an applied electric field. The direction of the ferroelectric polarization can control the sign of the photocurrent in a ferroelectric thin film [2,4,5,7,29,70]. Switchability of PV properties in FEs is of great interest for potential applications as photoferroelectric memories but it is not always achievable because of the nature of the electrode-ferroelectric interface (Schottky barrier), thickness, and defects.

To study the influence of polarization on the photovoltaic properties, Choi et al. measured a BFO single crystal sample with gold electrodes, illuminated by a 20 mW/cm^2 light at 532 nm wavelength as seen in Figure 1.10 (a). A photocurrent density of 7.35 mA/cm^2 was observed where the origin of PV effect expected was modulation of Schottky barrier height at interfaces [68].

Additionally, the applied electric field can totally switch the diode characteristic in BFO ferroelectrics [62]. In 2016, Yang et al. demonstrated that polarization may be used to switch the J-V characteristic of $La_{2/3}Sr_{1/3}MnO_3$/BFO/ITO under one sun illumination [71]. The curve is rectifying in the up-polarization direction, and the photocurrent is proportional to the light intensity, whereas the curve is linear in the down polarization direction. The photocurrent is always in the opposite direction to the polarization. These results are explained by a polarization-induced change of Schottky barriers [71]. Related reports in $(Pb_{1-x},La_x)(Zr_{1-y}Ti_y)O_3$ doped with WO_3 [72] (PLZT) demonstrate the capability of reversing the polarization to reverse the direction of the photovoltaic current, or at the very least to tune its magnitude.

Another example is reported by Lee et al. where photocurrent density of 0.1 mA/cm^2 was measured on a 400 nm thick BFO film in between Pt top electrode and $SrRuO_3$ (SRO) bottom electrode under 10 mW/cm^2 [29]. The photocurrent density was reversed between the up and down polarization state. Notably, the photocurrent was zero when domains in both polarization state became the same amount as shown in Figure 1.10 (b). These results are consistent with the BPVE as photocurrents of equal magnitude are present for opposite signs of polarization. Interestingly, it is also observed that the photocurrent makes a hysteresis loop which superimposes FE loop indicating direct relation between the polarization and photocurrent.

Furthermore, it has previously been demonstrated that the photocurrent follows a loop (as a function of the poling voltage) similar to a ferroelectric hysteresis loop, indicating a direct relationship between photocurrent and electrically poled polarization for various ferroelectrics such as $BaTiO_3$ [73], $BiFeO_3$ [29], $Pb(Zr_{1-x},Ti_x)O_3$ (PZT) [4,5,7,70], $PbTiO_3$-based solid solutions [7].

One may consider reversing the direction of polarization to change the direction of the photocurrent to produce a similar effect to the switchability of the ferroelectric diode. Notably, this notion is perfectly consistent with the third rank of the BPVE tensor, as reversing the polarization reverses the BPVE tensor and hence reverses the photovoltaic current. Another source of switchability is the variation of the Schottky barrier height at the ferroelectric-metal interface caused by polarization.

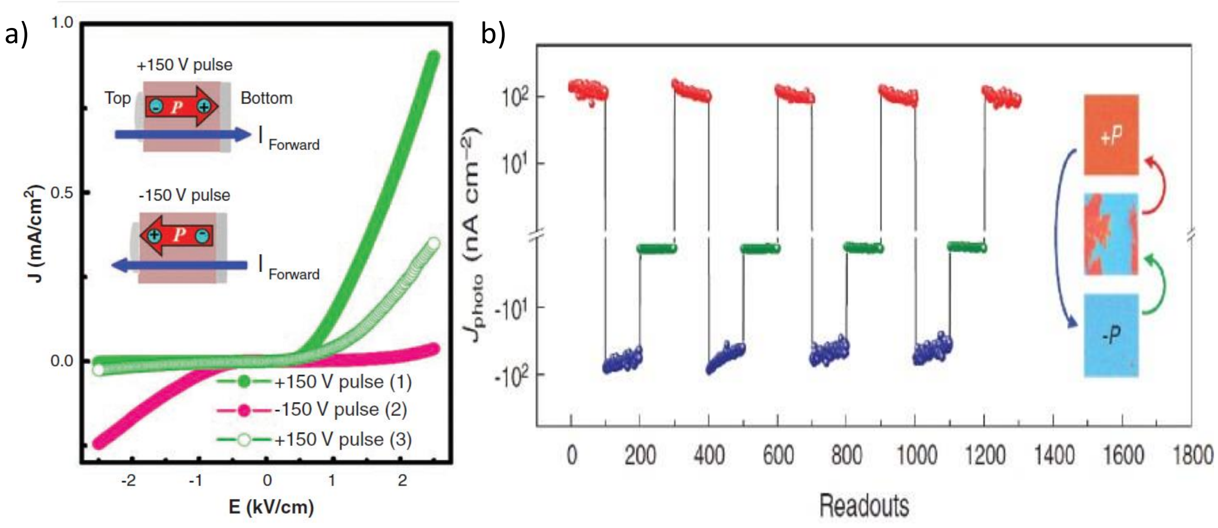

Figure 1.10. a) I-V characteristic of a BiFeO3 single crystal [68] b) photocurrent measured in up and down polarization states in BiFeO3 thin film capacitors [29].

The switchability property of the BPVE in ferroelectrics enables a use beyond the generation of electricity. Polarization-dependent photo response was evaluated in PZT to be further used as non-destructive readout ferroelectric memories [74,75].

Photovoltaic current and open-circuit photovoltage measured in a 100 nm thick BFO thin film on $La_{0,7}Sr_{0,3}MnO_3$ as bottom electrode and Pt/Fe as top electrodes, were found to be 0.15 pA/-0.13 V for a down polarization state, and -0.15 pA/0.21 V for an up-polarization state [31]. A 16-cell photoferroelectric memory prototype was created based on this idea (see Figure 1.11), with information being written by changing the polarization and read by measuring the photovoltage [31].

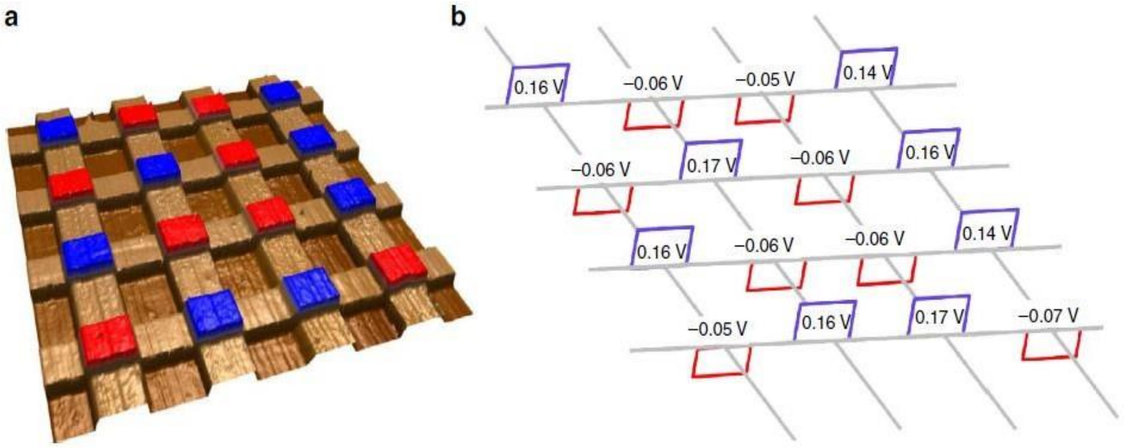

Figure 1.11. A BFO based 16 cells photoferroelectric memory prototype [31].

1.3.2 Electrode/Interfaces

Different electrodes make different Schottky barrier at the ferroelectric interfaces [41,76,77], and can affect transport properties by introducing high contact resistance or inducing ferroelectric diodes if only one interface has a Schottky contact, and the other is ohmic for example. In order to develop efficient and switchable devices, such as photoferroelectric memory, great attention must be paid to the choice of contacting electrodes [31]. The ability to tune the barrier height of the Schottky contact via polarization is one of the benefits of using ferroelectrics instead of traditional semiconductors. The switchable effect is thought to be caused by a variation of the Schottky barrier at the ferroelectric/metal interface [78,79]. Indeed, the electric polarization at the interface changes the Schottky barrier, modifying it by an amount depending on whether the polarization P is oriented in up or down state [41].

On a PZT (20/80) thin film deposited on an SRO bottom electrode on top of a STO (100) substrate, extensive research of the top electrode effect was undertaken [61]. Pintilie et al. discovered that the switching behavior does not occur for all electrodes, but only for top electrodes made of Pd, Ag, or SRO. When reversing the polarization, no reversal of the photovoltaic current was seen in other samples with top electrodes such as Cr, Pt, or Al (see Figure 1.12). The author postulated a similar mechanism of regulation of the space charge area at the metal-ferroelectric interface to account for the variable behavior with different top electrodes.

According to theoretical calculations, oxide electrodes with a high dielectric constant, such as (La,Sr)MnO_3 (LSMO), could enhance the power conversion efficiency (PCE) by up to 19.5% in PLZT capacitors [60]. It is worth noting that none of these simulations account for the BPVE effect because they are based on Poisson equation resolution and classical transport equations.

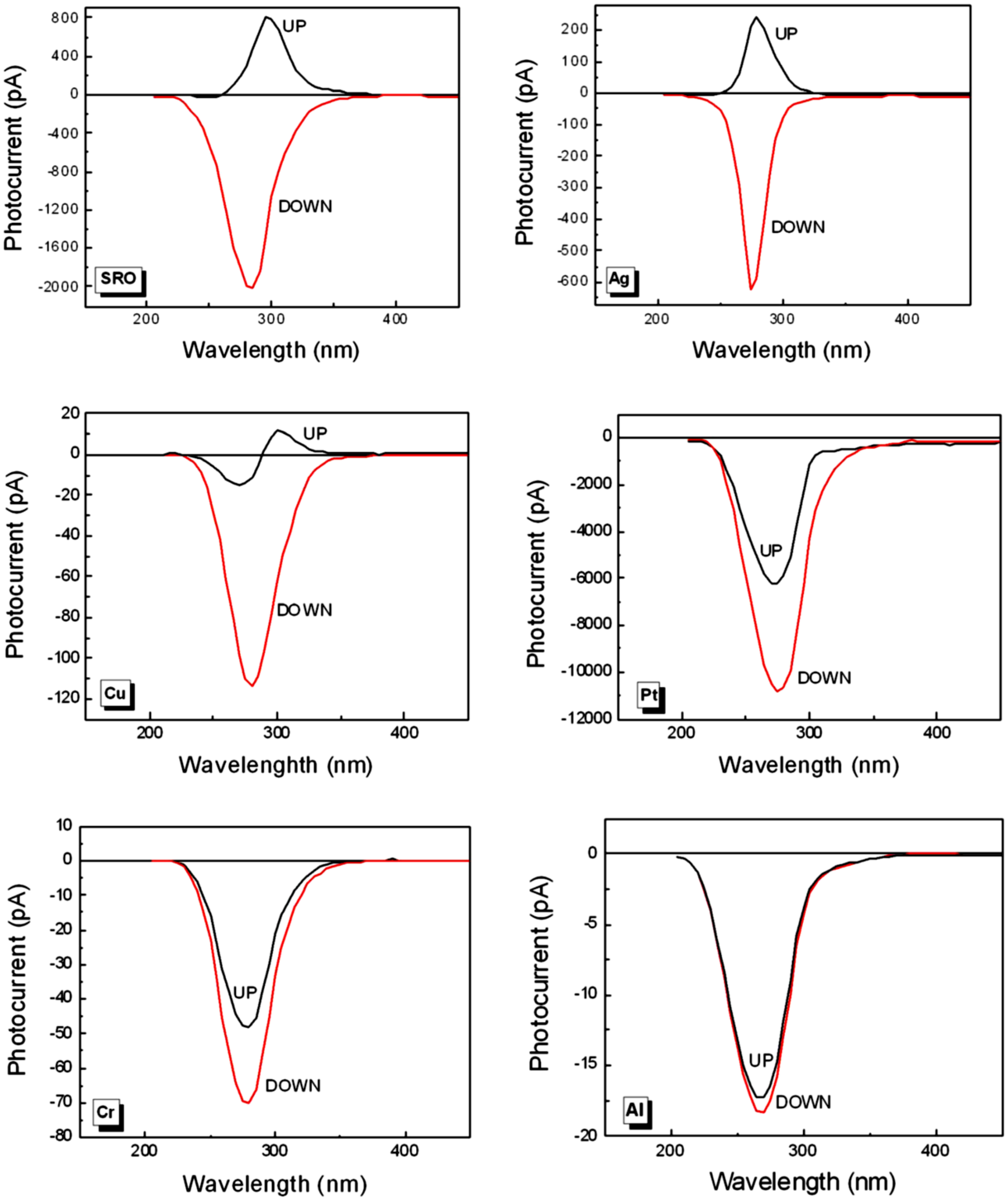

Figure 1.12. Photocurrent measured in PZT capacitors for different upper electrodes [61].

It is interesting to calculate the switchability (S) of the photocurrent in a ferroelectric device given by,

$$S = \left| \frac{Jup - Jdown}{2\max\left(|Jup|,|Jdown|\right)} \right| \tag{1.13}$$

with J_{up} being the photovoltaic current density in the up-polarization state and J_{down} being the photovoltaic current in the downstate, for potential uses in photoferroelectric memories. For example, in Bi_2FeCrO_6 films on $SrTiO_3$:Nb substrates with ITO top electrodes, it was estimated to be on the order of 70% [80].

There is also work on perovskite heterostructures based on $LaVO_3$(LVO)/PZT, with different thicknesses of LVO, sandwiched between Pt and SRO electrodes that is worth noting. The LVO films with a low bandgap (1.65 eV) are capable of producing a large number of charge carriers under illumination. While preserving strong photoresponse switchability (See Figure 1.13), the device with LVO layer thickness of 24 nm has the maximum PCE of 0.01%. As a result, combining a narrow-gap semiconductor with a ferroelectric is a good strategy for achieving high PCE and good photoresponse switchability in FE PV devices [81].

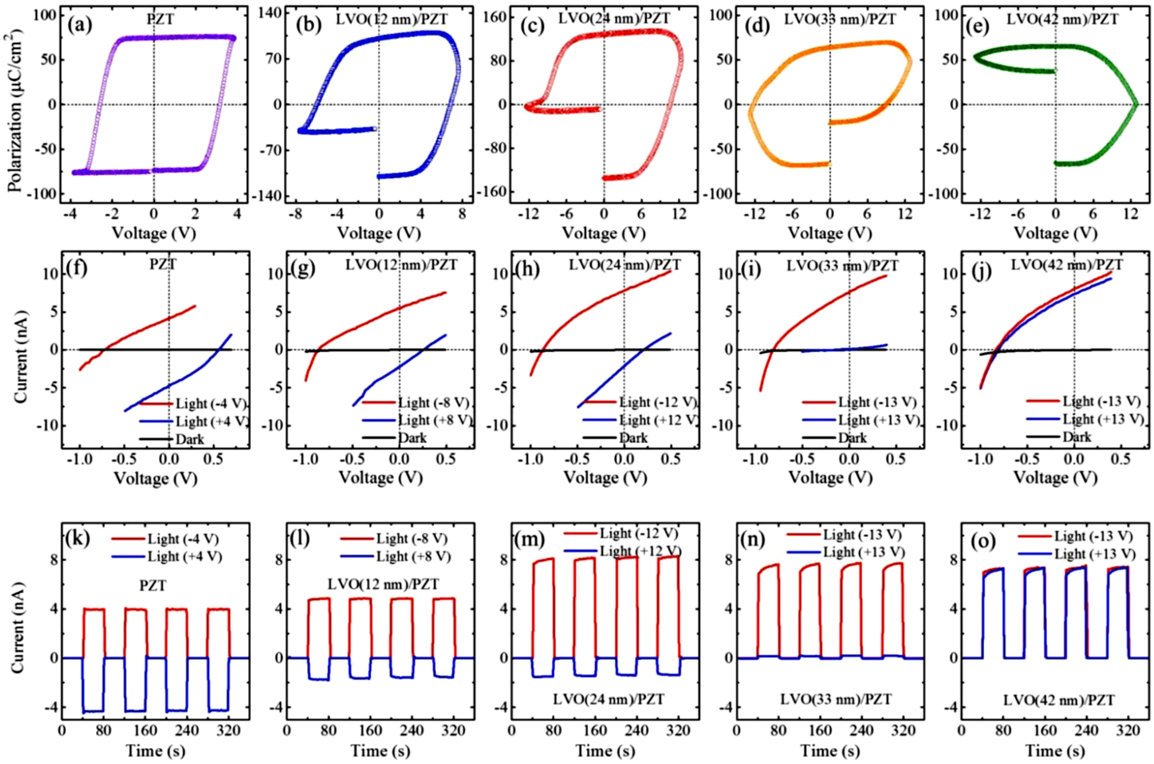

Figure 1.13. (a–e) P–V hysteresis loops, (f–j) photovoltaic I–V characteristics, and (k–o) time dependent photocurrents of (a, f and k) Pt/PZT/SRO, (b, g, and l) Pt/LVO(12 nm)/PZT/SRO, (c, h and m) Pt/LVO(24 nm)/PZT/SRO, (d, i and n) Pt/LVO(33 nm)/PZT/SRO, and (e, j, and o) Pt/LVO(42 nm)/PZT/SRO devices. In (f–o), the voltages for positive and negative poling are indicated in the brackets [81].

1.3.3. Thickness

Ferroelectric thin films have been extensively studied for their integration in photoferroelectric devices. Optimizing their thickness is crucial to improve photovoltaic properties. Earlier research indicated that UV-illuminated Au/PLZT/Pt films with a thinner thickness had greater photovoltaic currents (Jsc), such as 0.85 nA for 260nm-thick film under 1.6 mW/cm2 UV illumination [28]. The interaction between the space charge area at the electrode/FE interface and the electrode's screening effect is critical for adjusting the PV effect which depends on the thickness of the thin films. Experimentally, a moderate efficiency of 0.28% was obtained in PLZT thin films [59]. As demonstrated quantitatively on PLZT films in contact with various electrodes, a critical thickness exists that results in the greatest possible photovoltaic current (see Figure 1.14) [60]. This critical thickness is the transition point between a regime in which photovoltaic current is constrained by the electrodes' polarization screening and a regime in which photovoltaic current is commanded by the Schottky-induced space charge region.

Poosanaas et al., proposed a model based on the Glass model for the photovoltaic effect, which qualitatively corresponds with the previous numerical results [59]. The photovoltaic current in WO_3-doped PLZT films was anticipated to be optimal at a thickness of 33 µm [82].

It is important to note that a PCE of 0.6 percent was reached in $BaTiO_3$ thin films with a thickness less than 100 nm, which represents 4.5 times increase in yield over bulk crystals [47]. In this work, the observed increase at low thickness comes from the bulk photovoltaic effect which is greatly enhanced when the thickness of the crystal is reduced so that it is comparable to the characteristic shift in the nonthermalized carriers yielding the photoinduced electric field.

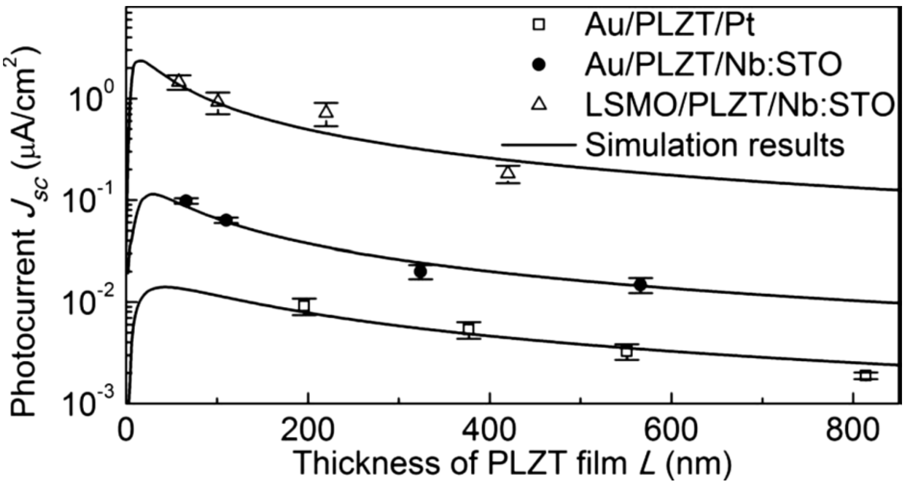

Figure 1.14 Short-circuit photovoltaic current vs thickness of PLZT thin film, as determined from calculations with different electrodes [60].

1.3.4 Defects

The consequences of defects on PV properties are difficult to predict. Similar to the Schottky barrier effect, defects such as oxygen vacancies can also generate built-in fields and affect the photovoltaic characteristics of FE materials [62] and their switchability [55]. Moreover, it is generally regarded that oxygen vacancies are the source of leakage in FE materials, resulting in a degradation of the photovoltaic effects [83]. As a result, demanding approaches are used to eliminate oxygen vacancies in FE materials in order to increase the performance of PV devices.

Instead of being unfavorable to PV performance, oxygen vacancies may also be advantageous by modifying interfacial screening charges, producing trapping centers, and increasing sub-bandgap absorption in photovoltaic devices. Moubah et al. demonstrated that PV effects are only detectable in a single domain BFO following the application of an electric field with a lower intensity than the coercive field under illumination [55]. There is an explanation for this: the electric field creates oxygen vacancies that are then driven to the BFO/electrode contact, where the oxygen vacancies can reduce the energy barrier, allowing for the measurable photocurrent. Another example demonstrates that the BTO/p-Si samples with abundant oxygen vacancies exhibit a higher photovoltaic response, which is connected to the formation of p-n junctions at the interfaces between the oxygen vacancy space charge layer and the p-doped silicon [84]. On the other hand, oxygen vacancies have the ability to significantly reduce the leakage of FE materials under specific conditions. Shuai et al. [85] indicate that leakage is reduced when more Mn ions are included in the BTO films, thereby increasing the number of oxygen vacancies available for charge compensation, and thereby serving as trapping centers in the BTO bandgap [85]. Additionally, the defect centers located in the bandgap may be able to induce sub-bandgap levels, which can not only increase the solar spectrum's absorption but also create an asymmetry in the k space between the charge generation and recombination processes that meet the BPVE condition [86]. According to the findings of these new investigations, effective defects control is critical to the production of ferroelectric-based PV devices.

1.3.5 Bandgap engineering

When it comes to photovoltaic devices, the ferroelectric material should have a bandgap close to the solar spectrum maximum, which is 1.4 eV. Most of ferroelectrics have a bandgap in the ultraviolet region of the solar spectrum (see Figure 1.15). This large bandgap is associated with the ferroelectric oxide perovskite’s electronic structure, which is defined by the valence band maximum produced by the oxygen 2p orbital and the conduction band minimum produced by the transition metal d orbital [87].

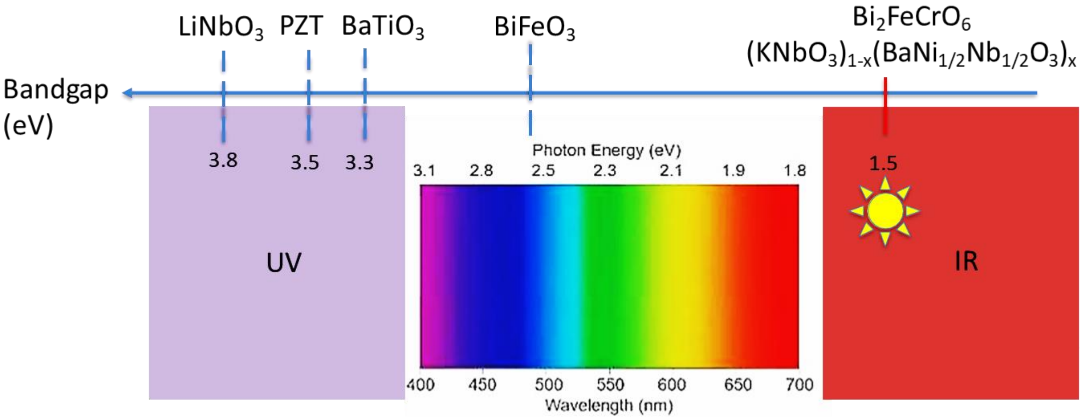

Figure 1.15. Various perovskite oxides with their bandgap.

One of the ideas is to tune the chemical ordering of materials using a narrow bandgap material to decrease the bandgap. Nechache et al. [88] were able to produce a multilayer structure of the same material in three layers, Bi_2FeCrO_6 (BFCO), with each layer absorbing a different portion of the solar spectrum due to the layers in varied chemical ordering. The researchers attained the best efficiency (8.1 %) ever recorded for traditional ferroelectrics using a multilayered structure, with typical photovoltaic outputs Jsc = 11.7 mA/cm^2 and Voc = 0.79 V under AM1.5 illumination. Additionally, prior work on Bi_2FeCrO_6 thin films reported a 6.5 % PCE under red laser illumination, with a photovoltaic current density of 0.99 mA/cm^2, one of the highest ever recorded [80].

Another way to minimize the bandgap is to experiment with chemistry, such as solid solutions or doping. Grinberg et al., in 2013 [89], revealed that the bandgap was 1.46 eV for the compound $(KNbO_3)_{(1-x)}(BaNi_{0.5}Nb_{0.5}O_3)_x$ (KBNN), which is a combination of a ferroelectric ($KNbO_3$) and an oxygen-deficient perovskite ($BaNi_{1/2}Nb_{1/2}O_3$).

In conclusion, to solve the drawbacks of ferroelectrics with big gaps and poor photovoltaic characteristics, significant effort has been expended to reduce the bandgap of the absorbing ferroelectric material as mentioned in Table 1.1.

	E_g (eV)
$BiMnO_3$	1.2
Bi_2FeCrO_6	1.4–2.0
$LiNbO_3$	3.78
$KNbO_3$	3.3
$(KNO)_x(BNNO)_{(1-x)}$	1.5–3
$KBiFe_2O_5$	1.6

Table 1.1 Summary of bandgap of different perovskite oxides [28].

Chapter 2

Growth and characterization techniques

Contents

This chapter includes first a brief introduction of the techniques used for the growth and the characterization of the oxide thin films, including pulsed laser deposition (PLD), atomic force microscopy (AFM), and X-Ray diffraction (XRD). In a second part, the structuration of the thin films into capacitor devices is presented: the sequence of fabrication steps, based on photolithography and sputtering processes. In the last part, the electrical characterizations of PZT thin films integrated into capacitor geometry are described to investigate their dielectric, ferroelectric, and photovoltaic properties. I myself did thin film growth, device fabrication, and electrical measurements for all the devices used in this thesis.

2.1 Growth and characterization of oxide thin films

2.1.1 Pulsed laser deposition (PLD)

Pulsed laser deposition is a thin film deposition technique based on the laser ablation process. A pulsed laser beam of high intensity is directed within a vacuum chamber where it is absorbed by the target (material that has to be deposited) and produces material ejection in the form of a plasma plume above a certain absorbed power density. The threshold of power density for ablation depends on many parameters such as target material, the wavelength of the laser, duration of the laser pulse, etc. The plasma plume, induced in the ablation process, contains the stoichiometric composition of the target material, which is transferred towards the substrate heated up to a certain high temperature. Then the material condenses into a high-quality epitaxial thin film if the growth parameters are well-tuned. The deposition can be processed under a high vacuum or in the presence of background gas such as an inert (argon) or reactive (oxygen, N_2O) gas. A sketch of the PLD setup is illustrated in Figure 2.1. For the growth performed during this Ph.D., there is no dedicated annealing process after the deposition apart from the cooling to room temperature, which typically takes 1 to 2 hours under an oxygen atmosphere.

PLD is a versatile physical vapor deposition (PVD) technique, in which several parameters, such as the laser fluence on the target (incident energy per unit area), the pulse rate, the gas pressure, and the substrate temperature, need to be regulated to control the growth process. Furthermore, by adjusting the pulse rate, it is possible to obtain exquisite control of film thickness down to the level of an atomic monolayer. It is quite simple to create multi-layered films or heterostructures of various complex materials by ablation of a variety of targets in a sequential fashion. A significant aspect of PLD is that, for a wide range of target materials including ternary and quaternary oxides, the target stoichiometry can be preserved in the films that are formed during the deposition process. The substrate can be heated to high temperatures to achieve better crystallinity, typically ranging from 500°C to 800°C for perovskite oxide films.

During the growth, a KrF excimer laser at (UV) 248nm wavelength is used in this work. The growth parameters used for the different oxides are summarized in the next section and are based on optimization work performed in the OXIDE team. For all oxides, the laser frequency is 2-5 Hz, the incident fluence is in the range of 2-4 J/cm^2, the pressure in the vacuum chamber is about $2*10^{-6}$ Torr before the deposition, the distance between target and substrate is 5 cm, and the gas used for the deposition of PZT is N_2O and O_2 for $SrRuO_3$ (SRO), $SrTiO_3$ (STO) and $La_{2/3}Sr_{1/3}MnO_3$ (LSMO).

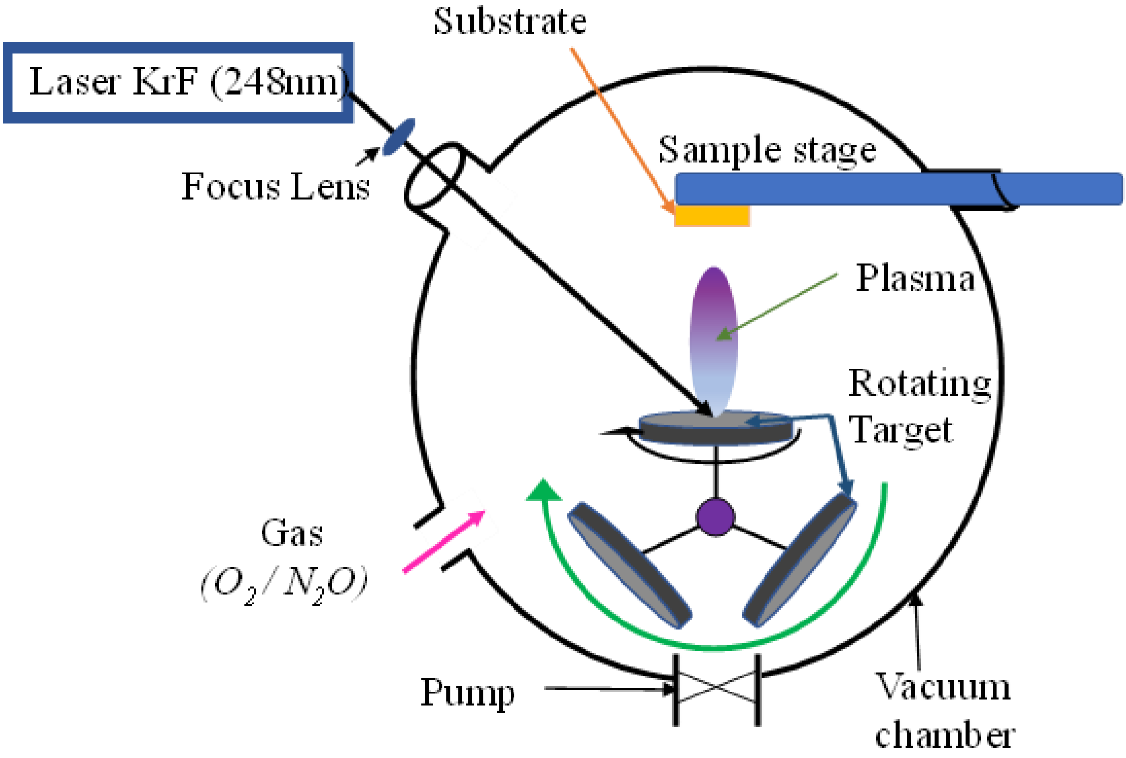

Figure 2.1. A sketch of pulsed laser deposition setup.

2.1.2 Growth parameters

In this work, $PbZr_{0.2}Ti_{0.8}O_3/SrRuO_3$, $PbZr_{0.2}Ti_{0.8}O_3/La_{2/3}Sr_{1/3}MnO_3$, $SrTiO_3$(1nm)/$PbZr_{0.2}Ti_{0.8}O_3$ /$SrRuO_3$, $PbZr_{0.2}Ti_{0.8}O_3/SrTiO_3$(1nm)/$SrRuO_3$, and $SrTiO_3$(1nm)/$PbZr_{0.2}Ti_{0.8}O_3/La_{2/3}Sr_{1/3}MnO_3$ layers have been epitaxially grown by PLD technique on a $SrTiO_3$ (STO) substrate of (001) orientation.

Substrate and buffer layer: Strontium titanate ($SrTiO_3$)

$SrTiO_3$ (STO) being an ABO_3 perovskite structure is used as the substrate in this thesis. It has a cubic crystal structure. A (001) oriented STO substrate with lateral dimensions of 5x5 mm^2 is first prepared before using it for PLD growth. STO can be either SrO or TiO_2 terminated. A single-terminated substrate promotes high-quality epitaxial films. To prepare a TiO_2 terminated STO substrate, a chemical process has been used [90]. In this chemical process, a STO substrate is first put in deionized (DI) water under ultrasonics for several minutes (~30 min). Then the substrate is etched in a buffered hydrofluoric acid (HF), which contains a 7:1 volume ratio of 40% NH_4F in water to 49% HF in water, for about 1min. Then the substrate is rinsed with deionized water followed by N_2 blowing to dry it out. In the end, the substrates get annealed in a tube furnace, for 3h at 950°C under pure O_2 flow.

Also, 1nm thick STO is used as an insulating buffer layer in some samples at the top (STO (1nm)/PZT/LSMO//STO) or bottom (PZT/STO(1nm)/LSMO//STO) interfaces to investigate the effect of interface on the electrical properties. Growth parameters of the epitaxial STO buffer layer are mentioned in table 2.1.

Parameter	STO (1nm)
O_2 (mTorr)	120
Fluence (J/cm^2)	2.8
Ablated area (cm^2)	0.012
Temperature (°C)	630
Substrate-target distance (cm)	5
Frequency (Hz)	2
Thickness (nm)	1
Deposition rate (pulses/unit cell)	40

Table 2.1 PLD growth parameters used for the epitaxial growth of buffer layer of STO.

Bottom electrode: Strontium ruthenate ($SrRuO_3$)

After preparing the STO substrate, the next step is epitaxial growth of the bottom electrode such as SRO using the PLD technique. At room temperature, SRO has an orthorhombic crystal structure and a pseudocubic lattice parameter of a = 3.928 Å [91], which is quite similar to STO (a = 3905 Å) [92]. Also, it is chemically resistant to most acids. It is a conductive oxide perovskite with electrical resistivity of about 200 µOhm.cm at room temperature, which makes it an ideal candidate for electrodes in thin film-based capacitors and heterostructures. All the epitaxial growth parameters are listed in table 2.2.

Parameter	SRO
O_2 (mTorr)	120
Fluence (J/cm^2)	2.8
Ablated area (cm^2)	0.018
Temperature (°C)	630
Substrate-target distance (cm)	5
Frequency (Hz)	5
Thickness (nm)	30-40
Deposition rate (pulses/unit cell)	30

Table 2.2 PLD growth parameters used for the epitaxial growth of bottom electrode of SRO on STO substrate.

Bottom electrode: Lanthanum strontium manganite ($La_{2/3}Sr_{1/3}MnO_3$)

Another bottom electrode used in this work is LSMO. LSMO is a good conductive oxide with electrical resistivity of about 1 mOhm.cm at room temperature that serves the purpose of the electrode. It has a rhombohedral structure with pseudo-cubic lattice parameter a = 3.876 Å [92] which shows a small lattice mismatch with STO substrate. All the parameters related to the epitaxial growth of LSMO are shown in table 2.3 below.

Parameter	LSMO
O_2 (mTorr)	120
Fluence (J/cm^2)	2.8
Ablated area (cm^2)	0.012
Temperature (°C)	630
Substrate-target distance (cm)	5
Frequency (Hz)	2
Thickness (nm)	25-30
Deposition rate (pulses/unit cell)	25

Table 2.3 PLD growth parameters used for the epitaxial growth of bottom electrode of LSMO on STO substrate.

Ferroelectric layer: Lead zirconate titanate ($PbZr_{0.2}Ti_{0.8}O_3$)

All the work in this thesis is carried out on PZT ferroelectric thin film. To have a high value of polarization a composition of 20/80 is used for Zr/Ti. It has a tetragonal structure with lattice parameters of a= 3.96 Å and c = 4.13 Å. After the deposition of the bottom electrode on the STO substrate, PZT films of 100-120nm thickness are grown in N_2O under the pressure of 120mTorr, other conditions can be seen in table 2.4.

Parameter	PZT
N_2O (mTorr)	120
Fluence (J/cm^2)	2.8
Ablated area (cm^2)	0.012
Temperature (°C)	630
Substrate-target distance (cm)	5
Frequency (Hz)	5
Thickness (nm)	100
Deposition rate (pulses/unit cell)	15

Table 2.4 PLD growth parameters used for the epitaxial growth of ferroelectric PZT thin film above SRO or LSMO bottom electrode.

2.1.3 Atomic force microscopy (AFM)

Atomic force microscopy (AFM) is a scanning probe method that is used to determine the topographies and other surface properties of a wide range of materials. AFM operates by scanning a tip along the surface of a sample at nanoscale resolution. To conduct a scan, the sample is positioned on a piezoelectric scanner, which accurately controls the distance between the tip and the surface, as well as the force applied to the tip. When the tip is brought into contact with a sample, the forces (F) between the tip and the sample surface cause the cantilever to deflect (Δx) in accordance with Hooke's law.

$$F = -k\Delta x \qquad (2.1)$$

Where k is the cantilever's spring constant. A laser-focused on the rear of the cantilever detects the deflection of the cantilever caused by forces operating on the tip. A photodetector detects the laser when it is reflected. The movement of the laser light on the photodetector gives the deflection of the cantilever during a scan.

In this work, AFM is used in contact mode to characterize the surface of substrates and samples, and to extract the roughness (R_{rms} root mean square). The tip is "dragged" over the surface in contact mode. The cantilever's defection is maintained at a constant value. Additionally, the image can be altered significantly by frictional and adhesive forces. Figure 2.2 illustrates a simplified schematic of the AFM setup. The AFM utilized is a Bruker Innova AFM with a tip made of silicon nitride.

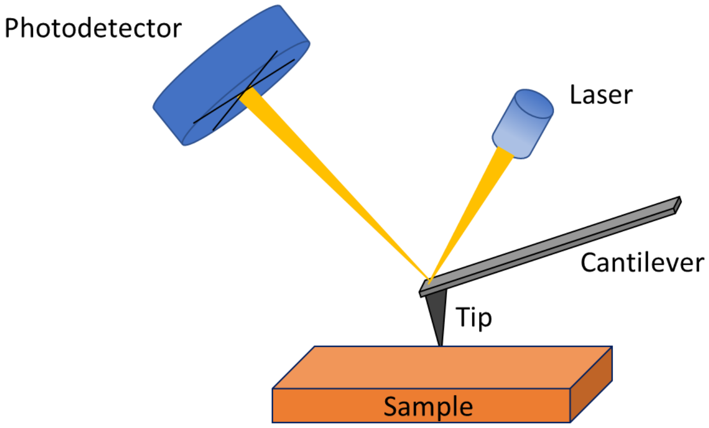

Figure 2.2. Setup of atomic force microscopy (AFM).

2.1.4 X-ray diffraction (XRD)

The crystalline quality of all the samples has been characterized by X-ray diffraction at C2N by Thomas Maroutian (OXIDE team).

X-ray diffraction (XRD) is an analysis technique used to determine the crystal structure of a material. It works on the principle of interaction of crystalline matter with incident X-rays. Due to that, X-rays scattered by the material result in different scattering angles and intensities, which can be measured to give information about crystal structure, lattice parameters and thickness of the material. The wavelength of the X-rays is similar to the spacing between the crystal planes, as shown in Figure 2.3 a. X-rays scattered by a regular array of lattice planes interact either destructively to cancel each other or constructively to add up. This gives the resulting diffraction pattern based on Bragg's law:

$$n\lambda = 2d_{hkl}\sin\theta_{hkl} \qquad (2.2)$$

Where, h k l are Miller indices of parallel planes, n is an integer showing order of diffraction, λ is the wavelength of X-rays, d is the distance between planes and θ is the angle between incident X-rays and scattering plane. Interference is constructive when the phase shift is multiple of 2π.

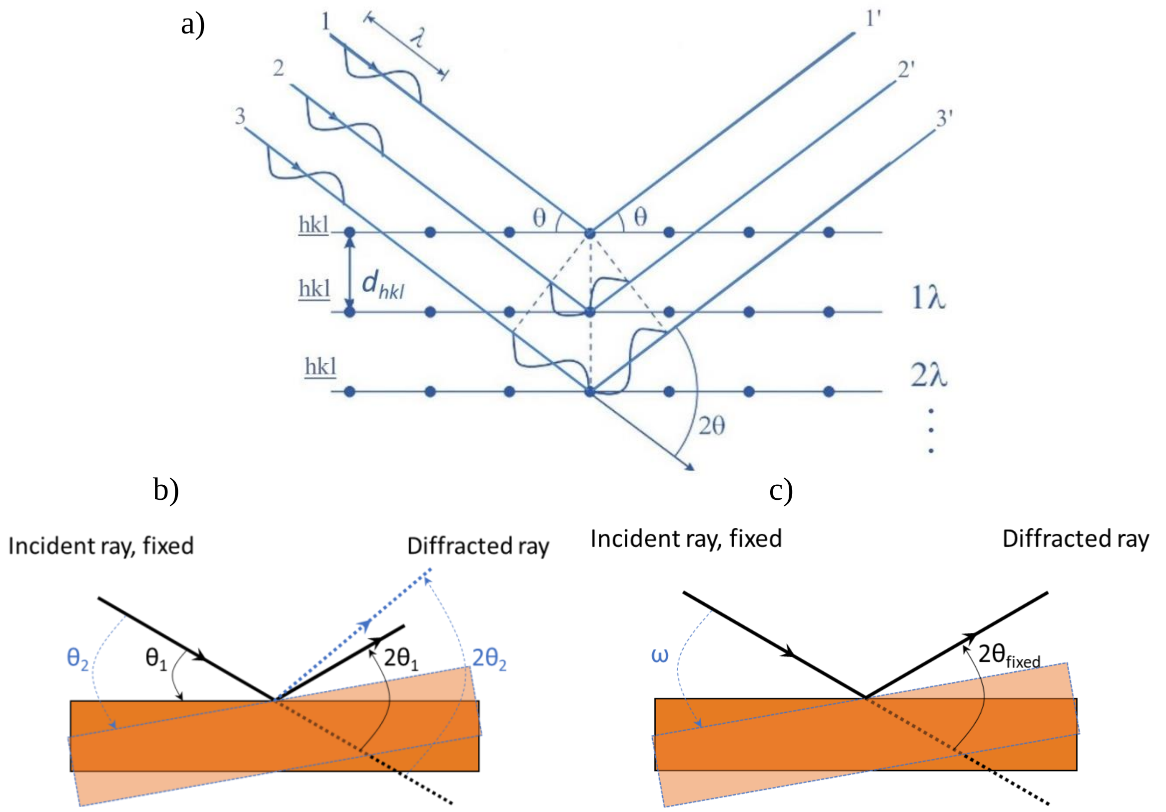

Figure 2.3. Schematic of a) Bragg's law condition, b) θ-2θ measurement and c) ω scan.

A θ-2θ curve around the PZT Bragg peaks 001, 002, 003, and 004 is presented in Figure 2.4, showing also both LSMO and STO peaks. The out-of-plane c lattice parameter of LSMO is 0.386nm and the film thickness was found to be 30nm from the analysis of the thickness fringes. The thickness of the PZT thin films for calibration was measured using X-ray reflectivity (XRR). The thickness of PZT is measured as 120 nm. The out-of-plane c lattice parameter of PZT is 0.413nm, which is consistent with its tetragonal structure for the $Pb(Zr_{0.2},Ti_{0.8})O_3$ composition. The rocking curve around the 002 PZT Bragg peak can be seen in Figure 2.5 and has a full width at half maximum of 0.12° indicating a good crystalline quality of the PZT layer with low mosaicity.

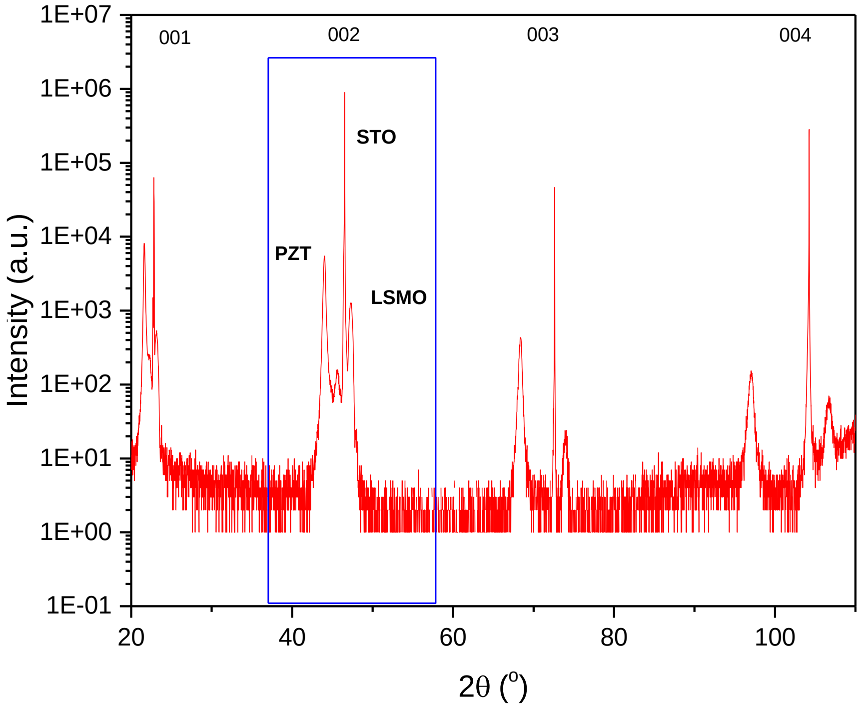

Figure 2.4. θ-2θ XRD curve of PZT/LSMO/STO.

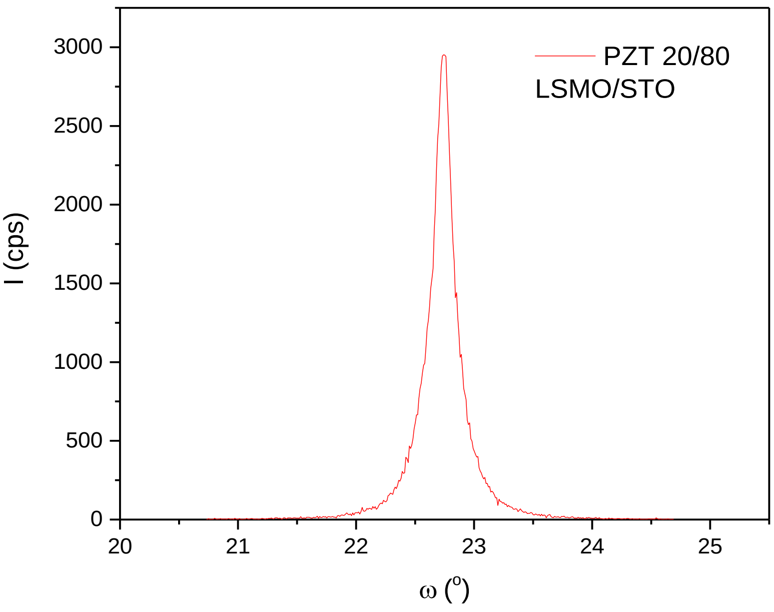

Figure 2.5. The rocking curve of PZT film 002 Bragg peak.

2.2. Structuration of oxide thin films into capacitor devices

This part describes the patterning of the thin films into capacitor's geometries in order to perform the ferroelectric and photovoltaic measurements. This patterning includes various chemical and physical processes described in the sections below.

2.2.1 Patterning steps

The capacitors are fabricated by deposition of top electrode on multilayer PZT sample following different steps shown schematically in Figure 2.6 a) and a microscopic image of the final capacitors is presented in Figure 2.6 b). After the growth of PZT thin film by PLD, a sequence of photolithography-deposition-lift-off is performed to fabricate top electrode pads. We want to perform the ferroelectric and photovoltaic measurements on pads of different lateral sizes from 200x200 µm² to 10x10 µm² and keep homogeneous illumination. This requires connecting electrically these pads to bigger pads next to them, insulated from the PZT layer, where the tip will be placed (see Figure 2.9(a)). So, the first sequence of photolithography-deposition-lift-off is performed to fabricate the 200x200 µm² pads of insulating Si_3N_4 (SiN). The photolithography step is explained in detail in the next section, as well as the deposition of an insulating layer of SiN by the sputtering technique. The purpose of this insulating layer is to connect the small size electrodes electrically to larger metal electrodes while keeping the latter insulated from the ferroelectric layer (Figure 2.9(a)). A second sequence of photolithography-deposition-lift-off is performed to fabricate the top electrode pads of Pt or ITO with dimensions ranging from 200x200µm² and 100x100µm² to 10x10µm². In this work, two electrode materials are used: Pt being widely used in the literature and the transparent ITO.

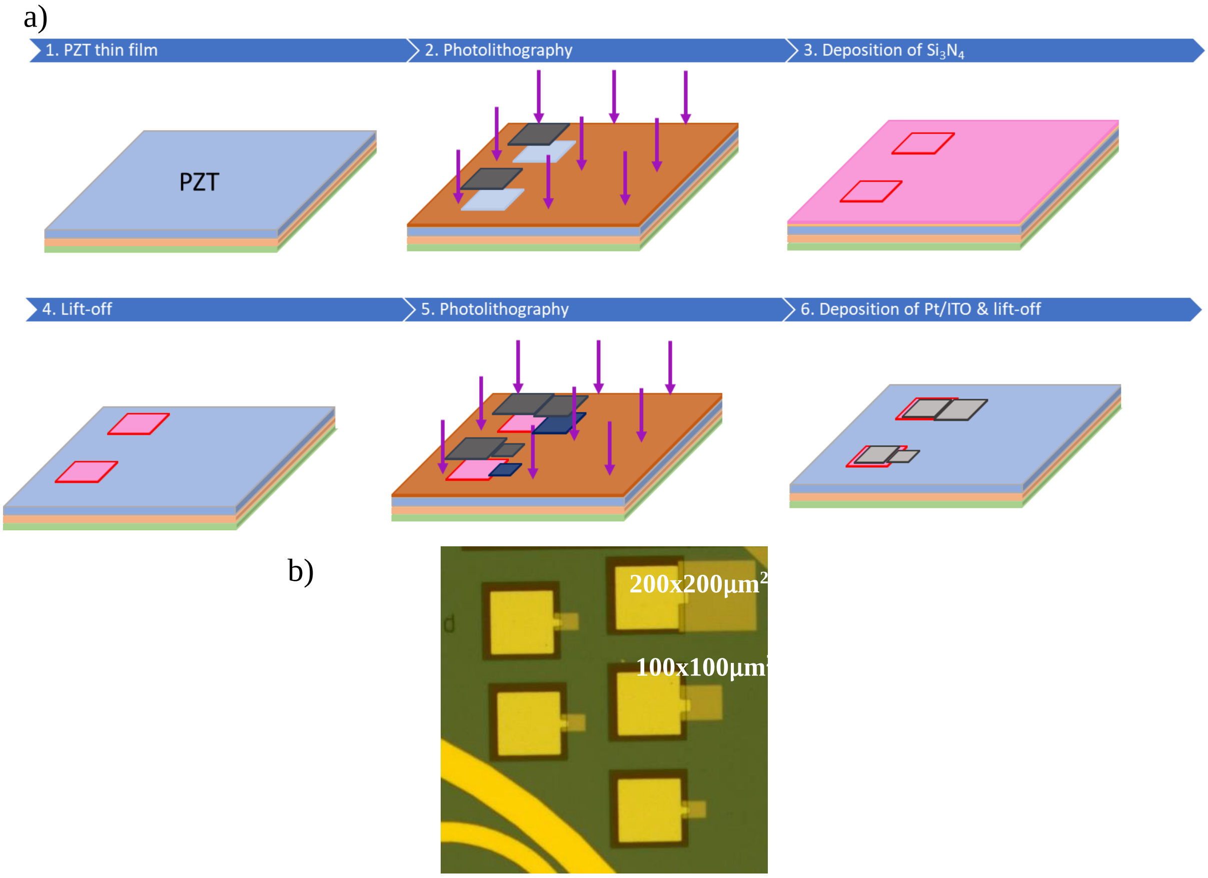

Figure 2.6. a) Fabrication steps involved in the realization of PZT based capacitor device. b) A microscopic image at the end of the process.

2.2.2 Photolithography

Photolithography is also known as optical lithography and is a technique to transfer geometric patterns widely used in microfabrication. A layer of photoresist is exposed to UV illumination. These photoresists are sensitive to light and can be developed to define structures with controlled design (transferred from a mask). The main steps in the lithography procedure can be seen in Figure 2.7.

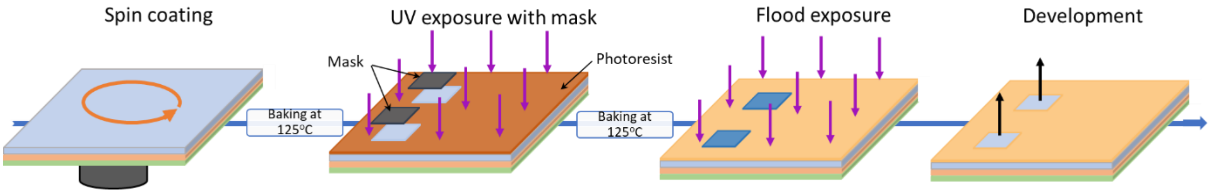

Figure 2.7 Main steps involved in photolithography.

The main recipe for the photolithography used in this work is described as follows:

1. Epitaxially grown PZT samples were cleaned with acetone and isopropanol followed by baking for 10min at 110° C to dehydrate the sample properly.
2. Spin coating with 1 drop of HDMS solution, for better adhesion of photoresist, for 6 sec at a speed of 6000 rpm followed by 45 sec at 4000 rpm.
3. Again, spin coating with AZ5214E resist (Photoactive resist) for 6 sec at a speed of 6000 rpm followed by 45 sec at 4000 rpm to a thickness of 1-1.2 µm.
4. Sample is baked on a hot plate for 1 min at 125 ° C to dry the solvent.
5. Exposure of photoresist to UV using a chromium photomask for 9 sec to reach a 15 mJ/cm^2 exposure dose, using MJB4 Suss MicroTec system. The exposed part of the resist will become soluble.
6. Image reversal process: baking of sample again for 1 min at 125 ° C will make the UV exposed part insoluble.
7. Flood exposure of UV, without the mask for 30 sec will expose all the samples, making the parts that were not exposed during step 5 now soluble.

8. Sample is kept in MIF826 development solution for 30 sec followed by 30 sec in DI water which will remove the soluble part leaving square holes in the resist, reproducing the design on the mask.

2.2.3 Sputtering

Sputter deposition is a high vacuum technique, that belongs to physical vapor deposition processes. The principle of sputtering is the use of a plasma (ionized gas such as Ar+) to release the atoms of the target material, which are then deposited on the substrate as shown in Figure 2.8. After the lithography process, dielectric SiN, Pt, and ITO were deposited using the sputtering technique.

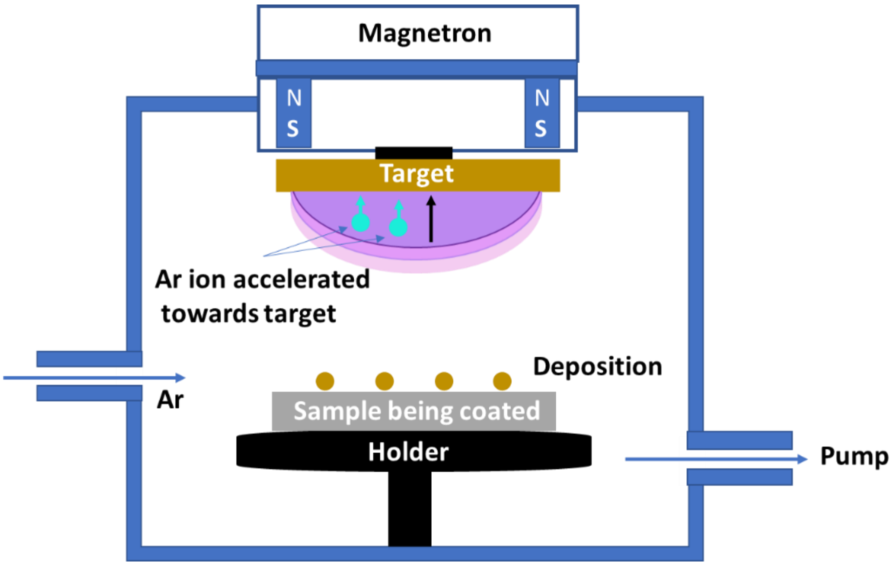

Figure 2.8. Sputtering Deposition setup.

Parameter	Si_3N_4	Pt	ITO
Pressure (Pa)	1.5	0.57	0.4
Gas atmosphere (mass flow)	N_2 (50 sccm), Ar (30 sccm)	Ar (30 sccm)	Ar (200sccm), O_2 (1sccm)
Power	RF 500 W	DC 150 W	RF 200 W
Pre-deposition sputtering duration (min)	10	1	10
Deposition rate (nm/min)	8	13	20
Thickness (nm)	200	8	20

Table 2.5. Parameters used while sputtering deposition of Si_3N_4, Pt, and ITO.

Insulating Si_3N_4 (SiN) is sputter deposited as mentioned (in step 4, Figure 2.7) followed by a lift-off process in which the sample is kept in acetone for 1-2 hours. After the repetition of all lithography steps, Pt or ITO was deposited by sputtering, and the final capacitors are obtained by the final lift-off process.

2.3 Electrical characterizations

All the capacitor devices based on PZT thin film were electrically characterized for ferroelectric and photovoltaic properties. For this, methods and setups used in this work are described briefly in the following sections.

2.3.1 Dielectric measurements

A capacitance measurement is required to obtain the dielectric constant of the ferroelectric thin film. This measurement is carried out using Hioki 3532-50 LCR HiTester (impedance meter) with Keithley 2400 (source meter) connected to 2 probes of a probe station. One tip is connected to the top electrode and the other one to the metallic disc which is attached to the sample using silver paste in order to connect to the bottom electrode. The bottom electrode is grounded as shown in Figure 2.9 a. The measurements were carried out at 1kHz to 1000kHz frequency. The dielectric constant (ε_r) of ferroelectric film can be obtained using the capacitance values measured using the formula:

$$C = \varepsilon_0 \varepsilon_r \frac{1}{d} A \qquad (2.3)$$

Where A is the area of the capacitor defined by the top electrode, d is the thickness of the PZT layer, and ε_0 (8.85×10^{-12} F/m) is the dielectric constant of free space.

The sign convention used for polarization up state and down state in this thesis can be seen in Figure 2.9 b-c. Note that in chapter 4, the dielectric constant was extracted at different polarizations as the sample was being poled before and after each capacitance measurements.

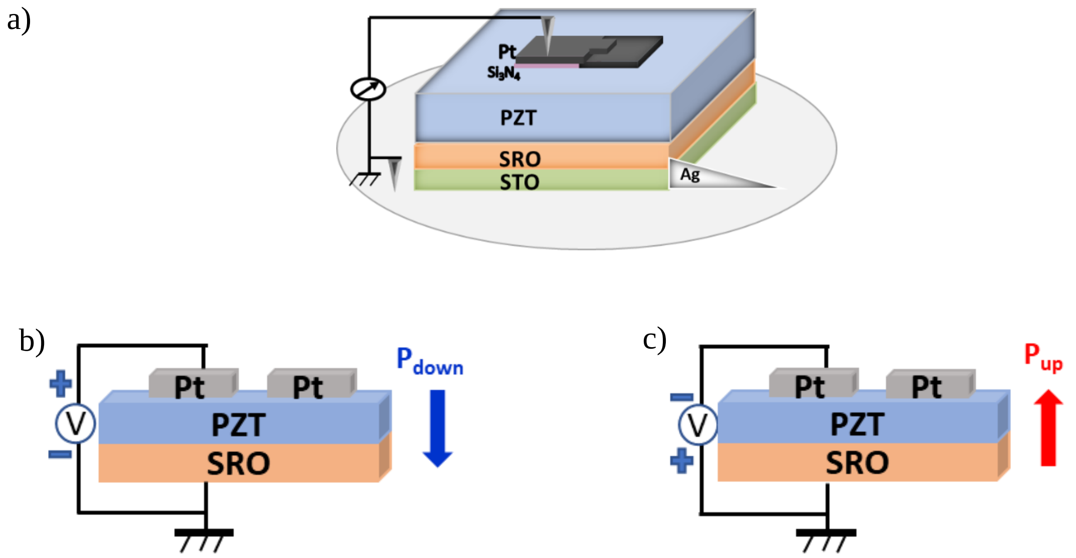

Figure 2.9 a) Sample connected to the two probes for electrical measurements. b,c) Sign convention for polarization direction in P down and P up state.

2.3.2 Ferroelectric measurements

The ferroelectric properties were analyzed on different PZT ferroelectric thin films integrated into capacitor geometry between the top and bottom electrodes using a TF Analyzer 1000 AixACCT (ferroelectric tester). TF Analyzer is connected to the two probes, brought into contact with the top and bottom electrodes. As mentioned in the last part, the first tip is placed directly on the top electrode. The second tip is placed on a conductive disc in contact with the bottom electrode through a silver paste, as shown in Figure 2.9a. In our capacitor devices, voltage is applied at the top electrode and the bottom one is grounded.

The polarization measurement is actually a measurement of charge in the capacitor given by

$$Q = P\,A \qquad (2.4)$$

where Q is the total charge in the ferroelectric, A is the capacitor area and P is the polarization [93]. Polarization can thus be obtained by integration of measured switching current (I) with respect to time,

$$P = \frac{\int I dt}{A} \qquad (2.5)$$

2.3.2.1 Classical ferroelectric loop

Polarization measurements are obtained by the dynamic hysteresis method (DHM). In this thesis, a triangular waveform is used for all the ferroelectric measurements, as shown in Figure 2.10 a. The first pulse is a prepoling pulse, the P-V loop can be obtained from the negative part of the second pulse (in green) combined with the positive part of the fourth pulse (in orange). Sketch of DHM ferroelectric measurement with its corresponding current loop can be seen in Figures 2.10 b and c. All presented ferroelectric measurements were obtained at 1kHz frequency at room temperature.

It is crucial to understand the other contributions to the measured current, that may come while switching the ferroelectric polarization. Figure 2.11 summarizes the different cases which can arise when measuring a ferroelectric loop.

In Figure 2.11 a, the loop is an example of an ideal ferroelectric loop with sharp ends of the hysteresis loop and sharp switching current peaks. When sweeping voltage following the waveform, ferroelectric switching gives indeed current switching peaks at the coercive field. In addition, all dielectric materials exhibit capacitance (C) and dielectric current charging given by CdV/dt. In case of pure dielectric charging, the polarization measurement will show a straight line and no loop, as shown in Figure 2.11 b. For a leaky dielectric material, current measurements will show only leakage such as Ohmic conduction (Figure c) or semiconducting exponential conductivity (Figure d), giving some apparent polarization with no sign of ferroelectric behavior (no switching). Whereas, in Figures e, f & g, all hysteresis loops are ferroelectric but with a slightly distorted shape, and by analyzing the first three cases above it can be observed by the current loop that there is additional contribution to the ferroelectric one. It is a combination of contributions from dielectric charging and different leakage sources. In ‘h’ case, the hysteresis loop looks like a ferroelectric loop, but special attention has to be paid when analyzing the loop by studying the current loop. This is not a ferroelectric loop but only a combination of dielectric charging with leakage current! The very last ‘i’ case shows an example of real loop with all contributions together giving a huge overestimate of polarization. The leakage behavior can be decreased by optimizing growth conditions, avoiding electrical breakdown, and performing the measurements at higher frequencies.

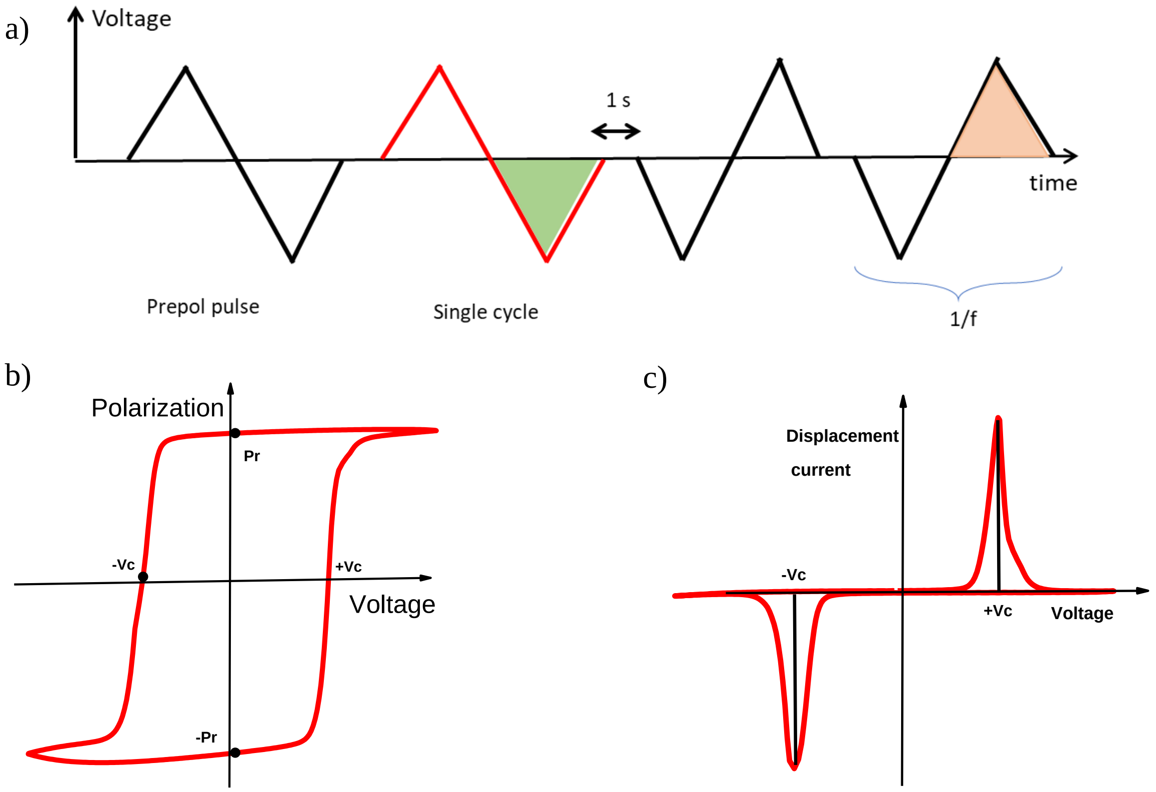

Figure 2.10 a) Triangular wave pulse applied in a conventional dynamic hysteresis (DHM). b) DHM ferroelectric hysteresis loop and c) corresponding DHM current loop.

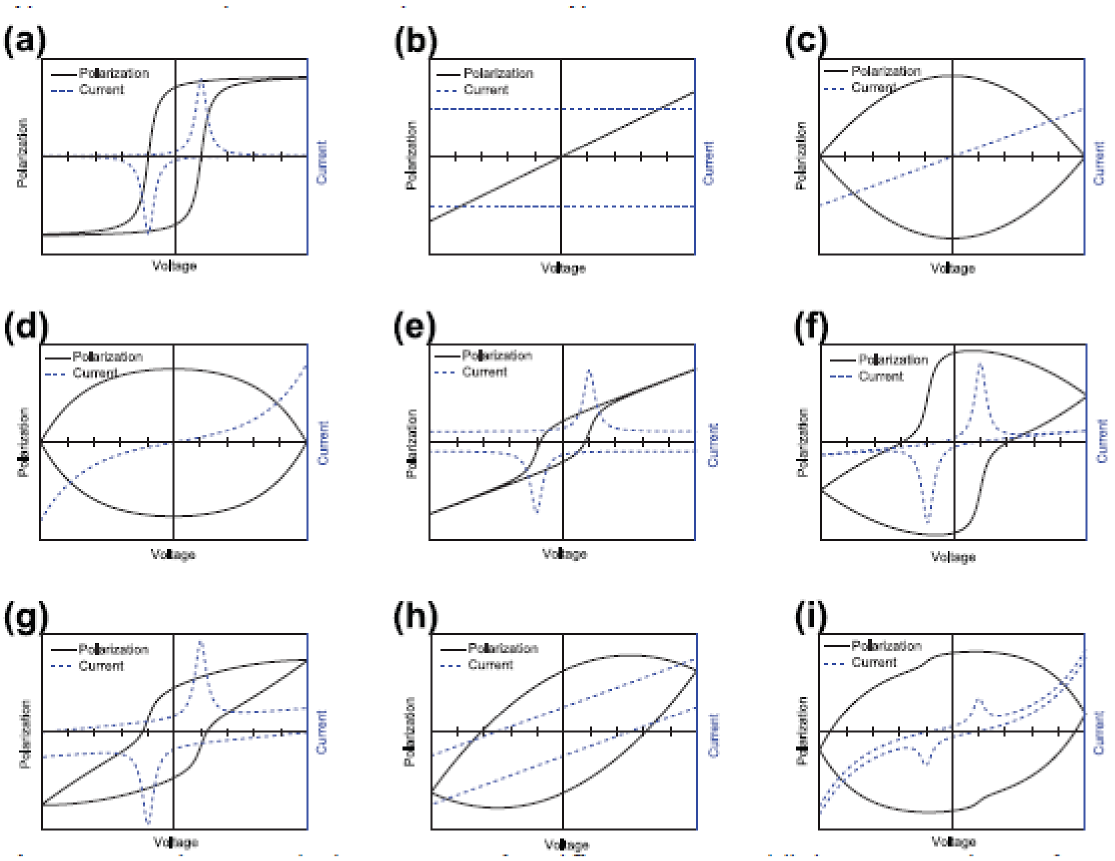

Figure 2.11. [Taken from Everhardt, 2017] [94] Polarization hysteresis loops and their corresponding current loops due to different sources. a) Pure ferroelectric hysteresis loop. b) Due to dielectric charging. c) Due to ohmic resistance (linear leakage). d) Exponential leakage. e) Combination of ferroelectric and dielectric contributions. f) Combination of ferroelectric and ohmic leakage. g) Combination of ferroelectric, ohmic leakage, and dielectric contribution. h) Combination of ohmic leakage and dielectric contribution. i) small polarization & dielectric contributions superimposed with exponential leakage.

Some important points while measuring a ferroelectric hysteresis loop are:

- The measurement frequency (inverse of the waveform's period) will affect the rate at which the voltage varies per unit of time. In order to sustain polarization at higher frequencies, the current needs to be increased. Dielectric contribution follows the same. Consequently, the current's role in polarization and charging increases with increasing frequency. Leakage currents, on the other hand, are independent of frequency. So, the apparent contribution of leakage current which adds to polarization changes with frequency. That is why higher frequencies are recommended to have a lower leakage contribution to the ferroelectric loop.
- In the ferroelectric hysteresis measurement, the voltage range must be adjusted. Increasing voltage beyond the coercive field where current switching peaks are present does not result in extra polarization. If it does, then the measurement indicates non-intrinsic polarization. In dielectric charging, however, greater voltage increases apparent polarization. Leakage will also cause greater apparent polarization

and coercive field. When the field is excessively strong, leakage becomes a major cause of apparent polarization.

The best ferroelectric measurement may be obtained by using a triangle waveform that is slightly above the coercive field and has the highest frequency possible while minimizing measurement noise. In this thesis, the equipment allowed us to apply a maximum of 1 kHz frequency.

2.3.2.2 Positive-up-negative-down (PUND) loop

In the previous section, it is observed that there can be some dielectric and leakage contributions, inducing spurious components in the measured polarization, leading to an overestimation of the polarization value. To distinguish between ferroelectric and non-ferroelectric contributions, there is an effective method called Positive-Up-Negative-Down (PUND) method. It is especially effective to remove the leakage current contribution.

The PUND waveform has one writing pulse and four reading pulses: two in the up direction and the other two in the down direction as can be seen in Figure 2.12 a. After the writing pulse, the first pulse denoted by ‘P’ will induce ferroelectric switching while the next pulse denoted by ‘U’ will be non-switchable and include only non-ferroelectric contributions. Similarly, on the other side, the negative pulse denoted by ‘N’ will switch back the polarization and the ‘D’ pulse will show a non-switching character with other contributions. By subtracting the measured current of the second non-switching pulse from the switching one, a sharp hysteresis without dielectric and leakage contributions can be achieved. One example of a loop for a PZT 20/80 sample is shown in Figure 2.12 b-c, where the dielectric and leakage effects are removed and the difference between DHM and PUND loops can be seen clearly. The PUND waveform used in this thesis has a pulse width of 0.5ms and a delay of 1ms.

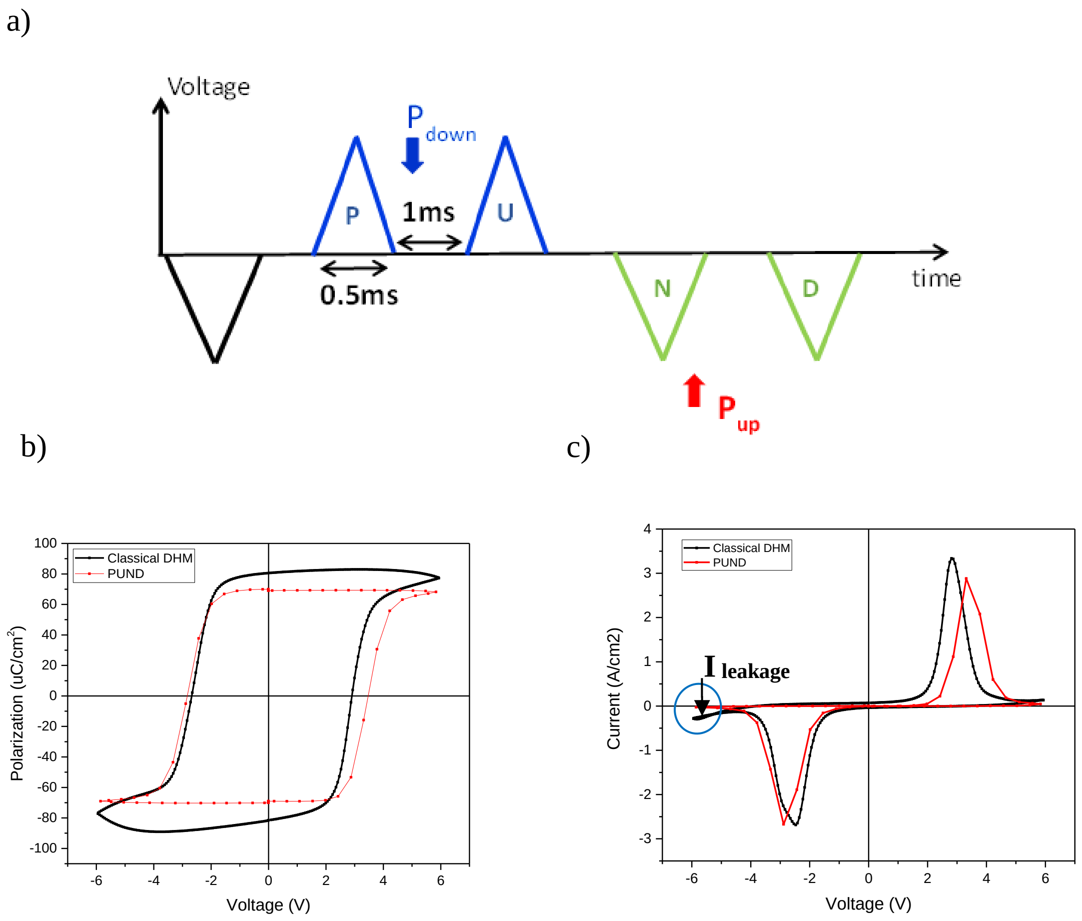

Figure 2.12. a) Triangular pulse sequence used in a PUND measurement. b) Polarization loop with classical DHM measurement and loop with PUND method for PZT 20/80 sample. c) Corresponding current loop from classical and PUND measurements for PZT 20/80 sample.

2.3.3 Photovoltaic properties

The setup for photovoltaic measurements is shown in Figure 2.13 a. Various measurements such as I(V), I(t), and Voc(t) (open circuit voltage) were carried out on the different PZT samples with capacitor geometry as mentioned in section 2.1.2. These measurements were made using a Keithley 2636B source meter to apply and measure current and voltage under UV illumination. The UV light is shined on the top electrode using diodes (LED) or Xe lamp (equipped with a fiber). The Xe lamp is equipped with a spectrometer having a scan range in wavelength from 0 to 1400nm. The UV source was placed above the top electrode at a distance of about 1-1.5cm from the sample surface, controlled manually. Experimentally, the Xe lamp power for wavelengths below 300 nm becomes insufficient to quantitatively measure a photo-induced voltage or photo-induced current. The measurements described will therefore be limited to the range 300-400 nm in the ultraviolet which corresponds to the bandgap of PZT (3.3 eV, 370 nm). The photovoltage is determined in an open circuit state, while the photocurrent is obtained in the short circuit state. Power of diode and lamp is measured using power detector Newport 919P-010-16. Both UV sources were placed at the same position with a distance of 1-1.5cm from the power meter, similar to the sample-UV source position, to extract the power and divided by the illuminated area to obtain the effective fluence during measurements. In Figure 2.13 b & c, the power of the diode is plotted as a function of its current intensity, and the fluence of the Xe lamp is plotted for wavelength ranging from 300 to 400nm. In order to pole the sample before each measurement, TF Analyzer 1000 AixACCT (ferroelectric tester) was connected to the sample as shown in Figure 2.13 a.

The spectrometer setup used for the wavelength-dependent photocurrent measurements presented in chapter 3 belongs to the Photonics group of Francois Julien and Maria Tchernycheva at C2N. Note that the UV fluence achieved by the Xe lamp is much lower than the one from the LED.

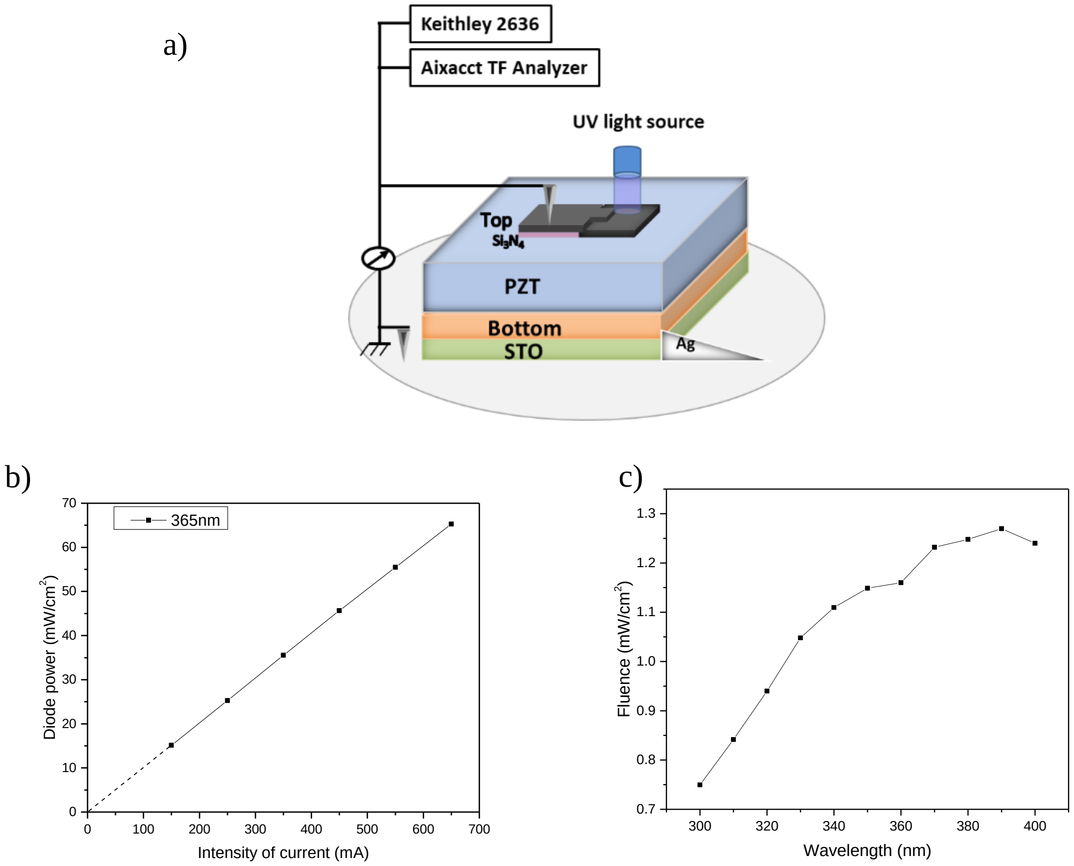

Figure 2.13. a) Setup for photovoltaic measurements where the sample is under UV illumination and connected to Keithley 2636 and Aixacct TF Analyzer 1000. b) Power of diode emitting at 365nm wavelength as a function of its driving current. c) Fluence of Xe lamp at the end of the fiber as a function of wavelength ranging from 300 to 400nm.

Chapter-3

Ferroelectric and photovoltaic characterization of PZT capacitors

Contents

This chapter covers the general characterization of PZT ferroelectric thin film, specifically on a Pt/PZT/SRO//STO capacitor device (sample number 3020). First, the surface morphology and crystal structure were studied using atomic force microscopy and x-ray diffraction. Then the ferroelectric and photovoltaic properties under two UV sources were analyzed.

3.1 Surface and structural characterization

The surface and structural characterization of PZT on SRO/STO substrate show a good quality of thin film with smooth surface and good crystallinity. AFM topography image is presented in Figure 3.1(a) and evidences a flat surface of the PZT film with a roughness of 0.5 nm rms. An XRD θ-2θ curve around the (002) PZT Bragg peak is presented in Figure 3.1(b), showing also both SRO and STO (002) peaks. The out-of-plane c lattice parameter of SRO is 0.395nm and the bottom electrode thickness was found to be 37nm from the analysis of the thickness fringes. The out-of-plane c lattice parameter of PZT is 0.413nm, which is consistent with its tetragonal structure for the $Pb(Zr_{0.2},Ti_{0.8})O_3$ composition.

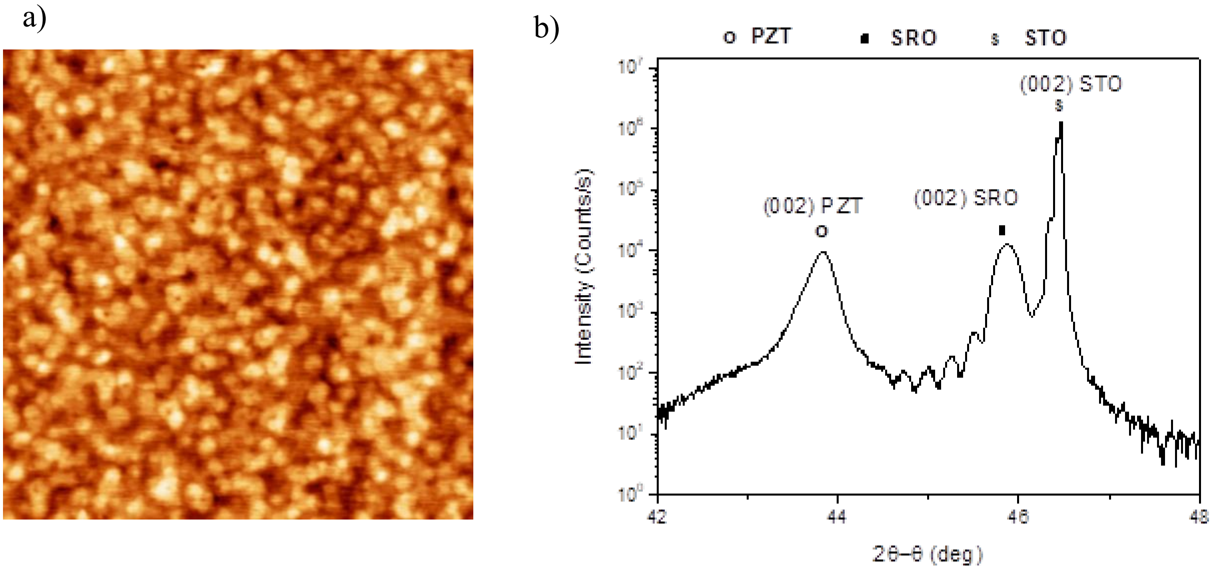

Figure 3.1. (a) AFM topography image (size 2x2 μm²), (b) θ-2θ XRD curve of PZT/SRO/STO.

3.2 Ferroelectric characterization

Ferroelectric measurements were performed by measuring dynamic P–V hysteresis loop using a TFAnalyzer1000 (aix-ACCT systems) at 1 kHz. The voltages were applied to the top electrode (Pt) with the bottom electrode (SRO) grounded and all the measurements were performed at room temperature.

3.2.1 Ferroelectric hysteresis loop

A dynamic ferroelectric polarization loop and its corresponding current loop are measured at 1 kHz for a 100 ×100 μm^2 capacitor device, as shown in Figure 3.2. It is a symmetrical polarization loop with remanent polarization of ±73µC/cm^2. The measured remanent values are consistent with the remanent values existed in the literature in the range of 50-100 µC/cm^2 for 20/80 composition of PZT [4]. The current hysteresis loop presents two sharp peaks at the coercive voltage with values of -2.7V and +2.8V.

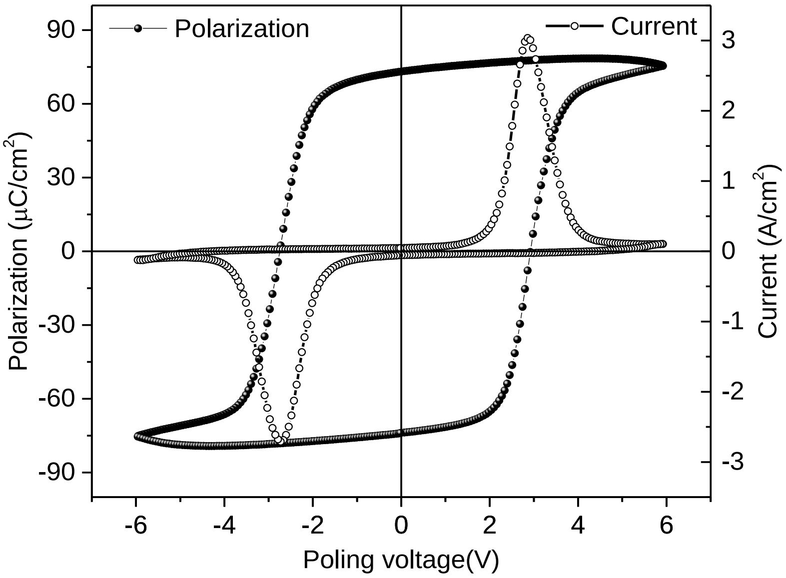

Figure 3.2. Ferroelectric hysteresis and corresponding current density hysteresis loop for PZT thin film.

3.2.2 PUND loop

Figure 3.3 depicts the ferroelectric polarization loop and its corresponding current loop, measured following the PUND (Positive Up Negative Down) method in order to remove the contribution from leakage currents. This contribution was rather small as seen on the classical hysteresis loop (shown in Figure 3.2). The PUND ferroelectric loop exhibits remanent polarizations of ±70µC/cm^2 and coercive voltage values of -2.7V and +3.3V. There is a 0.7V shift in the coercive fields towards the right (positive side) indicating the presence of an internal electric field pointing in up direction.

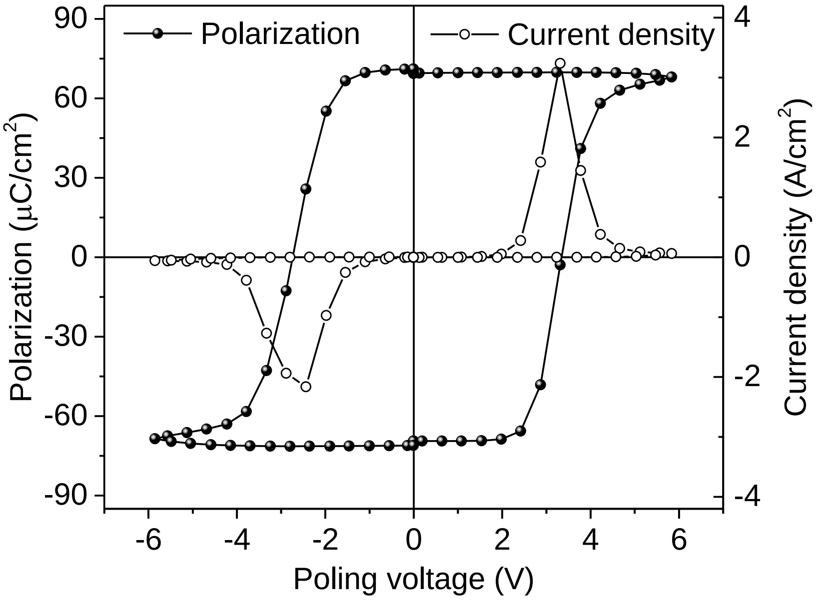

Figure 3.3. PUND polarization hysteresis and corresponding current density hysteresis loop for PZT thin film at 1kHz.

Retention of polarization without light illumination

Retention of polarization in ferroelectric-based devices is a crucial property to attain. In order to study the retention of the written polarization before shining light on the sample, a voltage protocol is followed during the measurement. In this protocol, the sample is first poled by a voltage waveform (see Figure 3.4 a (1)). After 100 seconds of waiting time in open circuit condition, the sample is again poled (see Figure 3.4 a (2)). After short circuit current measurement in dark for 100 seconds, the sample is poled again. All three waveforms allow to define the polarization state of the sample (called initial polarization) either up or down (after -6V or +6V last pulse) and the last two waveforms give access to the retention of polarization (called the final polarization) 100 seconds after poling, either in open-circuit (waveform (2)) or short-circuit condition (waveform (3)).

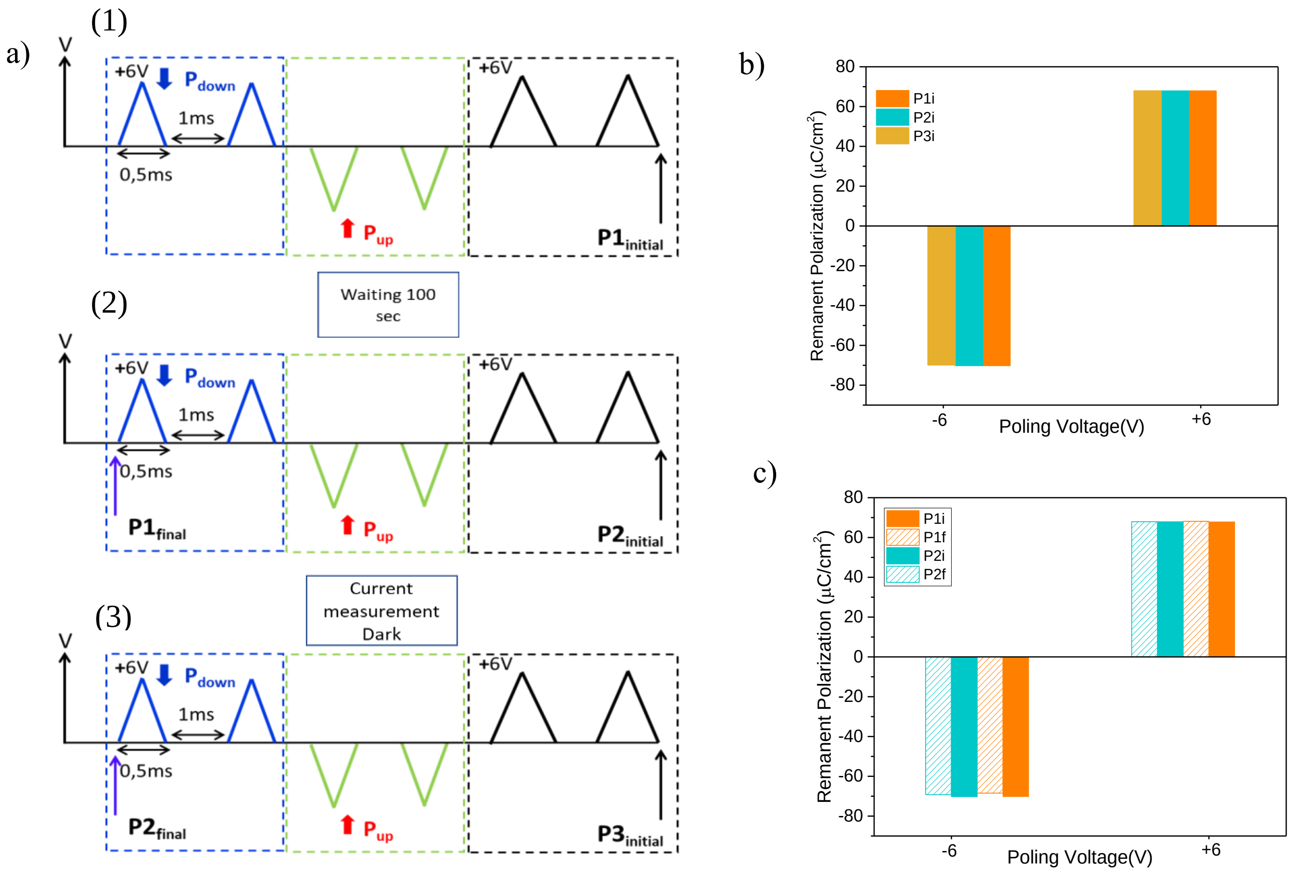

Figure 3.4. a) Voltage waveform used to pole the sample (1) before waiting time of 100 sec in open circuit condition, (2) after 100 sec waiting and before short circuit current measurement in dark condition and (3) after short circuit current measurement in dark condition. b) Initial remanent polarization in two poling states where initial polarization is extracted from the voltage waveform (1), (2), and (3) as $P1_{initial}$ (P1i), $P2_{initial}$ (P2i), and $P3_{initial}$ (P3i). c) Remanent polarization of initial and final polarization in two poling states in open and short circuit condition without illumination.

Remanent polarization values extracted from this protocol are mentioned below:

$P1_{initial}$- First Initial remanent polarization (P1i) value obtained from the first voltage waveform (1).

$P1_{final}$- First final remanent polarization (P1f) value, after 100 sec waiting time in open circuit condition, obtained from second voltage waveform (2).

$P2_{initial}$- Second initial remanent polarization (P2i) value obtained from the waveform of poling (2) just before current measurement in short circuit condition.

$P2_{final}$- Second final remanent polarization (P2f) value after 100 sec waiting time in short circuit condition (during I(t) measurement without UV illumination) obtained from poling (3).

$P3_{initial}$- Third initial remanent polarization (P3i) value obtained from poling 3.

The following plots in Figure 3.4 (b) represent the three initial polarization values (P1i, P2i, and P3i) for ±6 V polarization state (poling voltage). The plotted histogram clearly shows that the same poling procedure gives quite the same initial polarization value, as expected. Figure 3.4 (c) depicts the final polarization values (P1f and P2f) with respect to initial polarization values, which are more or less similar. Thus, the PZT thin film shows good retention of polarization in both polarization states, in both open circuit and short circuit conditions, in dark.

3.2.3 Capacitance-voltage (C-V) measurement

C-V characteristic while sweeping the DC voltage between -3V and +3V, under an AC voltage of 30 mV at 1kHz is presented in Figure 3.5. It shows a butterfly loop, with a maximum of capacitance at the ferroelectric switching voltage, a typical characteristic of ferroelectrics. Relative permittivity can be extracted using capacitance values and plotted against DC voltage. As it was first shown by polarization measurements above, this measurement also reveals the typical sharp ferroelectric switching of the PZT layer for the 20/80 Zr/Ti ratio. Dielectric constant is maximum at the coercive voltage and shows a value of ≈ 200 which is consistent for the 20/80 composition and lower than dielectric constant for MPB composition [95]. Note that the apparent coercive voltages are here smaller than the ones in the polarization loop because the voltage is swept at a much lower frequency.

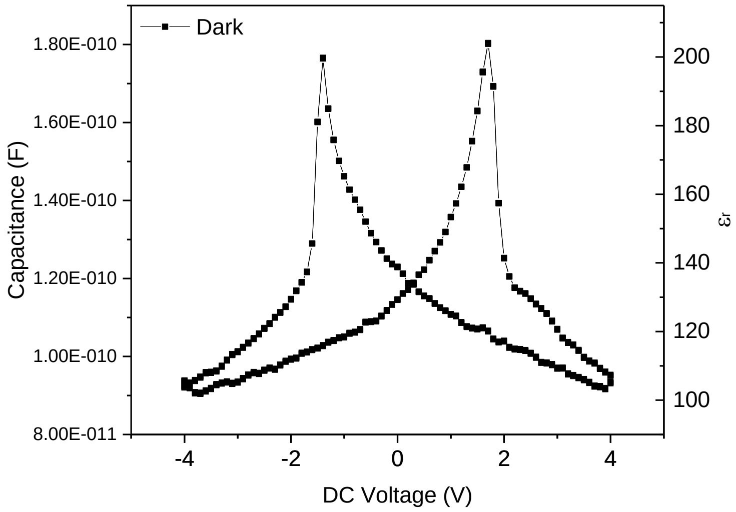

Figure 3.5. Capacitance-voltage characteristic (on the left axis) for a PZT thin film and its corresponding dielectric constant (on the right axis) measured as a function of DC voltage at 1kHz in dark.

3.3 General Photovoltaic properties

Photovoltaic measurements were performed using Keithley 2636 under UV illumination at 365 nm wavelength (except for the last part reporting the wavelength study which was performed using the Xe lamp), corresponding to photon energy above the bandgap of PZT. The samples were illuminated from the top with a diode of 365 nm wavelength. The incident power of the diode on the capacitor device was measured to be 35.5 mW cm^{-2}, of which 45% is absorbed by the Pt top electrode.

3.3.1 Current-voltage measurements

Figure 3.6 depicts the photovoltaic properties of the PZT capacitor in the dark and under UV illumination at 365nm. The photocurrent was measured in the UP (P_{up}) and DOWN (P_{down}) states, corresponding to -6V and +6V poling voltage, respectively. The short-circuit photocurrent density (Jsc) for the Pup polarization state is positive, while the Jsc for the P_{down} polarization state is negative. This is consistent with the expected sign of photocurrent if we consider the depolarizing field as the main driving force. For P_{up} state, for example, the depolarizing field would point towards the SRO bottom electrode. Under illumination, photo-generated electron-hole pairs would then be separated by this electric field, resulting in a positive photocurrent in short-circuit conditions. By changing the polarization direction, the photocurrent changes sign, as previously reported in many studies. Naturally, for one given polarization state, the Jsc and the open-circuit voltage (Voc) have opposite signs, since in an open-circuit condition the photo-generated charges accumulate at each interface, tending to compensate the depolarizing field. However, this observed switchability of Jsc and Voc could also come from the bulk PV effect. Note that Jsc and Voc are slightly higher in absolute value for the P_{down} state (-51.6μA/cm^2 and 0.53V instead of 38.2μA/cm^2 and -0.4V for the P_{up} state). The switchability value of Jsc is obtained as 87% using equation 1.13 (chapter 1). Since both remanent P_{up} and P_{down} polarization values are similar, the measured differences for Jsc and Voc in both polarization states cannot be fully explained by considering only the switchable remanent polarization which is measured in these PZT thin films. Note that the ferroelectric loop (Figure 3.3) presents an imprint towards the positive voltage, indicating some internal electric field pointing up which could favor higher Jsc and Voc in the P down state.

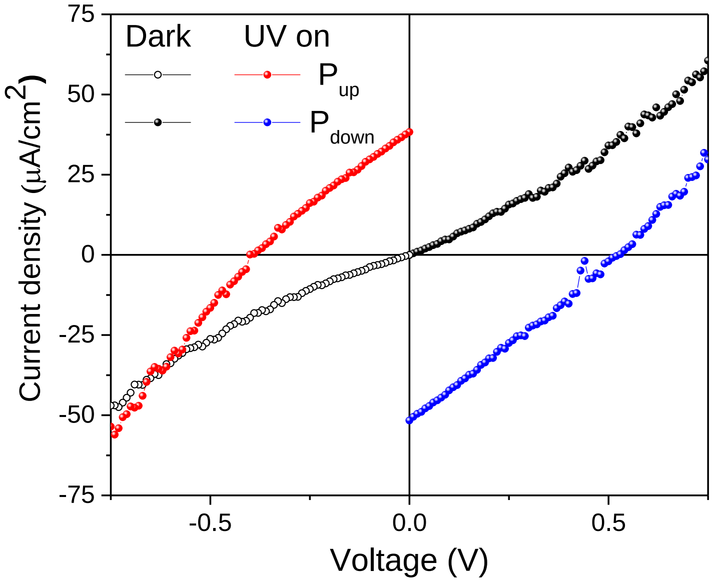

Figure 3.6. Current density Vs voltage measurement both in the dark and under UV illumination for UP and DOWN poling states.

3.3.2 Photocurrent and photovoltage time dependence

The short circuit current density Jsc over time ($J(t)_{v=o}$) is measured as shown in Figure 3.7 (a).

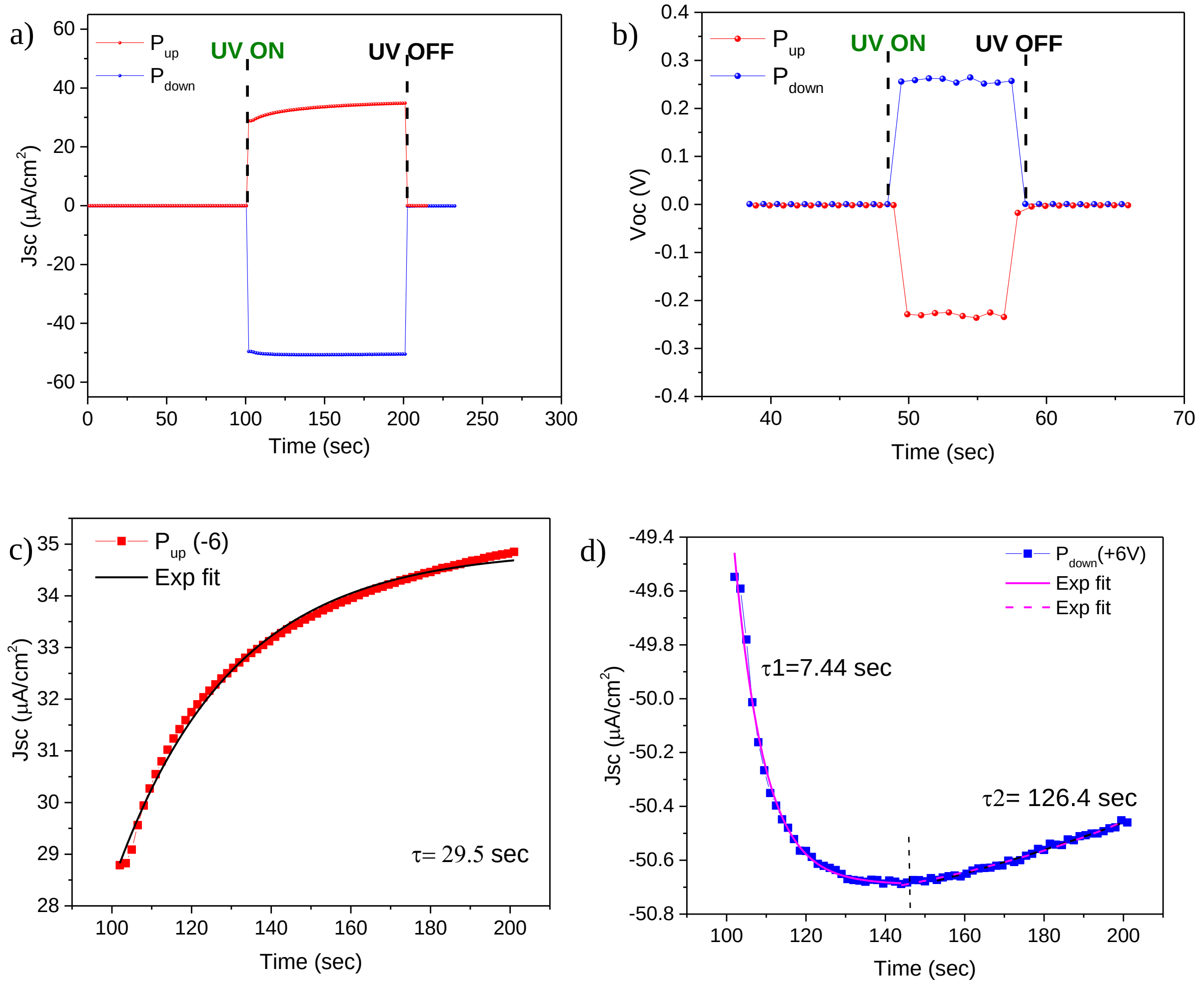

Figure 3.7. a) short circuit current density, b) open-circuit voltage as a function of time under UV OFF and ON condition, c) exponential fit of Jsc curve (a) under UV ON in P_{up} state, and d) exponential fit of Jsc curve (a) under UV ON in P_{down} state.

The photocurrent is measured after +6V and -6V poling to reach P_{down} and P_{up} state. Initially, for 100 sec, the current is measured in a short circuit condition to allow the relaxation of charges to attain a steady flow. After 100 sec, the sample is illuminated with 365nm wavelength UV (UV ON) with a diode driving current of 350mA corresponding to a power of 35.5 mW/cm^2. The values of Jsc are, when the UV light is just turned on, 28.7µA/cm^2 and -49.5µA/cm^2 for the P_{up} and P_{down} polarization states. Before turning off UV, Jsc values are 34.8µA/cm^2 and -50.4µA/cm^2 for the P_{up} and P_{down} polarization state. Clearly, the P_{up} state shows more transient behavior than P_{down} state. However, the final polarization (Pf) values after I(t) measurement does not indicate any change in polarization under UV light. Thus, the photocurrent time dependence does not seem to be related to a change in polarization state. The transient J(t) curves in Figure 3.7 (a) are fitted exponentially in P_{up} and P_{down} state (see Figure 3.7 c-d). The time constant is extracted using equation 3.1 in P_{up} polarization state as

29.5 sec. In Figure 3.7 (d), Jsc curve in P_{down} shows exponential increase in the beginning with time constant τ1= 7.4 sec and then decreases with time constant τ2= 126.4 sec. In the V-t measurement, Voc values in P_{up} and P_{down} polarization states are -0.23 V and 0.25 V, rather showing steady behavior over time in Figure 3.7(b). The time dependence of the photocurrent will be further investigated in the part 3.3.4 of this chapter and for different wavelengths.

$$f(t) \propto exp\,(-t/\tau) \tag{3.1}$$

3.3.3 Fluence dependence

The next measurement made is a measure of J(V) in dark and under illumination at 365 nm with different incident UV light intensities for the same PZT thin film. The measurements are made after poling at +6V (P_{down}) and -6V (P_{up}) polarization states and shown in Figure 3.8. As observed in the last two parts, for up polarization state, Jsc (short circuit current density at V=0V) is measured positive and Voc (open circuit voltage at J=0) is negative whereas for down polarization state Jsc is negative and Voc is positive. Clearly, Jsc is increasing with increasing intensity of UV illumination at 365nm wavelength. The Voc is following the same trend with the increment of UV intensity but saturates at high intensities. It is well known that Voc in ferroelectrics usually increases with the increase of incident UV intensity and then saturates to a constant value at sufficiently high light intensities when the photoconductivity becomes dominant over the dark conductivity [96]. The set of values of Jsc and Voc is listed in table 3.1.

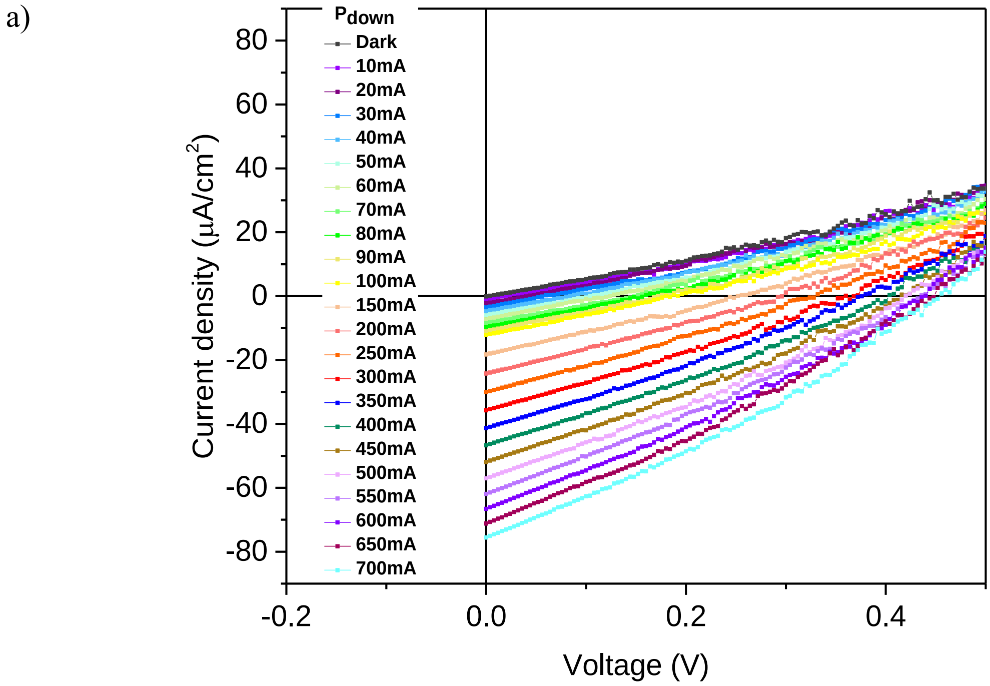

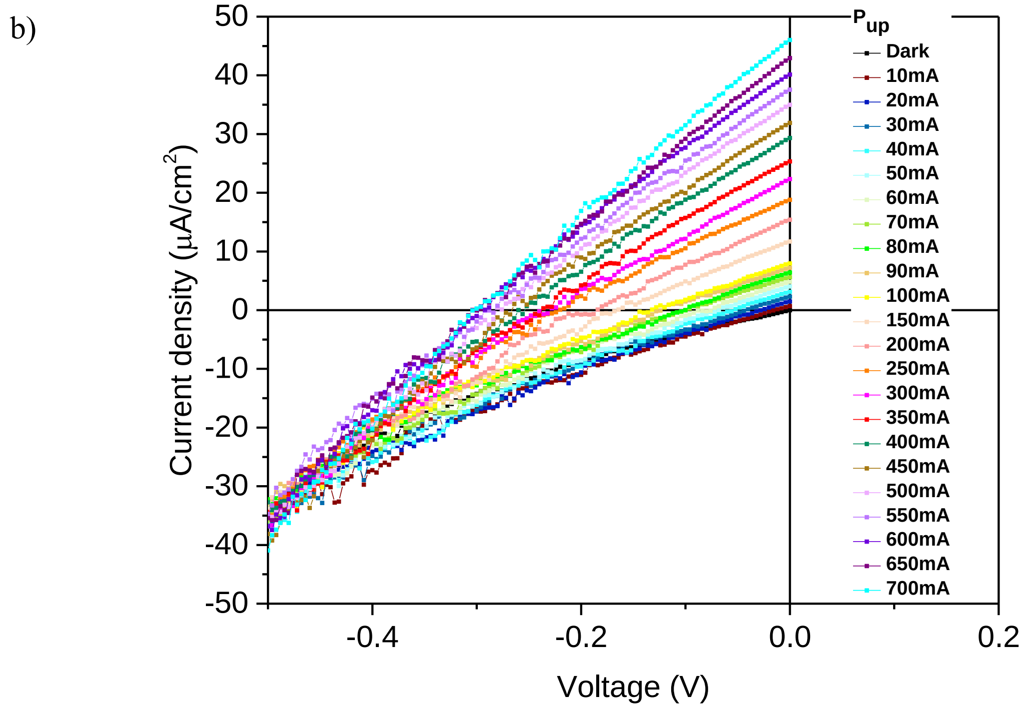

Figure 3.8. J-V curves under the different intensities (diode driving current) of UV light at 365nm wavelength in (a) polarization down state and (b) polarization up state.

Intensity of UV at 365nm (driving current values in mA)	**Jsc(μA/cm^2) P$_{down}$**	**Voc (V) P$_{down}$**	**Jsc (μA/cm^2) P$_{up}$**	**Voc (V) P$_{up}$**	**Fluence (mW/cm^2)**
10	-1	0.016	0.67	-0.01	1.3
20	-2.2	0.041	1.4	-0.02	2.21
30	-3.5	0.056	2.2	-0.04	3.05
40	-4.7	0.084	3.1	-0.05	3.98
50	-5.9	0.1	4	-0.06	4.97
60	-7.2	0.12	4.8	-0.07	5.97
70	-8.4	0.14	5.6	-0.099	7.07
80	-9.7	0.15	6.3	-0.099	8.34
90	-10.9	0.17	7.1	-0.12	9.4
100	-12.1	0.19	7.9	-0.13	10.2
150	-18.2	0.25	11.6	-0.16	13.2
200	-24.2	0.29	15.3	-0.18	20.6
250	-30	0.33	18.7	-0.22	25.2
300	-35.7	0.35	22.3	-0.23	30.9
350	-41.3	0.37	25.3	-0.24	35.5
400	-46.6	0.4	29.3	-0.25	40.9

450	-51.9	0.41	31.8	-0.26	45.1
500	-57	0.42	34.9	-0.28	50.4
550	-61.9	0.43	37.5	-0.28	54.8
600	-66.6	0.44	40.1	-0.29	60.8
650	-71.2	0.45	42.9	-0.3	65.4
700	-75.5	0.45	45.9	-0.3	71.6

Table 3.1 List of the values of Jsc and Voc for different UV intensities at 365nm wavelength for polarization down and up state.

Based on the measurements above Jsc dependence on the fluence of UV light is plotted in Figure 3.9 a) for polarization up and down state, which shows that Jsc increases linearly with the fluence, as expected. Voc dependence on the fluence is also plotted in Figure 3.9 b) for both states and shows the increase of Voc at low light intensity, followed by a saturation at higher intensity.

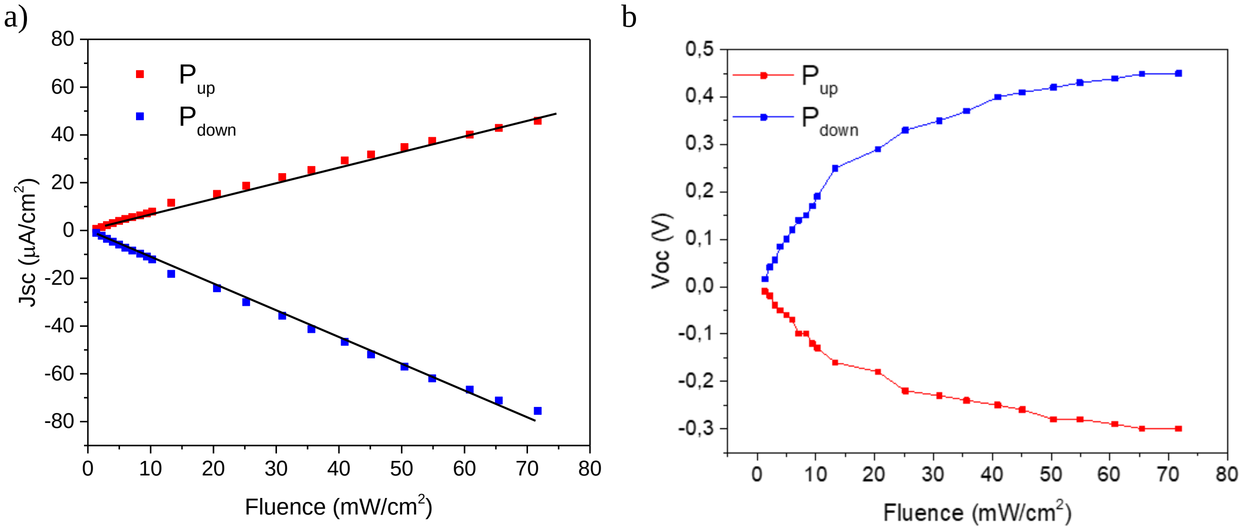

Figure 3.9. a) Jsc and b) Voc plotted as a function of fluence of UV light for up and down polarization state.

The next plot is conductance as a function of fluence of UV light as shown in Figure 3.10 (a). The conductance values are obtained using I-V measurements. Since the I-V curves are not perfectly linear up to Voc values, the slope is extracted from the linear part of I-V at low voltages. One example of the extraction of conductance is shown in Figure 3.10 (b), where I(V) is measured at 350mA light intensity of 365nm wavelength after +6V poling and fitted linearly to obtain the slope. This slope is conductance and is 10 nS at 35.5 mW/cm^2 for the P_{down} state. Conductance for different light intensities was extracted from the slope of all the I-V curves in Figure 3.8 and plotted in Figure 3.10(a). The photoconductivity values are showing linear behavior with light intensity, as expected [2].

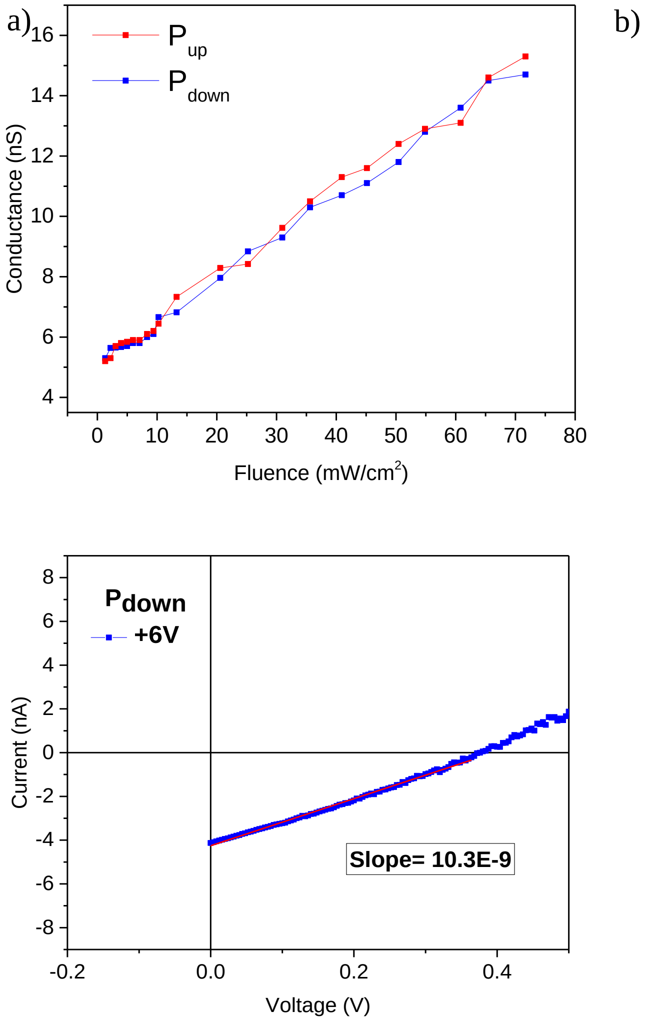

Figure 3.10 (a) Conductance plotted as a function of fluence of UV light for up and down polarization state. b) Linear fit of I-V curve at small voltages for +6V pre-polarized state under 365nm wavelength at 35.5 mW/cm^2.

The open circuit voltage (Voc) has also been measured as a function of time for the two polarization states after a pre polarization of +6V and -6V and it can be seen in Figure 3.11. The diode is repeatedly switched on and off. The Voc is increasing with increasing intensity of UV light (indicating by arrow) ranging from 10mA to 600mA driving current and tends to saturate at high intensity. This measurement is in agreement with previous J-V measurements. A list of Voc values obtained from this measurement can be seen in table 3.2.

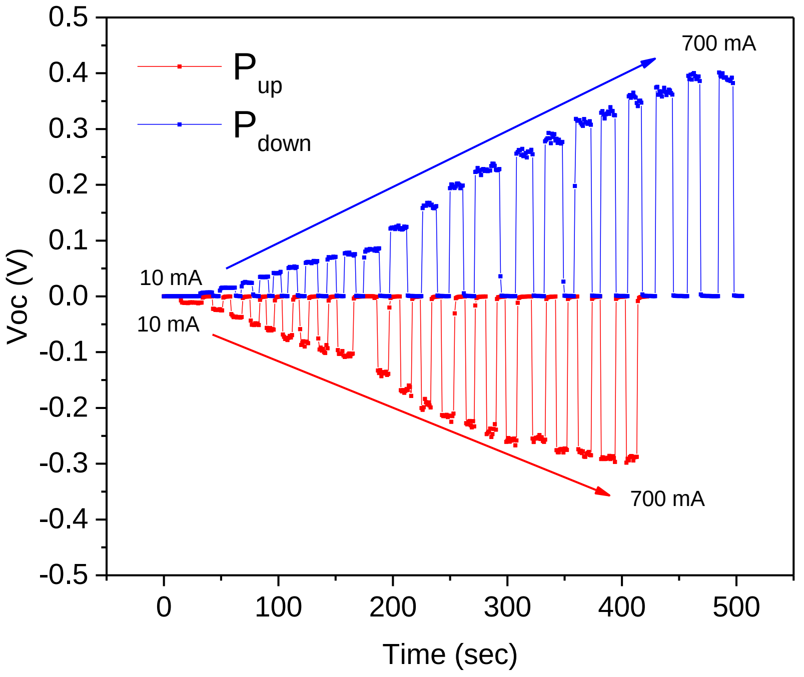

Figure 3.11. Open circuit voltage as a function of time for different UV intensities (at 365nm wavelength) in up and down polarization state.

Intensity of UV at 365nm (driving current values in mA)	Voc (V) P_{down}	Voc (V) P_{up}
10	0.007	-0.011
20	0.015	-0.024
30	0.024	-0.035
40	0.034	-0.04
50	0.042	-0.05
60	0.053	-0.058
70	0.063	-0.074
80	0.069	-0.083
90	0.075	-0.095
100	0.084	-0.11
150	0.12	-0.13

200	0.16	-0.17
250	0.19	-0.19
300	0.22	-0.21
350	0.24	-0.22
400	0.28	-0.24
450	0.31	-0.25
500	0.32	-0.25
550	0.35	-0.27
600	0.37	-0.28
650	0.39	-0.29
700	0.4	-0.29

Table 3.2 List of values of Voc for different UV intensities in up and down polarization state.

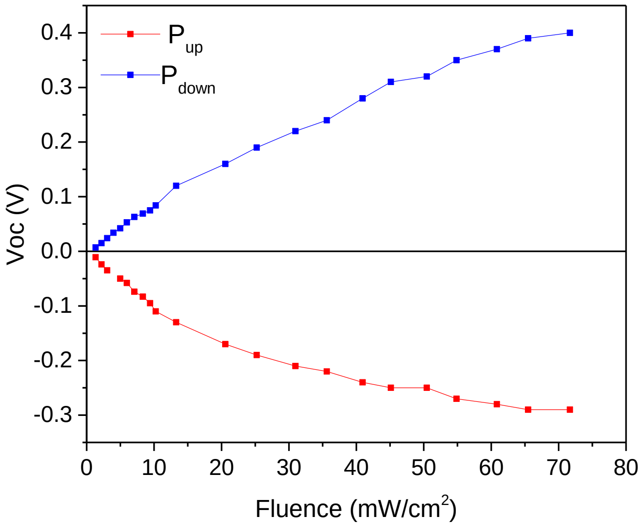

Figure 3.12. Voc is plotted against the UV fluence (at 365nm wavelength).

Then the extracted Voc values are plotted as a function of fluence in Figure 3.12. The increment in Voc is nonlinear in both polarization states. The Voc values are a bit higher in the down polarization state as observed in the I-V part.

3.3.4 Wavelength dependence

a) Optical absorption of PZT

The absorption profile (α) and penetration depth (d) of PZT are shown in Figure 3.13 (a-b). From the onset of absorption, a gap of 3.3 eV (375 nm wavelength) can be estimated. At 375nm wavelength, absorption coefficient is α_{PZT}= 82862 cm^{-1} and penetration depth is comparable to the film thickness (120nm) .

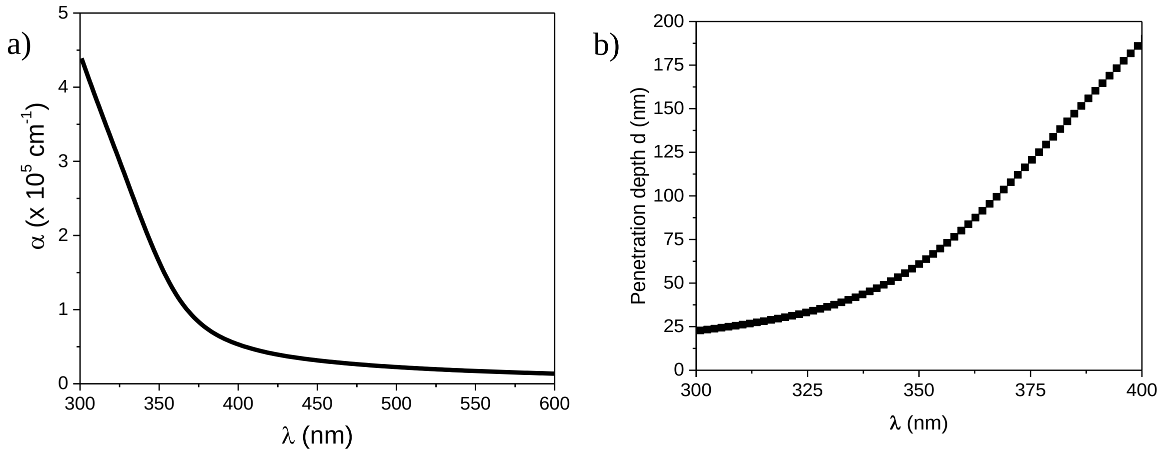

Figure 3.13 a) Absorption coefficient and b) penetration depth in PZT as a function of wavelength.

b) Wavelength dependence in up and down Polarization states

In the next parts, the Pt/PZT/SRO device is illuminated by the Xenon lamp light coupled with a Jobin Yvon Triax 180 spectrometer to tune the wavelength in the range of 300-400nm.

In Figure 3.14 (a), photocurrent is measured as a function of time while sweeping wavelength from 300nm to 400nm for different pre-polarization states (poling at +6V and -6V). After poling, Isc is measured in short circuit in dark for 100 sec then the UV exposure starts at t=0sec from 300nm wavelength. While the photocurrent is continuously measured, the light wavelength is changed every 10sec with a step of 10nm till 400nm. Then the photocurrent Isc is normalized by the area of the device to get photocurrent density and plotted as a function of wavelength (See Figure 3.14 (b)). The short circuit current is negative for the positive polarization state (+6V) and positive for the negative polarization state (-6V) under the UV light, as expected. Jsc increases when the photon energy increases and the onset of photocurrent at 375 nm wavelength is in agreement with the absorption measurements and

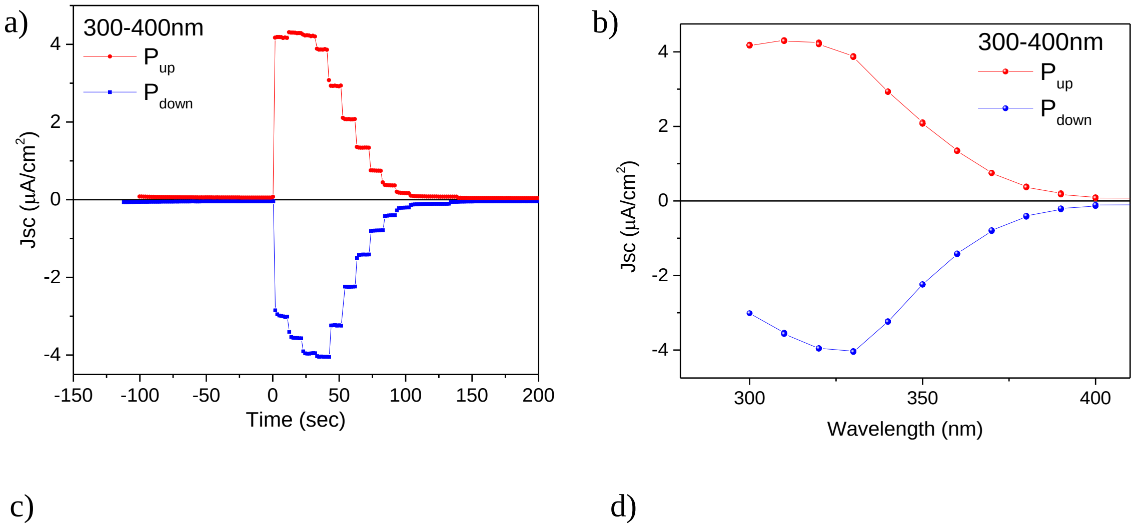

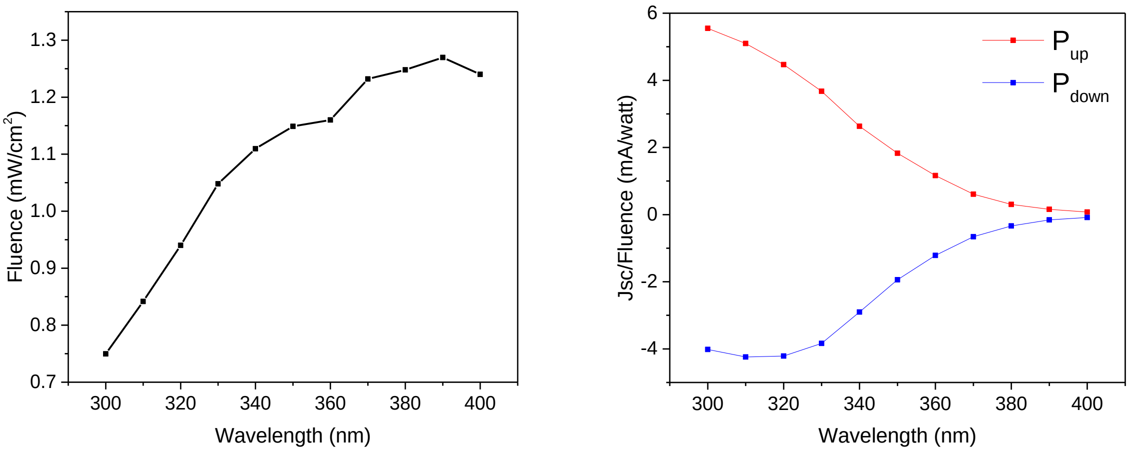

Figure 3.14. a) Photocurrent measurement over time for a wavelength sweep between 300nm and 400nm in both polarization states, b) Jsc Vs wavelength, c) lamp fluence as a function of wavelength, d) Jsc/fluence as a function of varied wavelength for the Pt/PZT/SRO device, consistent with a PZT band gap of 3.3 eV (375 nm wavelength).

a PZT band gap energy of 3.3 eV. The intensity of the Xe lamp decreases with the wavelength (as shown in Figure 3.14 (c)), so to take into account this, the photocurrent density has been divided by the fluence and once again plotted as a function of wavelength in Figure 3.14 (d). At constant fluence, the photocurrent increases progressively when the photon energy increases even if the photo carriers are more and more generated at the top of the film (decrease of the penetration depth). The too low fluence of the Xe lamp for photon wavelength below 300 nm prevented from studying photocurrent at higher photon energy.

c) Time and wavelength dependence in up and down Polarization states

The measurement of short circuit current Jsc with time (I(t) V=0) for different wavelengths is shown in Figure 3.15. After 100 sec in dark, the sample is illuminated with UV light for different fixed wavelengths from 300nm to 370nm. Note that in order to pole the sample in up (-6 V) and down (+6 V) polarization state, poling was performed before each I(t) measurement. It should be observed that the asymmetry in Jsc absolute values in two polarization states shows the same behavior shown by the measurements under diode where Jsc in P_{down} state is higher than P_{up} state. For ± 6V polarization states, Jsc looks rather steady over time in Figure 3.15 (a-b). Figure 3.15 (c) shows Jsc as a function of different wavelengths and Figure 3.15 (d) Jsc divided by the fluence as a function of wavelength. The wavelength dependence is consistent with the results already shown in Figure 3.14 (d).

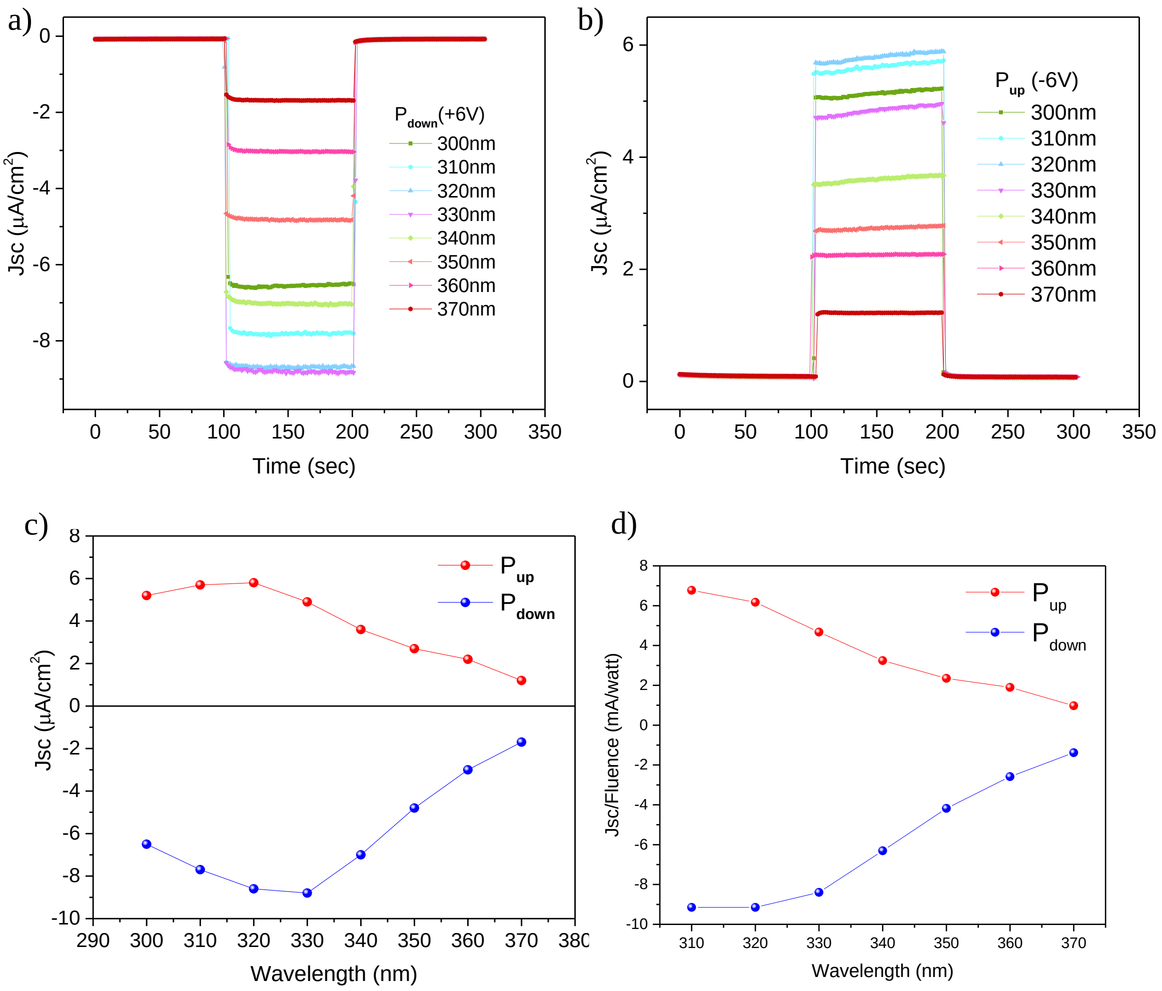

Figure 3.15. Short circuit current is plotted against time for different wavelengths ranging from 300 to 370 nm in a) polarization down state after +6V poling, b) polarization up state after -6V poling. Plots of c) Jsc and d) Jsc/fluence as a function of wavelength.

d) Time and wavelength dependence in disordered Polarization states

Repetition test

Before investigating the wavelength dependence of photocurrent in disordered polarization states, a repetition test is conducted to determine if the same poling procedure for intermediate polarization states results in the same photocurrent value. In that purpose, a measurement of photocurrent at 365nm wavelength has been performed 4 times on an intermediate state (4 times poling at 2.61 V) (See in Figure 3.16). In this test, the sample is pre-polarized each time before I(t) measurement, and the same poling pulse is applied after the I(t) to extract the polarization value. The final remanent polarization values after each I(t) measurement are listed in the table 3.3 as Pfinal (Pf). The evolution of photocurrent over time is fitted with double decay exponential and the time constant values are also listed in the table 3.3. First, the time constants values are similar for measurements 1, 3 and 4 (the difference found for the second measurement may be related to the difficulty to fit the time dependent Isc by two decaying exponentials).

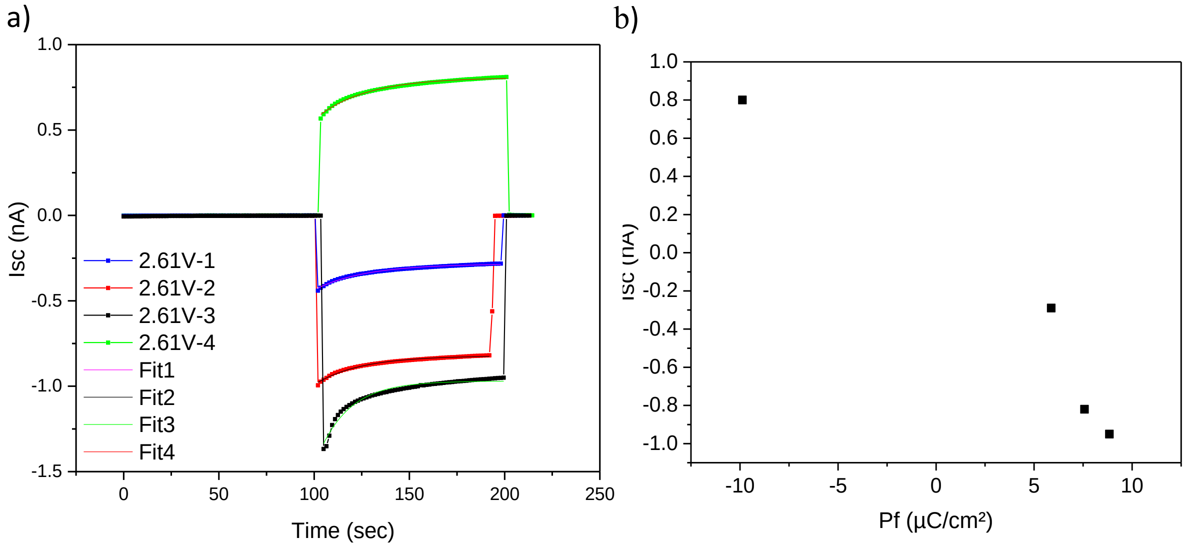

Figure 3.16. Repetitive photocurrent measurement at 2.61 V poling state under 365nm wavelength (350mA diode driving current). a) Isc as function of time (the time constants are listed for the 4 measurements extracted from the fitting in table 3.3). b) Final Isc value as function of final remanent polarization value.

The Pf values are small, between 9 and -10 µC/cm², which is consistent with the poling in an intermediate polarization state (close to P~0). The final Isc values vary typically between -1 nA and 0.8 nA. The Isc values are clearly related to the Pf values, as shown in Figure 3.16 b). So, for the next study of wavelength dependence of photocurrent, one needs to keep in mind that poling in intermediate states does not end up exactly in the same polarization state, which gives different photocurrent values, but the time evolution remains similar.

Poling Voltage	Isc (nA)	Pf (µC/cm^2)	Time constant (sec)	
			τ1	τ2
2.61V-1	-0.29	5.9	55.6	7.4
2.61V-2	-0.82	7.6	24.3	
2.61V-3	-0.95	8.9	54.9	5.9
2.61V-4	0.8	-9.9	51.6	6.8

Table 3.3. List of final Isc, remanent polarization values (Pf) taken after photocurrent measurement and time constant for four measurements performed in an intermediate polarization state after poling at 2.61 V.

Photocurrent measurements

Photocurrent measurements at different wavelengths (between 300nm and 390 nm) were performed for two intermediate pre-polarization states close to the polarization switching: after a partial switching at -2.2 V from the P_{down} state (defined as P_{up} (-2.2 V)) and after a partial switching at +2.6 V from th P_{up} state (defined as P_{down} (+2.6 V)). The results are shown in Figure 3.17 (a,b). The device is poled before and after each photocurrent measurement. In Figure 3.17 (a, b), the magnitude of the photocurrent changes with the wavelength. This is caused by the expected wavelength dependence (as already shown for up and down polarization states), plus the fact that for each Isc measurement at one wavelength the polarization state can be a bit different (see last repetition test). Note that the Isc curve for P_{down} (after 2.6V poling) at 340nm was measured three times (shades of green): different Isc values are obtained and are well related to the difference in remanent polarization values (Pf) (extracted after each I(t) measurement and listed in table 3.4).

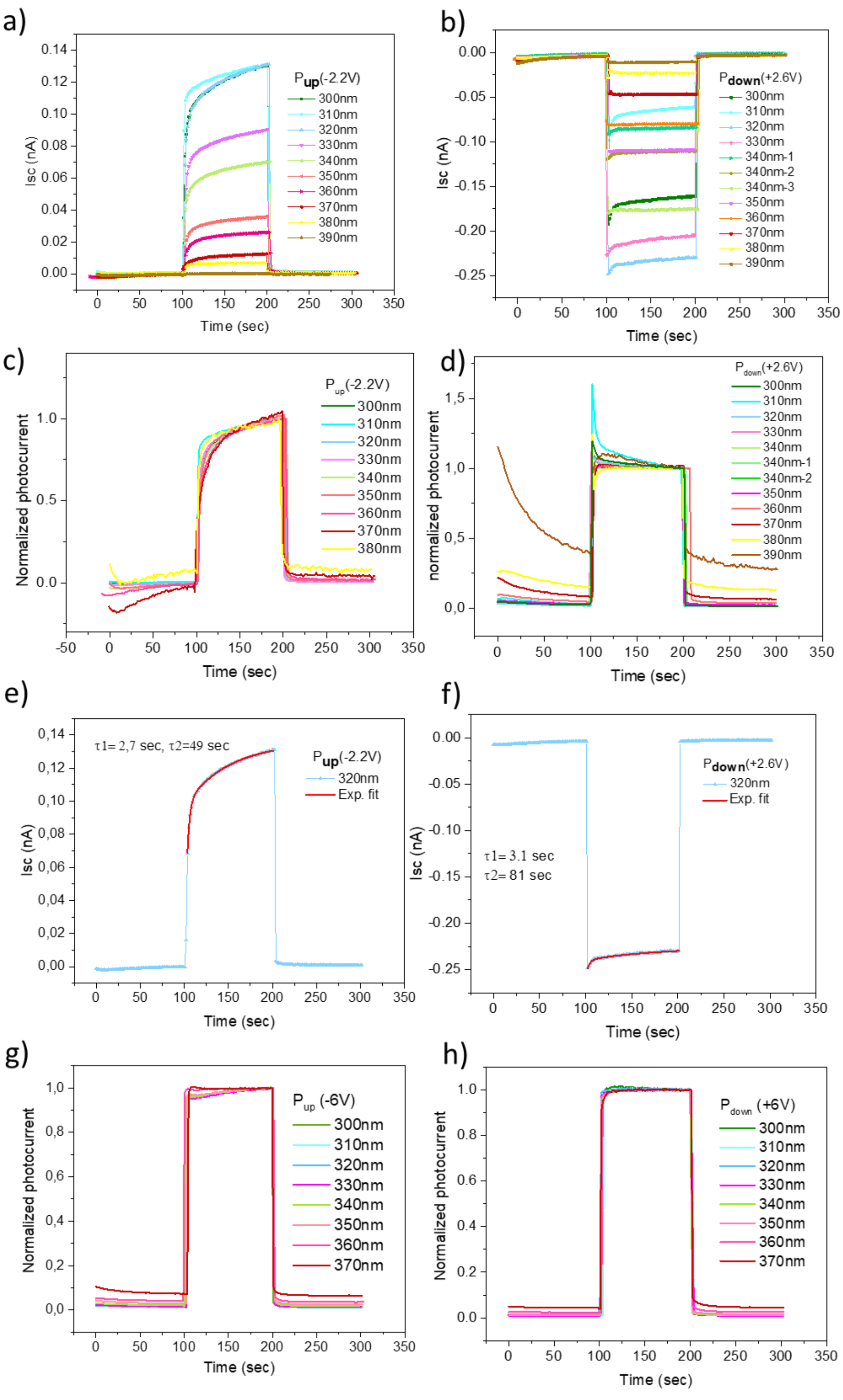

Figure 3.17. Wavelength dependence over time at two intermediate poling states a) -2.2V (P_{up}) and b) +2.6V (P_{down}). Normalized photocurrent as function of time for varied wavelength for c) -2.2V (P_{up}) and d) +2.6V (P_{down}) and corresponding fitting for e) -2.2V (P_{up}) and f) +2.6V (P_{down}) at 320 nm wavelength with the two-time constants extracted. Normalized photocurrent as function of time for varied wavelength for g) up polarization state (-6V) and h) down polarization state (+6V), calculated from the photocurrent data in Figure 3.15 (a, b).

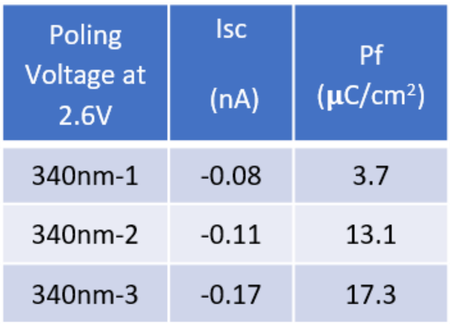

Poling Voltage at 2.6V	Isc (nA)	Pf ($\mu C/cm^2$)
340nm-1	-0.08	3.7
340nm-2	-0.11	13.1
340nm-3	-0.17	17.3

Table 3.4 List of final remanent polarization values (Pf) and Isc after photocurrent measurement at 340 nm wavelength (in the intermediate polarization state after poling at 2.61 V).

Discussion about the transient response

The photocurrent has been normalized by the final value and is shown for different wavelengths in P_{up} (after -2.2V poling) and P_{down} (after 2.6V poling) in Figure 3.17 (c-d). For P_{up} state in Figure 3.17 (a, c), it can be seen that the transient behavior is relatively independent of change in the wavelength. In P_{down} state in Figure 3.17 (b, d), photocurrent for wavelength from 300 nm to 340 nm shows a ‘‘peaked’’ transient behavior whereas photocurrent for wavelength ≥ 350 nm shows a steadier behavior. For both intermediate states (at very low polarization value), the photocurrent shows a more pronounced transient behavior than for up and down polarization states (normalized photocurrents are shown in Figure 3.17 (g, h) from previous data of Figure 3.15 (a, b)). The mechanisms which govern the time evolution of the photocurrent remain not clear and difficult to estimate. We present and discuss in the following several possible effects that could contribute to the transient response of the device.

“RC time constant”: The transient feature of photocurrent could be related to the typical RC time constant of the device. Under UV illumination by Xe lamp (fluence ~ 1mW/cm²), the conductance is typically 5 nS (figure 3.10 a)) giving R = 200 MΩ. With a capacitance of 12 nF, a RC time constant of 2,4 seconds can be estimated. Time-dependent photocurrent curves can be fitted by a double exponential with two time constants. The first one is typically below 10 s (table 3.3) and equals ~ 3 s for these last measurements (figure 3.17 (e, f)). So, this first “fast” transient behavior could be indeed related to the charging of the capacitor device with RC time constant. However, the second “slower” response has a different origin and seems to be related to the polarization state and the wavelength.

Partial screening of depolarizing field under illumination: When shining light on the device, photogenerated carriers will tend to screen the depolarizing field and thus increase the ferroelectric polarization, a mechanism that was evidenced at ultrafast (ns) timescale [30]. Under continuous illumination, trapping of charges can be observed at a longer timescale, that would thus give a decrease of the depolarizing field-driven photocurrent (in absolute value). However, this is not what is observed for the photocurrent in the Pup (-2.2V) state. The photocurrent decreases over time only in the Pdown (+2.6V) state and for low wavelengths.

Schottky barrier–driven photocurrent: As can be seen in figure 3.17, the ‘‘peaked’’ part of the transient photocurrent exhibits both polarization and wavelength dependence. Indeed, this ‘‘peaked’’ response is measured in the P down state, for a low polarization value and a wavelength below 350 nm (figure 3.17 d)), while it disappears at higher polarization (figure 3.17 h)) and at longer wavelengths (figure 3.17 d)). This behavior hints at a combined effect of optical absorption and Schottky barrier at the top interface, as detailed in the following.

- At 350 nm wavelength and below, the optical penetration depth is typically in the 20-60 nm range, and a large part of the charge carriers are generated in the depletion layer close to the top interface, that has a thickness in the same range (10-50 nm, depending strongly on the defect density in PZT).
- For high polarization state, the depolarizing field is thought to be the dominant driving field of the photocurrent, inducing high photocurrent in both up and down states. In the intermediate polarization states, the polarization is strongly reduced, as well as the depolarizing field, and the photocurrent values are much smaller. So the measured photocurrent in short-circuit condition and disordered polarization state can be more sensitive to the potential barriers and the built-in electric fields at both interfaces.
- At the PZT/Pt top interface, the built-in electric field is oriented upward in the case of n-type PZT or downward in the case of p-type PZT, which would cause negative photocurrent or positive photocurrent, respectively. The small negative transient photocurrent in the Pdown (+2.6V) state could thus be related to Schottky-contact PV effect if PZT is considered as a n-type semiconductor. However, from analysis of leakage current in more asymmetric device, such as ITO/PZT/SRO presented in chapter 5, our PZT thin film seems to behave rather like a p-type semiconductor.
- Trapping of photogenerated carriers at interfaces would modify the built-in potential and thus change the measured current over time, depending on the trapping time constant.

To conclude, the analysis of the time dependence of the photocurrent is rather complex and many physical mechanisms can come into play. In our device, after some transient effect, the photocurrent is mainly steady, in particular in polarized states. For the intermediate states where the ferroelectric polarization is small, the transient part of the photocurrent is more visible and could be related to changes in the potential profile by the trapping of charges, especially at interfaces.

3.3.5 Polarization and Capacitance under light

In this section, the same stack of PZT is kept under 365 nm UV illumination (diode) while measuring polarization hysteresis loop and capacitance. Polarization-voltage loop up to 6V is measured with and without UV light at 365nm with two different driving current intensities (350mA and 650mA). Polarization loops and corresponding current loops are shown in Figure

3.18. No effect of the UV illumination can be observed in these measurements. The photoconductivity is limited so there is no significant increase of leakage current.

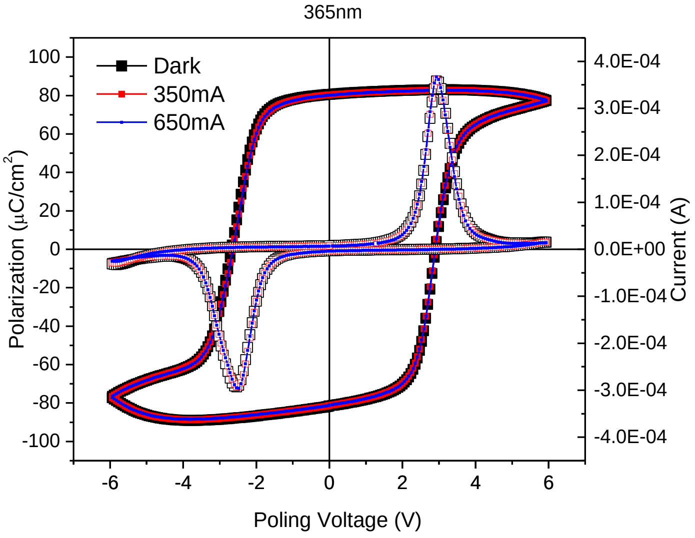

Figure 3.18. Ferroelectric hysteresis curve and corresponding current loop with and without light at 365nm wavelength.

C-V measurements were carried out at 1, 10, and 100 kHz without light by sweeping DC voltage from -4V to 4V DC as seen in Figure 3.19 (a). In Figure 3.19 (b-d), the capacitance was measured with and without UV light at 1, 10, and 100 kHz frequencies. UV light current intensity used is 350mA at 365nm wavelength. Under illumination conditions, one can observe a bump in the butterfly loop at 1 kHz frequency, which reduces with the increase of the frequency at 10 kHz and vanishes completely at 100 kHz frequency. The bumps observed under illumination before the ferroelectric switching happen when DC voltage ∼ Voc. This could be related to some space charge effects at the interfaces, with rather slow charges movement only seen at a low frequency of 1 kHz.

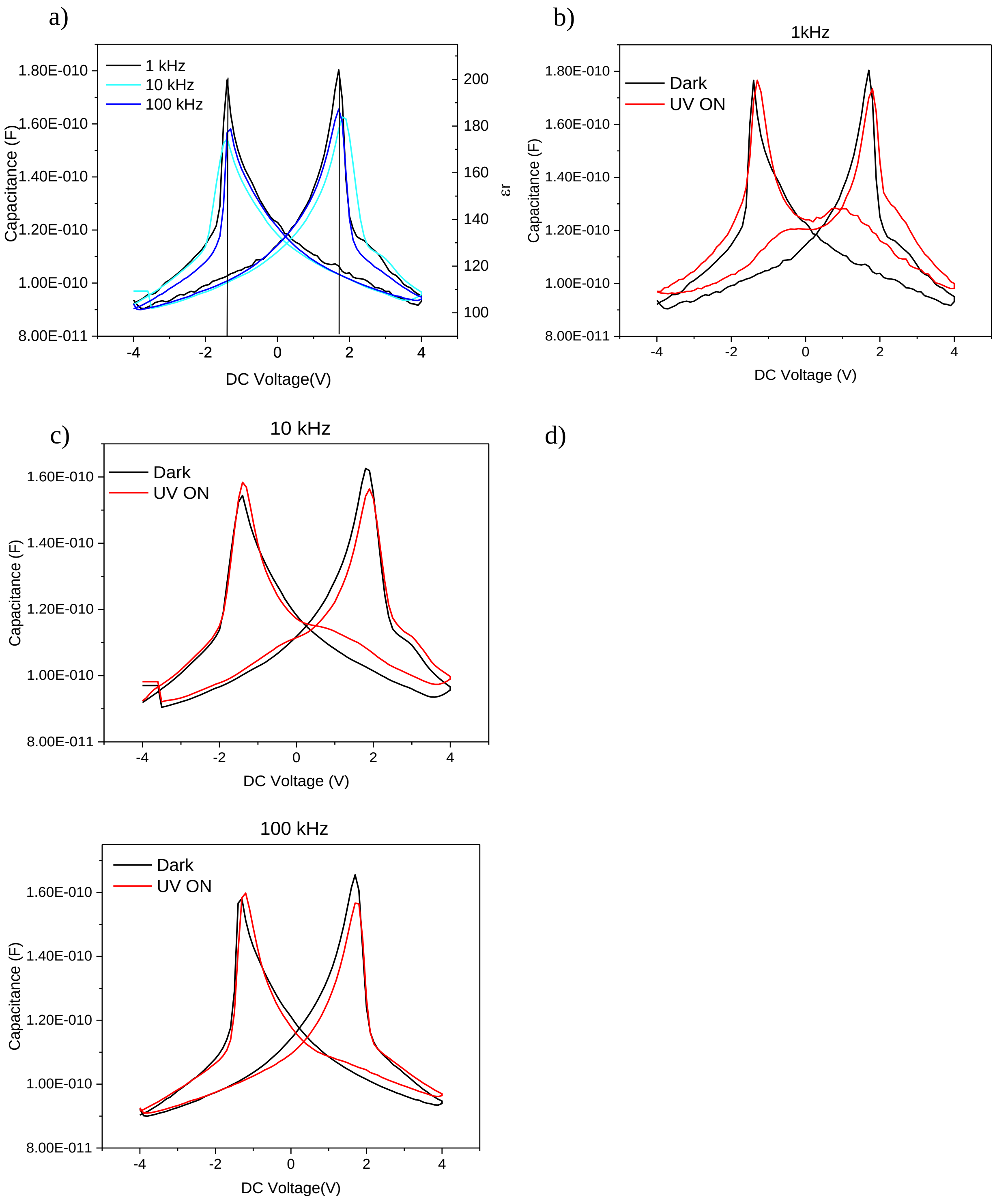

Figure 3.19. a) Capacitance-voltage curve at 1, 10 and 100 kHz under dark conditions. Capacitance-voltage at b) 1 kHz, c) 10 kHz and d) 100 kHz under dark and UV illumination conditions.

3.4 Conclusion

This chapter focused on Pt/PZT (20/80)/SRO device. The PZT 20/80 film presents good surface morphology and crystal quality. The device shows ferroelectric behavior with symmetric and high remanent polarization value of ±70µC/cm^2. The polarization exhibits good retention in open and short circuit conditions for up and down polarization state in dark. The C(V) measurements show the typical butterfly loop with dielectric constant ~200 for the 20/80 PZT. No effect of UV illumination (above PZT band gap) is seen on the ferroelectric polarization loop, while the dielectric constant is observed to be affected by light when measured at low frequency (1 kHz) in equivalent open-circuit condition in which slow charged carriers are probably migrating and trapped.

The photovoltaic properties of the device have been characterized in detail.

- First, a switchability of short-circuit current Jsc and open circuit voltage Voc is achieved by switching the polarization between P_{down} and P_{up} states (a switchability of 87% is achieved for Jsc).

- In both states, Jsc and photoconductivity are found to increase linearly with the UV fluence, while Voc reaches saturation when the UV fluence reaches a high enough value for which the photoconductivity becomes much higher that the dark conductivity. This dependence of PV properties with light fluence is in agreement with what is expected for a classical FE material with good insulating properties.

- The analysis of the wavelength dependence of the photocurrent is consistent with the optical absorption of PZT 20/80 having a bandgap of 3.3 eV. No photocurrent is detectable at photon energies below the bandgap.

- The time evolution of photocurrent under illumination shows a rather steady behavior in up and down polarization states. For intermediate states (at very low polarization values), the photocurrent shows a more pronounced transient behavior, probably because the depolarizing field which drives the photocurrent (strongly for up and down polarization state) is almost zero here. So, the photocurrent in short-circuit condition and disordered polarization state is probably more affected by the potential barriers at both interfaces and their evolution over time if charged carriers get trapped at interfaces and the polarization value get changed.

Chapter-4

Quantitative investigation of polarization-dependent photocurrent

Contents

In this chapter, a careful investigation of the polarization-dependent photocurrent of epitaxial lead zirconate titanate PZT thin films has been carried out. The purpose of this study is not to close the debate on the PV mechanisms in FE thin films, but to provide a more quantitative determination of the switchable Vs unswitchable parts of photocurrent. More precisely, the dependence of the photocurrent as a function of electrically controlled remanent polarization has been investigated. These measurements have shown that 1) the photocurrent depends linearly on the switchable part of the ferroelectric polarization and that 2) the analysis of this dependence provides important insights on the switchable and unswitchable internal electric fields in the FE material (the latter being necessarily related to pinned FE polarization). Such pinned polarization strongly affects the switchability of the PV properties in FEs and is otherwise rather difficult to probe by classical FE characterizations. These results are thus particularly relevant for the optimization of FE thin films, not only to achieve switchable PV properties but also to understand their ferroelectric response.

The results presented in this chapter have been published in Journal of Physics: Condensed Matter [97].

All measurements in this chapter were conducted under the same conditions as described in Chapter 2 on the sample number 3020 which is a Pt/PZT(100nm)/SRO sample.

4.1 State of the art

4.1.1 Photocurrent loop

It has been reported in previous studies that photocurrent can be tuned by the direction of polarization in different ferroelectrics and also makes a hysteresis loop similar to a ferroelectric hysteresis loop. These studies clearly evidence there is a relationship between photocurrent and polarization and its switchable effect. However, there is no report of a quantitative relationship between photocurrent and polarization. Some of these studies are worth mentioning here to summarize the state of the art about the relation between photocurrent and polarization.

In 1978, Micheron measured spontaneous polarization and photocurrent simultaneously under the illumination at 496nm wavelength (Intensity = 0.12 W/cm^2) at constant temperature (T=5°C) in 1mm thick $BaTiO_3$: Fe crystal. He observed the photocurrent making a hysteresis loop, as plotted on top of the polarization loop in Figure 4.1 (a). Here the origin of the photovoltaic effect is associated with a field related to the polarization [73].

Pintilie et al. in 2007 studied PZT 20/80 thin film with a thickness of 260nm on SrTiO3/SrRuO3 and a polarization of 100 µC/cm^2. In order to show the direct relation between photocurrent and polarization, the photocurrent was measured after poling the PZT sample with different voltages. The light was directed right above the Pt top electrode, using an optical fiber and the top electrode's area was 0.09±0.01 mm^2. Each poling voltage (with the reference voltage polarity on the top electrode) was applied to the film for 20 seconds. After removing the poling voltage, short-circuit photocurrent curve is measured. The results showed that the photocurrent can be switched: its magnitude depends on the magnitude of the poled polarization whereas the sign depends on the polarization direction (See Figure 4.1 (b))[98]. This photocurrent measurement can be used to perform a nondestructive readout of ferroelectric nonvolatile memory, provided that the film is imprint-free at all points and maintained in short-circuit conditions. Other studies have also reported a control of the photocurrent by the ferroelectric polarization, inducing photocurrent loop in PZT [6,73,99].

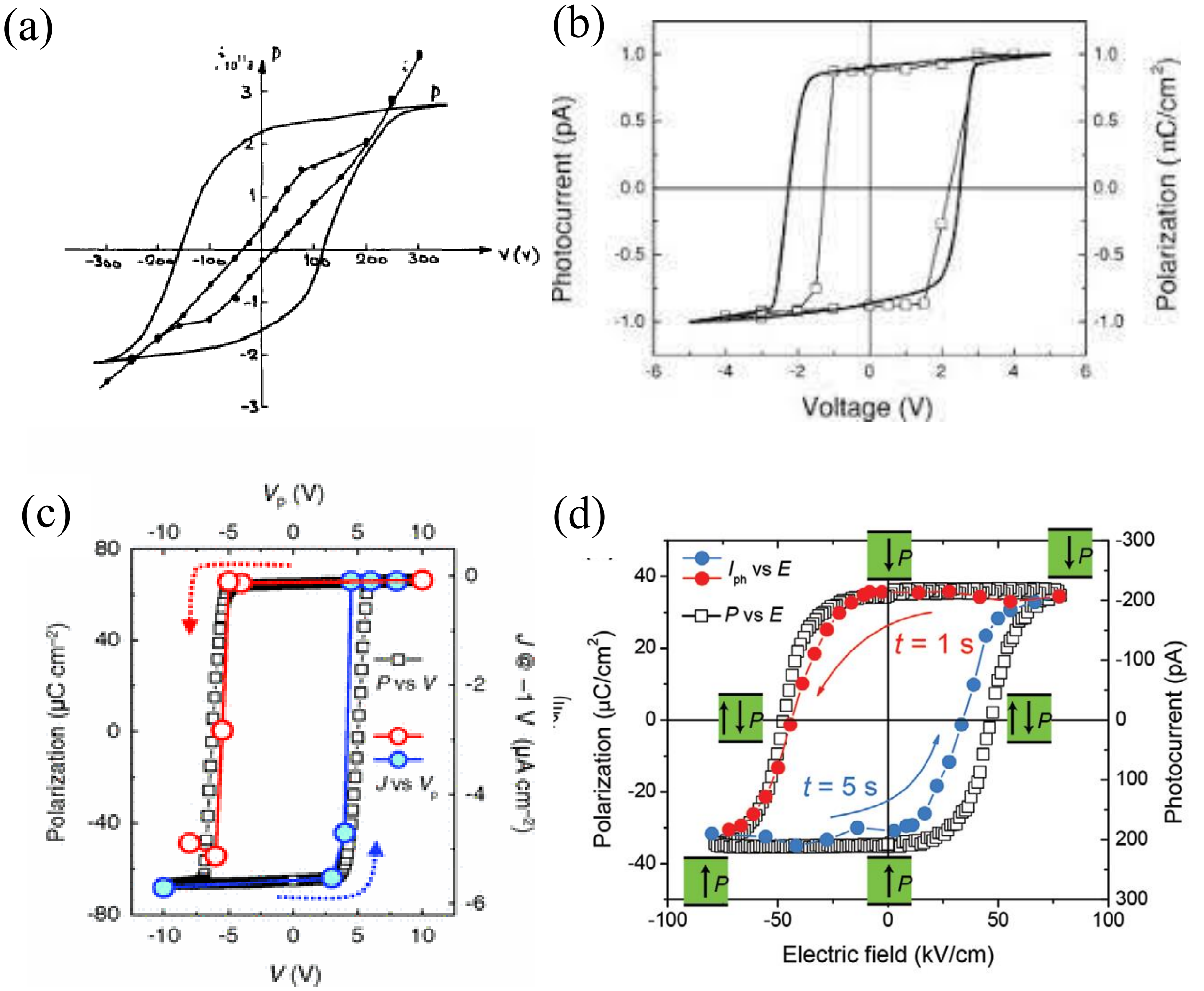

Figure 4.1. Dependence of photocurrent and polarization as a function of poling voltage in (a) BaTiO$_3$:Fe crystal, (b) 260 nm-thick PZT film, (c) 400 nm-thick BiFeO3 film and (d) 36 µm thick (0.5)Pt-(0.5)BNT ferroelectric ceramic. All photocurrent values are in short-circuit conditions, except for (c) where the current was measured at -1V. The polarization curves are obtained by classical loop measurements in (a, b, c) and by PUND in (d). (extracted from [3,73,98,100]).

In 2011 Lee et al. also showed that the photocurrent measured at -1 V follows a loop overlapping the ferroelectric hysteresis loop for 400nm thick BFO film on SrTiO3/SrRuO3 and Pt top electrode. The photocurrent was measured after 5 µs poling at different poling voltages and under 10mW/cm^2 illumination of white light. J values in the down and up polarization states are plotted as red open circles and blue solid circles as shown in Figure 4.1 (c). This result demonstrates that the diode's polarity is dependent on the ferroelectric polarization direction. Loop of short-circuit photocurrent has also been reported in BFO-based superlattices by Belhadi et al. [8].

Recently in 2021, Wu et al. reported similar results on 36 µm thick (0.5)Pt-(0.5)BNT ferroelectric ceramic with 100nm thick ITO top electrode. In this work, the influence of ferroelectric polarization on the photovoltaic response was investigated utilizing a protocol that included a poling voltage pulse followed by a short-circuit photocurrent measurement. After each voltage pulse, the short-circuit photocurrent was measured under 450 nm illumination. Figure 4.1 (d) shows the photocurrent onto polarization hysteresis loop as a function of the poling electric field. Here, the polarization curve has been measured by the PUND method, so it excludes dielectric and leakage behaviors. The significant resemblance between the switching behavior of the ferroelectric polarization and the photocurrent shows that the 0.5PT-0.5BNT ferroelectric's photovoltaic response is controlled by the ferroelectric polarization [100].

Photocurrent loops have also been reported in various other ferroelectrics, such as (Bi3.7Nd0.3)Ti3O12 (BNT) films [101] and Bi2FeCrO6 (BFCO) films [102].

Note that the above results show a photocurrent loop (where I(t) were measured under illumination in different poling states) superimposing more or less a dynamic polarization hysteresis loop. These loops were not loops of measured remanent polarization values, which could explain why the photocurrent does not switch at the same voltage than the coercive voltage.

4.1.2 Relationship between photocurrent and remanent polarization

In 2015, Liu et al. [103] investigated short circuit current and remanent polarization (Pr) relation on a BTO thin film (150nm thick) on SrTiO3/LSMO with Pt top electrode in a more detailed way (Figure 4.2(a)). In this work, photocurrent response is measured in the symmetric (between top and top electrodes) and asymmetric configuration (between top and bottom electrodes) of M/F/M devices under 266 nm wavelength with a fluence of 1.3 J/cm^2. First, polarization retention has been studied for up and down polarization state and the measurements revealed that for the top-top configuration there is a gradual loss of polarization over time (Figure 4.2(b)). When illuminating the sample and measuring the photocurrent in the same configuration, the photocurrent is also found to decrease when the time between pre-poling and photocurrent measurement increases (Figure 4.2(c)). Using these two sets of data, a linear relationship can be seen between Jsc and Pr in Figure 4.2(d) giving clear evidence that the switchable PV effect originates from the ferroelectric polarization. In this work, the depolarizing field due to inefficient screening of polarization charges at electrode interfaces is presented as the driving field behind the PV effect. The analysis of the linear Jsc-Pr relationship allowed extracting the screening efficiency at interfaces (fraction of unscreened polarization α≈0.03) for BTO and corresponding depolarizing field value of Edep =1.3 kV/cm for 1 µC/cm^2. Note that this study has reported different photocurrent values and related them to different remanent polarization states, using the low ferroelectric retention of the BTO film. In this chapter, we will define well-controlled remanent polarization states by a careful electrical poling procedure and study how they affect the photocurrent response.

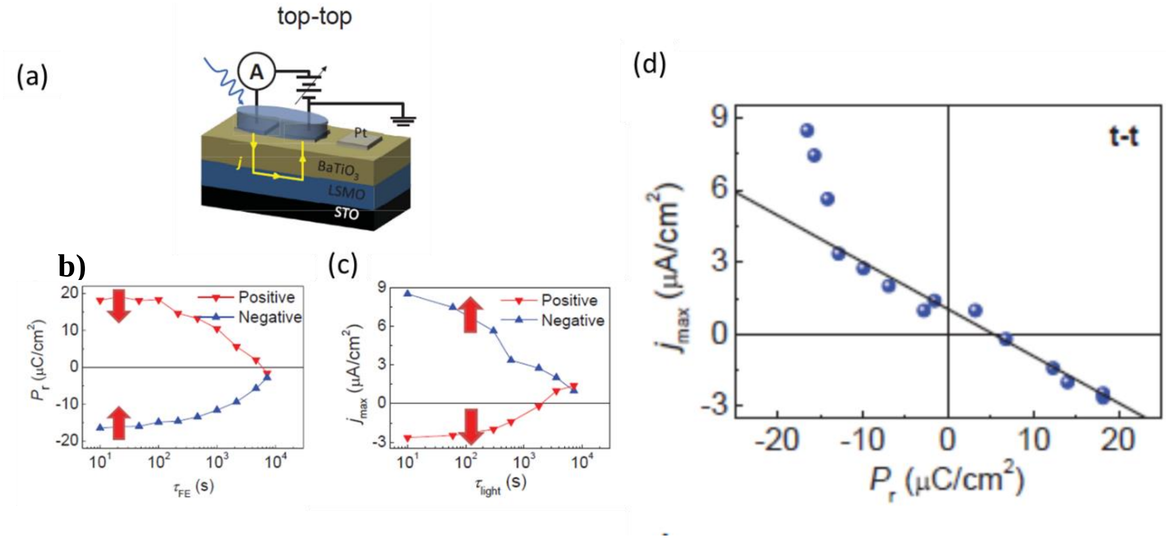

Figure 4.2. (a) Sketch of the top-top measurements configuration for BTO thin film. (b) Remnant polarization (P_r) as a function of delay time between the prepoling pulse and the measurement pulse (τ_{FE}). (c) Photocurrent maximum as a function of delay time between the prepoling pulse and the illumination (τ_{light}). (d) Dependence of the maximum of the photocurrent on the remnant polarization determined from data in (b) and (c). [extracted from[103].

4.2 Experimental protocol

4.2.1 Classical ferroelectric measurements

A classical ferroelectric hysteresis loop and a PUND polarization loop were measured using triangular pulses of 0.5 ms width. Both are shown in Figure 4.3 and exhibit close values of remanent polarization, indicating that the contribution from leakage currents is rather small in these thin films, but not negligible.

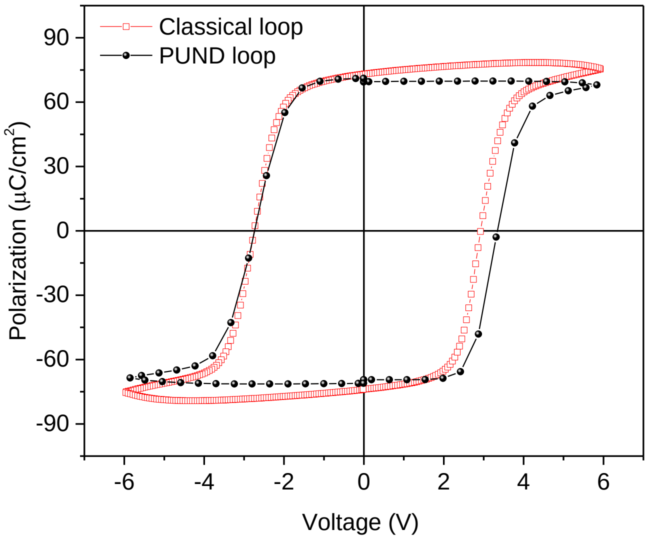

Figure 4.3. Typical ferroelectric loop in comparison to PUND polarization loop for the Pt/PZT/SRO sample.

4.2.2 Protocol to define and measure intermediate polarization states

A measurements protocol has been developed to pole the device and reach different well-defined polarization states in the PZT thin films as can be seen in Figure 4.4. The triangular voltage waveform shown in Figure 4.4 (a) consists of a writing pulse sequence to pole the sample before photocurrent measurements to precisely control its ferroelectric polarization state. This poling allows to achieve intermediate polarization ($P_{initial}$) between P_{up} and P_{down}. Figure 4.4 (b) shows examples of a ferroelectric loop from the writing sequence, following the mentioned waveform from P_{down} to P_{up} polarization state and ending at particular and well-defined intermediate states. After the photocurrent measurements, a reading pulse sequence is used to measure the polarization state (P_{final}). The method to extract this final remanent polarization value is further described in the next part. It has been shown that the remanence of polarization is good for the different polarization states ($P_{initial}$~P_{final}) at the timescale of the measurements. In the rest of the chapter, the results will refer to P_{final} as remanent polarization values.

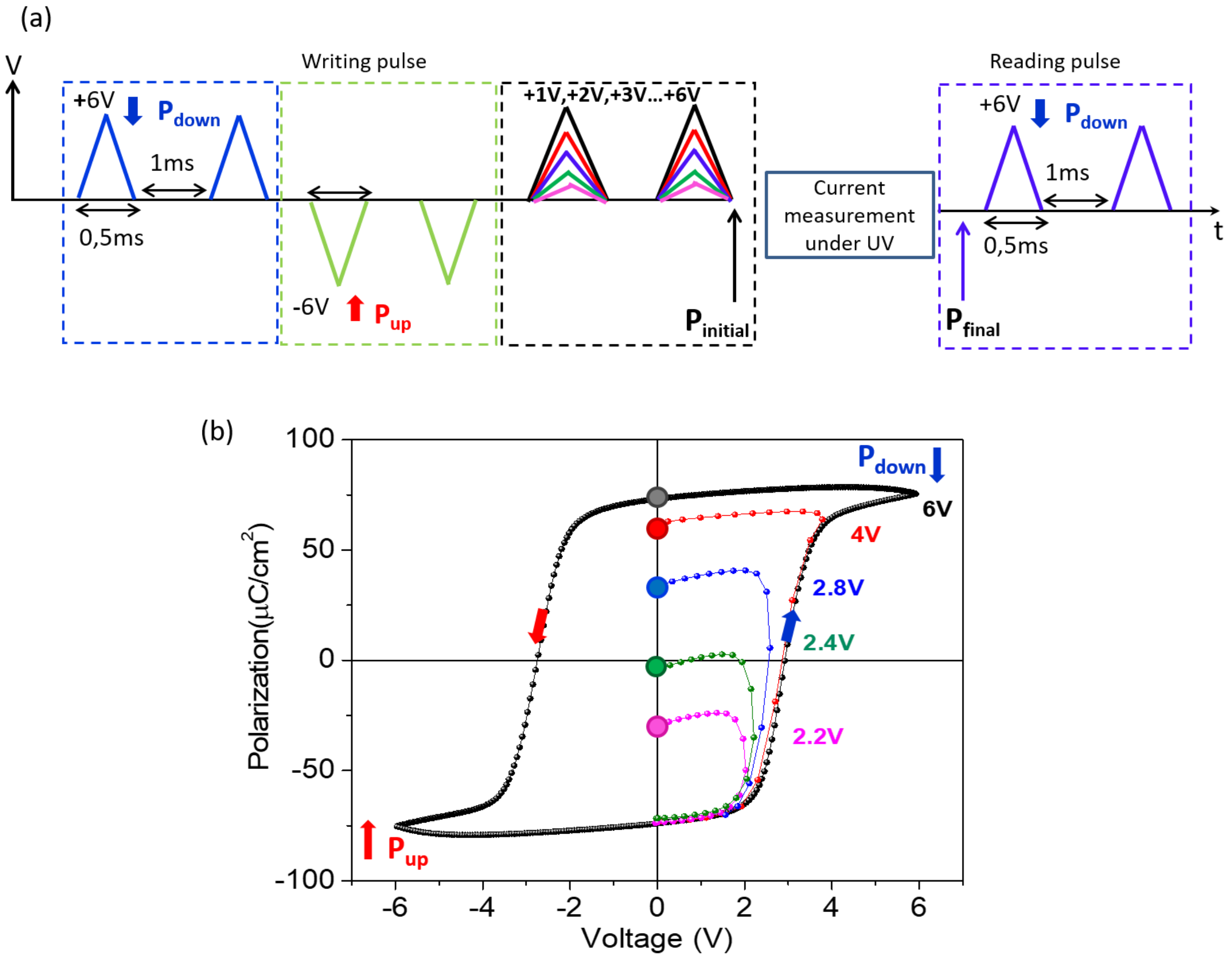

Figure 4.4. (a) Protocol for photocurrent measurements as function of different remanent polarization states. Writing pulse sequence used to pole the sample in particular polarization state and reading pulse used to extract the remanent polarization values after each photocurrent measurement. (b) Ferroelectric loop obtained by the writing pulse sequence, showing poling in different states.

4.2.3 Example of extraction of remanent polarization value

As shown in Figure 4.4(a), the voltage waveform allows poling the sample with the writing pulse, and then the photocurrent is measured under UV (diode at 365nm wavelength). After these measurements, the remanent polarization is measured with a reading pulse. Writing (blue, green, multicolor) and reading (purple color) pulses are made up of triangular pulses. In the writing waveform, a voltage pulse at +6V (writing to Pdown) is followed by a voltage pulse at -6V (writing to Pup) before poling the sample to an intermediate polarization by +1V, +2V, etc. This waveform allows to pole the sample in intermediate states by stopping at different positions on the -6V to +6V half hysteresis loop (as shown in Figure 4.4(b)). Writing pulse sequence with opposite sign is also used to pole the sample in opposite polarization intermediate states by stopping at different positions on the +6V to -6V half ferroelectric hysteresis loop.

Repeating +6V and -6V pulses twice allows to remove the dielectric contribution and the presence of possible leakage current, like in the usual PUND method. Using +6V and -6V pulses in the writing sequence provides thus access to the amount of switchable polarization (called Pref, which is purely ferroelectric) from Pdown to Pup state (Figure 4.5). The final polarization value (Pfinal) is measured by the reading pulse which gives access to the amount of polarization (Prest) which can still be switched from up to down. The two +6V pulses of the reading sequence allows here also to give access to Prest, without any non-ferroelectric contribution. Using the above methodology, the final remnant polarization value can be calculated using the formula below

$$Pfinal = \frac{Pref}{2} - \ Prest$$

Pfinal will be maximum when the sample is completely poled down by a +6V pulse at the end of the writing sequence (Prest would be zero), while Pfinal would be minimum when the sample is completely poled up by -6V writing pulse (Prest would be maximum).

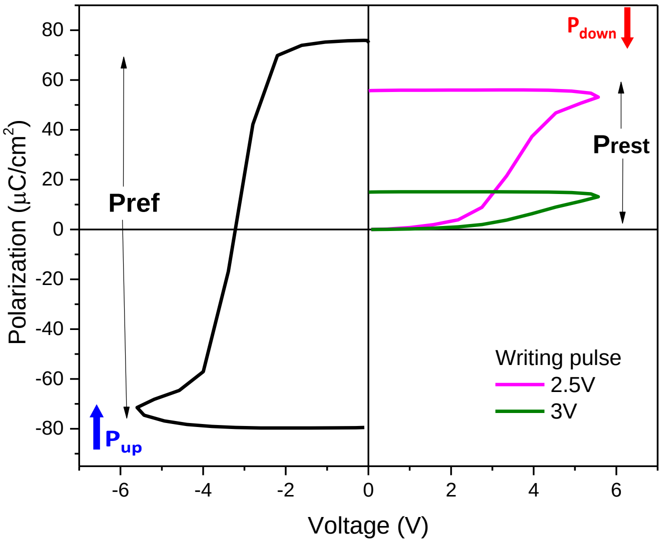

Figure 4.5. Half loop for negative voltage showing the amount of switchable polarization (Pref) from Pdown to Pup state after removing the leakage contribution obtained during the writing pulse. After polarization writing and photocurrent measurements, the amount of polarization without leakage (Prest) which can still be switched down is measured by the positive voltage during the reading pulses. Prest is shown for writing pulse of 2.5V and 3V.

4.3 Photocurrent in different polarization states

4.3.1 Photocurrent measurements

Figure 4.6 shows steady state short-circuit photocurrent measured at various intermediate poling states in dark and under illumination. A multistate switchable photocurrent can be achieved, like it was reported in $PbTiO_3$-based solid solutions ceramics [100]. These measurements agree well with the I(V) measurements (chapter 3 in Figure 3.6) giving negative J_{sc} for P_{down} state, positive J_{sc} for P_{up} state and a highest J_{sc} in absolute value for P_{down} state. J_{sc} changes sign along the intermediate states when the poling voltage V_p is close to 2.4V. Similar measurements (shown in Figure 4.7) have also been performed by starting with the P_{down} state (+6V poling) and progressively switching the polarization until the P_{up} state (-6V poling).

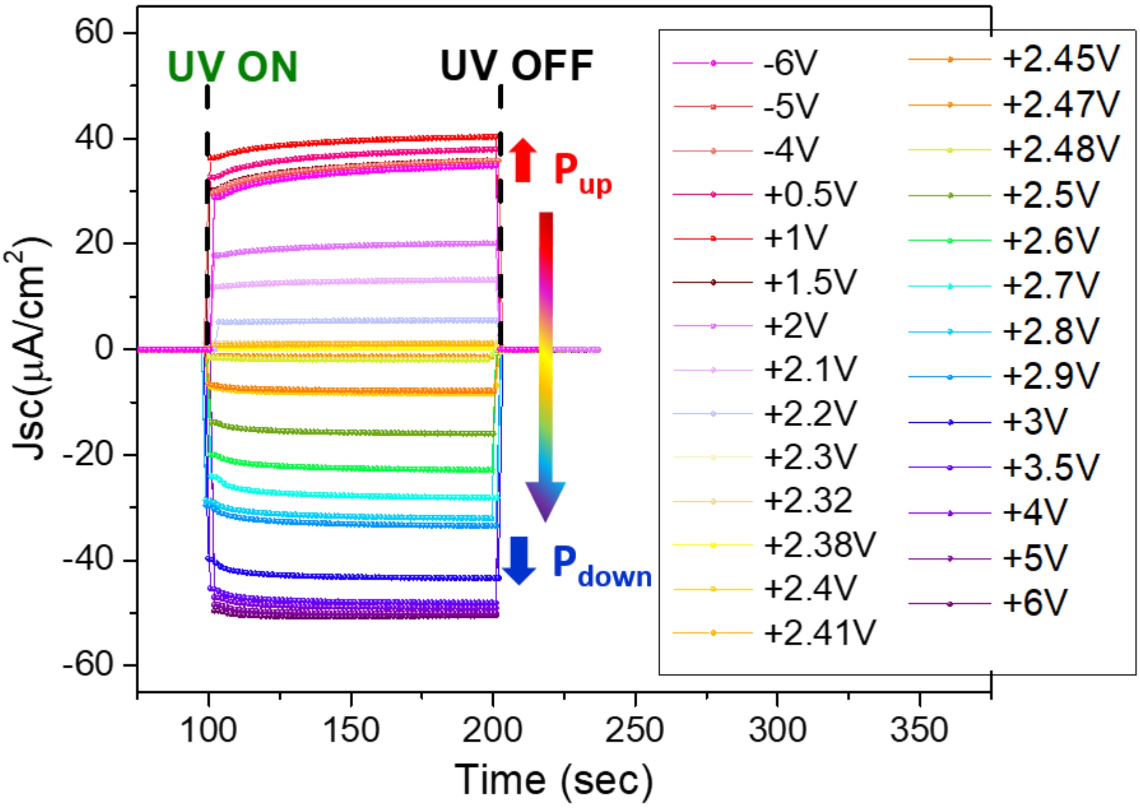

Figure 4.6. Time-dependent J_{sc} under UV ON and OFF condition for -6V poling (P_{up} state), +6V poling (P_{down} state) and different intermediate polarization states (while partially switching the polarization from P_{up} to P_{down} by applying positive poling voltage V_p).

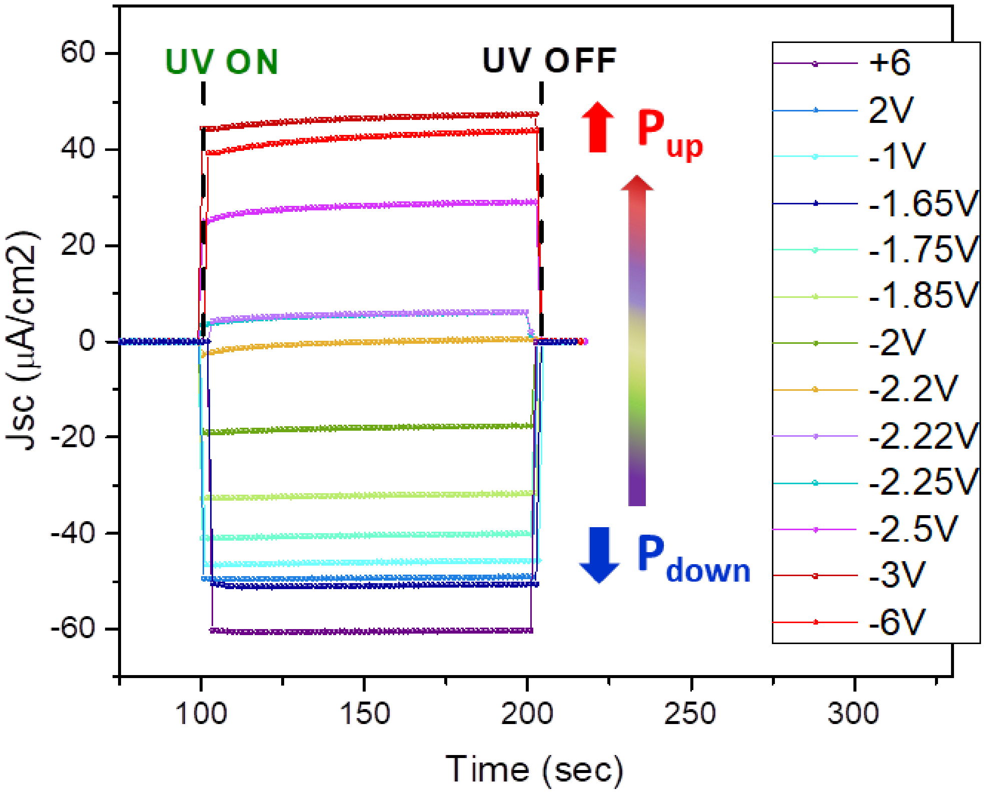

Figure 4.7. Time-dependent J_{sc} under UV ON and OFF condition for +6V poling (P_{down} state), -6V poling (P_{up} state), and different intermediate polarization states (while partially switching the polarization from P_{down} to P_{up} by applying negative poling voltage V_p).

4.3.2 Photocurrent loop

The J_{sc} value measured right before switching off the illumination for each poling state (in Figure 4.6) was extracted and plotted as a function of poling voltage V_p in Figure 4.8. The J_{sc}-V_p curve clearly follows a hysteresis loop. In addition, after each photocurrent measurement, the final remanent polarization P_r=P_{final} was extracted using the previously mentioned protocol and plotted against the poling voltage. P_r-V_p follows a ferroelectric hysteresis loop, plotted in black in Figure 4.8, which, like the PUND polarization loop, also exhibits an asymmetry in coercive voltage towards positive values (V_p=-2.1V and +2.4V). However, the maximum and minimum P_r values for both +6V and -6V poling voltages are comparable (+67μC/cm² and -70μC/cm²), which indicates that the same amount of polarization can be poled up and down with good remanence. The P_r-V_p loop exhibits the same “coercive” poling voltage as for the photocurrent loop, indicating that the remanent polarization (P_r) and the short-circuit photocurrent (J_{sc}) are closely related. In this work, the similarity between both loops is remarkable and much stronger than in previous studies mentioned before [3,6,73,98,100]. Indeed, it is evidenced here that the photocurrent loop is not to be compared with a classical ferroelectric hysteresis loop but rather to the loop of the remanent polarization which is measured for each poling voltage.

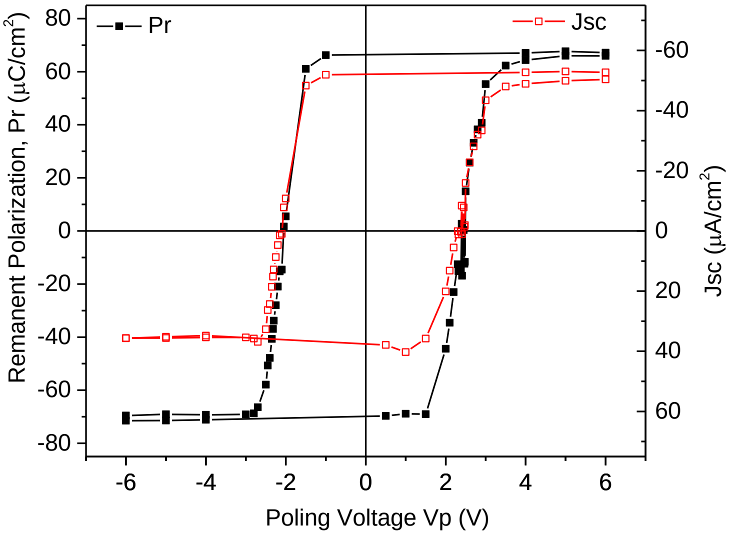

Figure 4.8. Loop of measured remanent polarization (P_r) and short-circuit photocurrent (J_{sc}) loop plotted as function of the poling voltage (V_p), showing similar hysteretic shape.

4.4 Quantitative relationship between photocurrent and polarization

4.4.1 Linear dependence of photocurrent with the remanent polarization

To study quantitatively the relationship between P_r and J_{sc}, J_{sc} was plotted as a function of P_r in Figure 4.9. The linear dependence between P_r and J_{sc} is conspicuous over the whole range of polarization states. Note that the P_r values are remanent polarization values, which can only be measured by switching the polarization. From the polarization measurements alone, there is thus no way to evidence the possible presence of a polarization that cannot be switched during the pulse sequence. The observed experimental dependence in Figure 4.9 clearly proves that the short-circuit photocurrent J_{sc} is proportional to the total ferroelectric polarization in the ferroelectric devices.

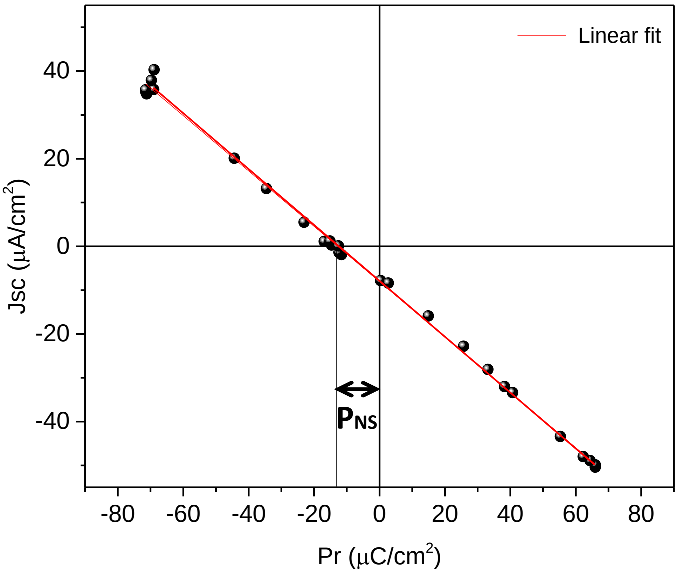

Figure 4.9. Linear dependence of photocurrent (J_{sc}) with the measured remanent polarization (P_r) in Pt/PZT/SRO-based capacitor device. J_{sc} reaching zero for a non-zero P_r value evidences the existence of a non-switchable polarization (P_{NS}) within the film.

4.4.2 Quantitative determination of unswitchable polarization

The fact that J_{sc} reaches zero for a non-zero P_r value demonstrates thus the presence of a non-switchable polarization part (P_{NS}) in the film. This P_{NS} contribution to the total polarization in the film can be quantitatively obtained from the J_{sc}-P_r measurements. J_{sc} equals zero when the switchable remanent polarization P_r (controlled by poling) compensates the non-switchable polarization part (P_{NS}) in the film. J_{sc} equals zero for a measured P_r of -12µC/cm², meaning that P_{NS} is positive (pointing down) and equals 12µC/cm². One should emphasize here that this polarization of 12µC/cm² is not related to imprint induced fast back switching of very mobile domains, since the Pr-hysteresis loop exhibits similar values for both poling directions. This polarization of 12µC/cm² is rather an equivalent polarization which exists in the film and is not affected by the poling. It can then be referred to as a pinned polarization which is not probed by the ferroelectric hysteresis measurements but revealed by the photocurrent measurements.

Note that the origin of this pinned part of polarization is unknown and would deserve more investigation. It could be related to an inhomogeneous distribution of charged defects within the thickness and/or to the asymmetry between the potential barriers at bottom and top interfaces (higher built-in electric field pointing up at the PZT/Pt interface), in agreement with the shift of the polarization loop which suggested an internal electric field pointing up [104]. The presence of this P_{NS} part explains thus why higher J_{sc} is measured in absolute value in the P_{down} state. In the +6V state, both P_{NS} and P_r add up, reaching a total equivalent polarization P_{tot} of +79µC/cm² pointing down, while in the -6V state, P_{tot} is smaller and reaches only -58µC/cm². The detailed investigation performed here on the photocurrent is thus a very powerful experimental method to access quantitatively the switchable behavior of the polarization in a ferroelectric thin film.

4.4.3 Analysis of the PV mechanism

Now, the linear relationship between J_{sc} and P_r could be explained rather by the bulk PV mechanism and/or by the presence of an internal field in the film proportional to P_r with opposite sign. This second mechanism will be tested in the rest of this chapter, in a similar way as done in [103]. The depolarizing field, which opposes the polarization, is related to the incomplete screening at the ferroelectric-electrode interfaces. Mehta et al. proposed a classic model for depolarization in ferroelectrics with metal electrodes in 1970 [105]. With the screening effect and the depolarization field, many models were proposed in which screening charges were dependent not only on electrodes but also on the properties of ferroelectric films [106,107]. From the experimental results of the current study, J_{sc} can be written as

$$J_{SC} = J_S + J_{NS} \qquad (4.1)$$

Where J_S is the switchable part of short-circuit photocurrent and J_{NS} the non-switchable part (J_{NS}=-8µA/cm²). J_S is thus experimentally proportional to the switchable remanent polarization (P_r). P_r can be related to the presence of a depolarizing field [105].

$$Edep = -\alpha \frac{P_r}{\varepsilon} \qquad (4.2)$$

with ε the dielectric permittivity of the ferroelectric layer and α the fraction of unscreened switchable polarization. J_S can be expressed as,

$$J_S = \sigma \, Edep \qquad (4.3)$$

with σ the photoconductivity. In this picture, the relationship (4.4)

$$J_S = -\sigma \, \alpha \, \frac{P_r}{\varepsilon} \qquad (4.4)$$

would then account for the experimental proportionality between J_s and P_r. However, this assumes that both ε and σ are the same in different P_r states, which is not the case as shown in Figure 4.10. In a ferroelectric layer, the dielectric constant is known to follow a butterfly loop as function of DC voltage with maximum values at the ferroelectric switching (Figure 4.10 (a)). To take into account the dependence of the dielectric constant with the polarization state, capacitance has been measured in short-circuit condition and under light illumination for each intermediate P_r states. The dielectric constant, plotted as function of P_r in Figure 4.10 (b), shows maximum values achieved when the polarization is close to zero and the values change by 27% in the whole P_r range. The photoconductivity σ was also measured from the slope of I-V curves in the +0.1V/-0.1V range for each Pr state (Figure 4.10 (c)). σ decreases for increasing positive P_r values (P_{down} state) and changes by 48% in the whole P_r range. Note that the same voltage protocol (Figure 4.4 (a)) was used to pole the sample in the different

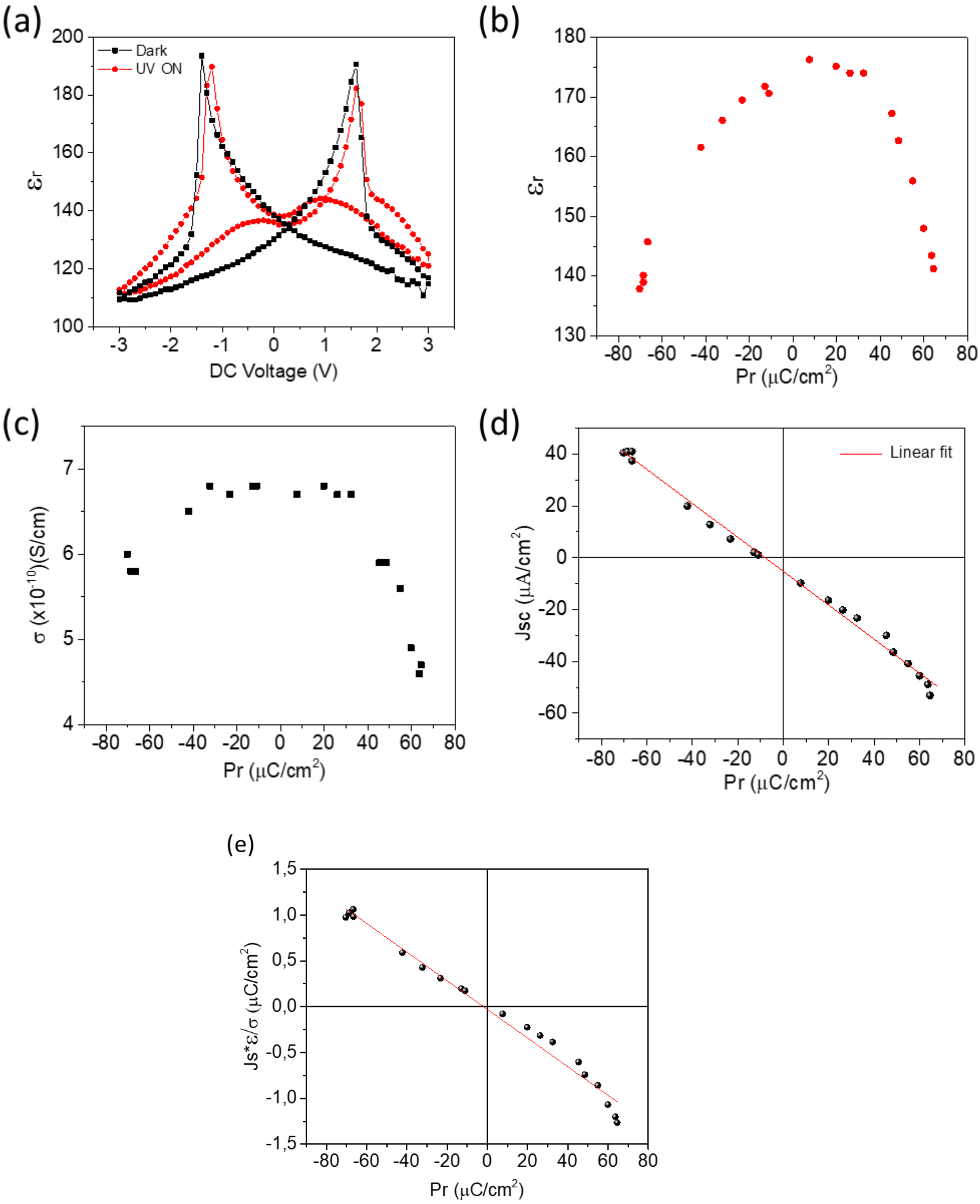

Figure 4.10. (a) Dielectric constant measured as function of DC voltage (using AC voltage of 30 mV and 1 kHz) in dark and under illumination conditions. The bumps observed under illumination (as already reported in chapter 3) before the ferroelectric switching happen when DC voltage ~V$_{oc}$ and could be related to space charge effects at interfaces. (b) Dielectric constant as function of P$_r$ state measured under illumination. (c) Photoconductivity as function of P$_r$. (d) New data set of short-circuit photocurrent (J$_{sc}$) as function of the measured remanent polarization (P$_r$), used to take into account the dependence of the dielectric constant and the photoconductivity on the polarization state. (e) J$_S$ ε /σ values plotted as function of P$_r$, using the Jsc data in (d).

intermediate P_r states before measuring the photocurrent (Figure 4.10(d)), the capacitance in short-circuit condition and under light illumination, and the photoconductivity to get a complete data set. P_r was further measured using the reading pulse sequence of the protocol.

The dependence of both ε and σ with the polarization state could invalidate the model of depolarizing field to account for the linear relationship between J_{sc} and P_r. From equation (4.5), J_S ε /σ is directly opposite to the unscreened polarization:

$$\frac{J_S\,\varepsilon}{\sigma} = -\alpha P_r \qquad (4.5)$$

For each P_r state, corresponding ε and σ values have thus been considered and the J_S ε /σ product has been plotted as a function of P_r (Figure 4.10 (e)). J_S ε /σ does still appear proportional to P_r, so the model of depolarizing field cannot be discarded as the origin of the photocurrent in these films in favor of the bulk PV effect. The linear fit of J_S ε /σ as a function of P_r gives a slope that is directly the opposite of the fraction of unscreened polarization α. A value of α=0.015 is obtained which is in agreement with the expected order of magnitude for screening efficiency [105] and consistent with the value reported for $BaTiO_3$ [103]. From this value of α and equation (4.2), an effective depolarizing field can be estimated and is found to be 85 kV/cm, corresponding to 0.85V, for P_r=70 µC/cm² and ε_r=140. In the case of bulk PV effect, V_{oc} larger than the corresponding depolarizing field can be achieved. Here, the open-circuit voltage reaches only 0.52V maximum, which is below 0.85V. In conclusion of this part, from the obtained experimental data, bulk PV, as well as depolarizing field models, can both be at the origin of the measured photocurrent in these PZT thin films.

4.5 Conclusion

In conclusion, the short-circuit photocurrent has been measured in PZT epitaxial thin films for electrically written and stable intermediate remanent polarization states. A clear linear dependence between the photocurrent and the remanent polarization has been evidenced and the quantitative analysis of these results allowed to reveal the presence of a pinned part of polarization in the layer, which explains why the photocurrent is not 100% switchable by electrically poling the ferroelectric film. While the linear relationship could not help elucidating the origin of the photocurrent (which can be bulk PV and/or related to depolarizing field), the developed method is useful to reveal unswitchable part of polarization in a ferroelectric layer. It thus provides important insights on the ferroelectric behavior in all types of ferroelectric layers, while the classical ferroelectric loop only gives a partial picture of the switchable polarization. Pinned polarization could be related to defects, in particular at interfaces with electrodes [108]. So, this type of study of photocurrent as function of remanent polarization could serve as an efficient tool to characterize the quality of a ferroelectric film integrated in capacitor.

Investigating different types of electrode materials appear interesting to find out how it will affect the part of unswitchable polarization and if different screening efficiencies can be achieved and quantified. This is the subject of chapter 5.

In this particular research field of PV in ferroelectrics, the results presented here provide a general approach to study and optimize the switchability of photocurrent, which could have far-reaching implications for future photo-ferroelectric memory applications.

Chapter-5

Influence of metal/ferroelectric interfaces

Contents

In this chapter, the influence of the electrode/ferroelectric interface on photocurrent switchability in PZT capacitors was investigated. The first section presents the surface and structural properties of PZT films deposited on different electrodes. In the second and third sections, a comparative study is presented between top electrodes of Pt and ITO on PZT ferroelectric films grown on SRO and LSMO bottom electrodes. The fourth section focuses on the effect of a STO buffer layer at the top electrode/ferroelectric interfaces. These last three sections include measurements of ferroelectric and photovoltaic properties and the study of the polarization-dependent photocurrent. The polarization screening efficiency in the different heterostructures was also extracted. All results are compared in the last part. The results about the insertion of STO at the bottom interface are preliminary and presented in annex.

5.1 Surface and structural characterization

5.1.1 Atomic force microscopy

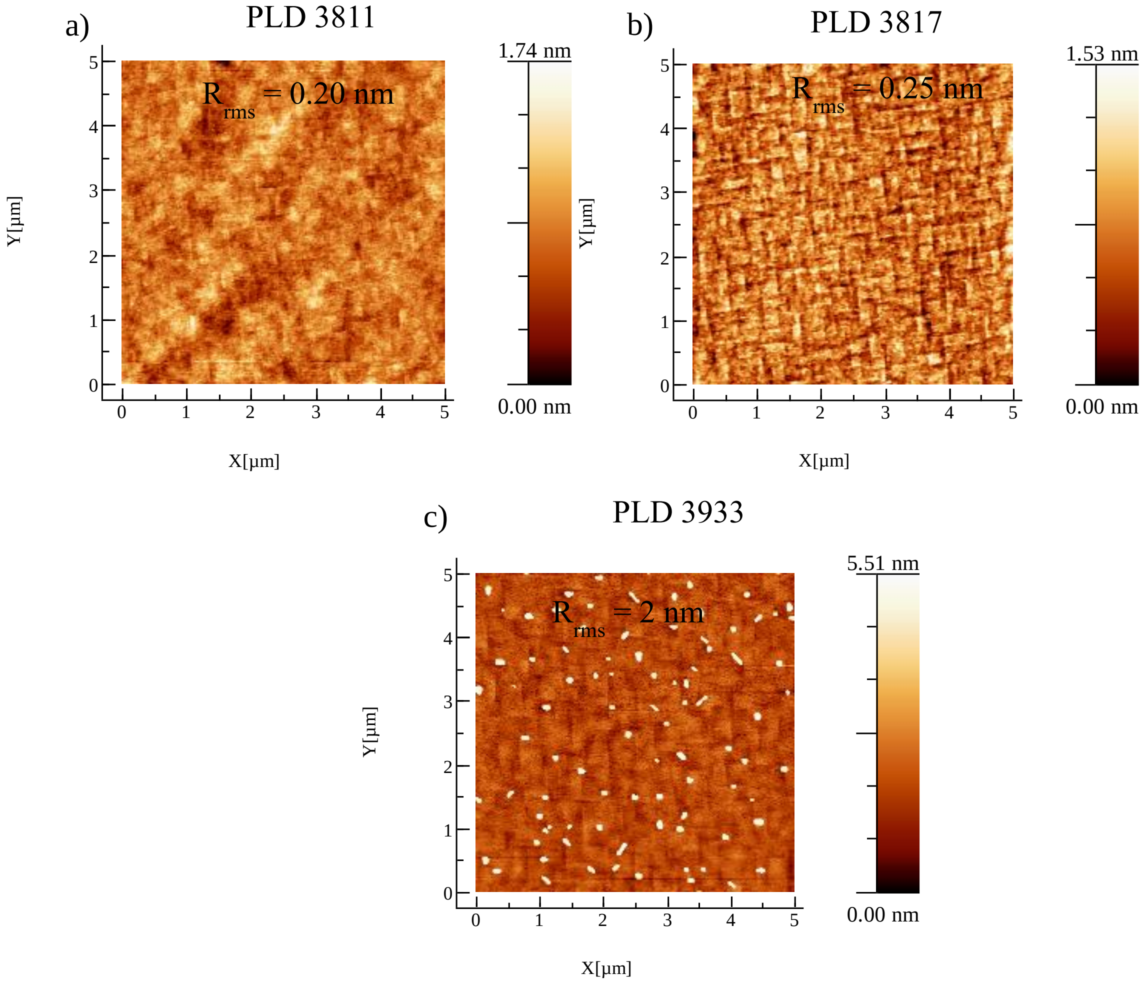

Figure 5.1. AFM topography image of a) PZT/SRO/STO, b) PZT/LSMO/STO, c) STO (1nm)/PZT/SRO/STO.

The surface morphology of all the samples was analyzed by atomic force microscopy (AFM). The AFM measurements show a smooth surface for all the samples, namely PZT/SRO, PZT/LSMO and STO(1nm)/PZT/SRO on (001) STO substrate, as shown in Figure 5.1 (a-c). For all samples, the thickness of PZT, SRO, LSMO, and thin STO is measured as 120nm, 37nm, 30nm, and 1nm. The roughness R_{rms} is 0.20nm, 0.25nm, and 2nm for PZT/SRO, PZT/LSMO, and STO(1nm)/PZT/SRO samples. While the ferroelectric polarization is mainly out of the plane, the PZT/SRO, PZT/LSMO, and STO(1nm)/PZT/SRO samples exhibit ferroelastic domains with small areas of in-plane polarization (evidenced on the topography images by vertical and horizontal lines). The presence of such ferroelastic domains is more prominent in the PZT/LSMO stack in Figure 5.1 (b). The defects imaged as white dots on figure 5.1c) are typical of non stoichiometric PZT precipitates and not due to the STO layer grown on top. On this STO(1nm)/PZT/SRO sample, most of the surface (>95% of area) is smooth (0.2nm rms) without defects, like for the other samples.

5.1.2 X-ray diffraction

High-quality epitaxial PZT films that have been obtained in the three stacks as can be seen in θ-2θ scans, showing only the (00l) family of Bragg peaks for PZT, as well as the bottom electrode layer (SRO or LSMO) and the STO substrate (Figure 5.2 a-c). The rocking curve around the (002) PZT Bragg peak shows a quite narrow full width at half maximum (FWHM) (typically 0.1-0.2°), indicating a good crystalline quality with low mosaicity. The out-of-plane c lattice parameter of SRO and LSMO are 0.395 nm and 0.386 nm, respectively. The c lattice parameter of PZT is 0.411-0.412 nm, consistent with the tetragonal structure of $Pb(Zr_{0.2},Ti_{0.8})O_3$ composition.

a) PLD 3811: PZT/SRO/STO

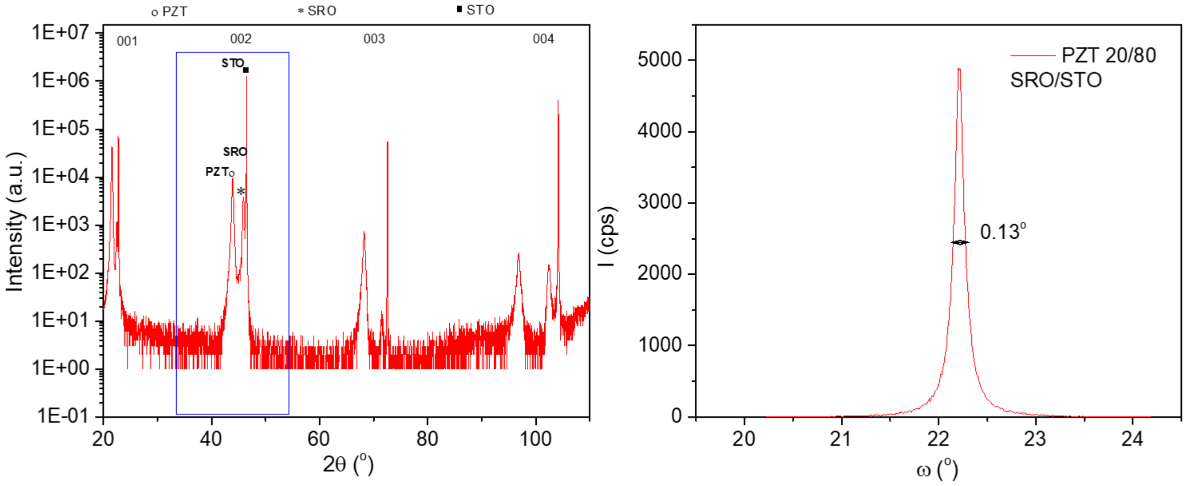

b) PLD 3817: PZT/LSMO/STO

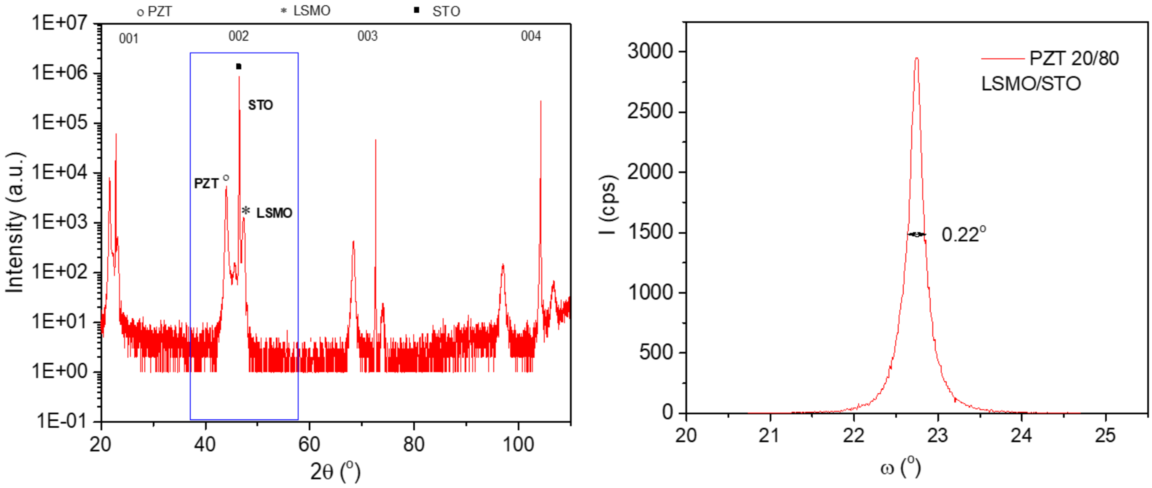

c) PLD 3933: STO(1nm)/PZT/SRO/STO

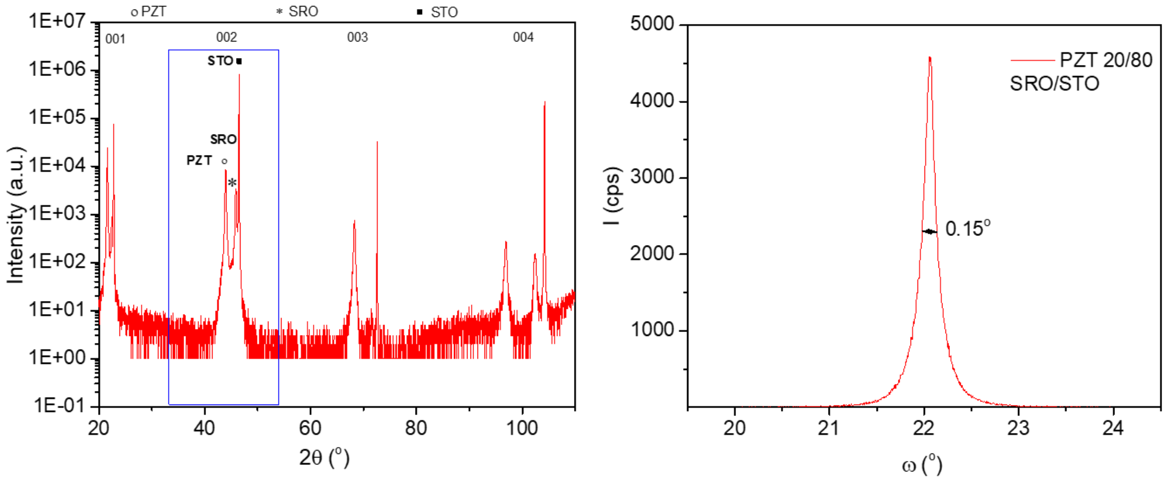

Figure 5.2. θ-2θ XRD curve and corresponding rocking curve around the (002) PZT Bragg peak for a) PZT/SRO/STO, b) PZT/LSMO/STO, c) STO (1nm)/PZT/SRO/STO.

5.2 SRO/PZT with Pt or ITO top electrode

In this section effect of Pt and ITO top electrodes with SRO bottom electrode is evaluated on ferroelectric and photovoltaic properties. Note that capacitors with top Pt and with top ITO electrodes have been patterned on the same PZT/SRO sample in order to make a more precise comparison between Pt and ITO top electrodes.

5.2.1 Ferroelectric measurements

Ferroelectric hysteresis loops were measured at 1 kHz on PZT/SRO capacitors (of 100x100µm^2 lateral size) with Pt and ITO top electrode in Figure 5.3 (a-b). The polarization curve seems symmetrical with no contribution from leakage current in the case of Pt. The remanent polarization ±P_r values and coercive voltages ±V_c for Pt are ±65 µC/cm^2 and -2.5 V, and 2.8 V. Whereas the polarization curve with ITO top electrode shows an asymmetric behavior where the loop is shifted to the positive side (V_c = -2.3V and 4.2V). This positive shift of+0.95V on the voltage axis indicates the presence of imprint field in the up direction. The ITO/PZT/SRO capacitor also presents a high leakage contribution in the ferroelectric measurements, leading to a significant overestimation of the remanent polarization value.

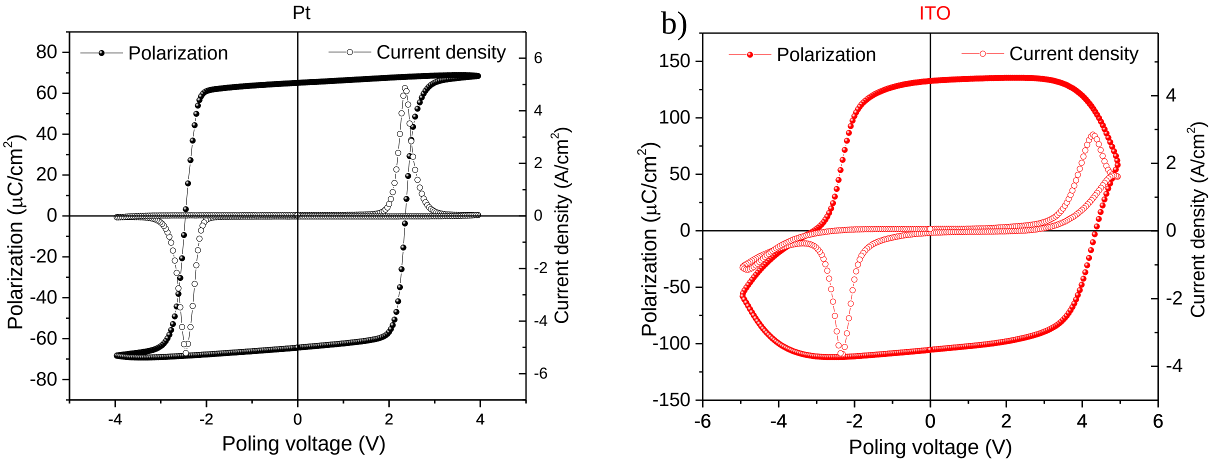

Figure 5.3. Ferroelectric hysteresis loop for top electrode a) Pt and b) ITO on PZT/SRO.

5.2.2 Photovoltaic measurements

The photovoltaic properties of the PZT/SRO capacitors were obtained under the illumination of 365nm (350 mA diode driving current and 45.5 mW/cm^2 incident fluence) wavelength in two distinct polarizations for the Pt and ITO top electrodes. The absorption value for the electrodes Pt and ITO are 55% and 4%. The Pt and ITO devices were pre-polarized before photocurrent measurement at ±4V and ±5V to reach P_{down} and P_{up} state.

I-V measurement

The photocurrent was measured as a function of voltage, as shown in Figure 5.4. In Figure 5.4 (a), for Pt top electrode, the Jsc value is slightly higher in absolute value for the P_{down} state (-0.37 mA/cm^2) in comparison to the P_{up} state (0.19 mA/cm^2) despite having similar Pr values. This result is similar to chapter-3 for Pt/PZT (100nm)/SRO sample. In contrast, the Voc values for the P_{down} state are smaller (0.76 V) than (-0.84 V) for the P_{up} state. In the case of ITO (Figure 5.4 b), the Jsc and Voc values for up and down states are (0.39 mA/cm^2, -1.5V) and (-0.24 mA/cm^2, 0.48V). The ITO/PZT/SRO capacitor thus presents a bit higher photocurrent switchability between up and down polarization states: 87% for ITO/PZT/SRO compared to 76% for Pt/PZT/SRO. Note that the switchability value for the other Pt/PZT/SRO stack studied in chapter 4 reaches 85%; this variability could come from slightly different growth parameters since the sample studied in chapter 4 was grown from an older PZT ceramic target. The switchability in Jsc values for all capacitors is listed in the comparison part in table 5.2.

In the ITO/PZT/SRO capacitor, the asymmetry in Jsc values (with higher Jsc in absolute value in the P_{up} state) is not consistent with what would be expected from the shift of the P-V loop, where the up-imprint field should give rise to a higher photocurrent in the P_{down} state where it adds up to the up depolarizing field. Discussion will be presented in the last part of the chapter.

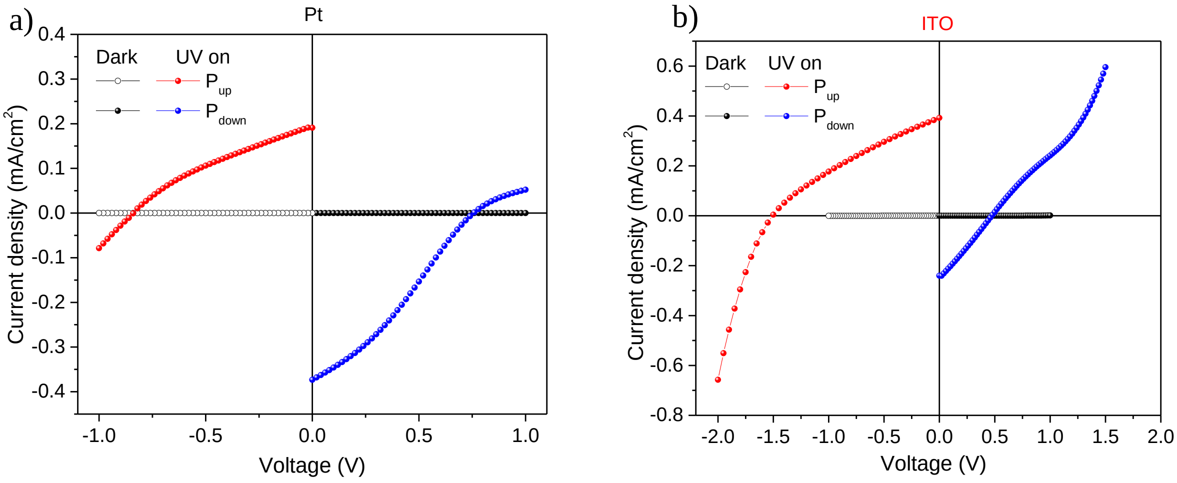

Figure 5.4. J-V measurement in up and down polarization state for a) Pt and b) ITO top electrode on PZT/SRO sample under dark and UV illumination.

I-T measurement

The photocurrent measurement (J(t) $_{v=o}$) as a function of time in short circuit condition can be seen in Figure 5.5 (a-b). In the case of Pt, Jsc values are 0.19 mA/cm^2 and -0.37 mA/cm^{2,} and for ITO, Jsc values are 0.39 mA/cm^2 and -0.29 mA/cm^2, which is consistent with the values extracted from the J-V curves (Figure 5.4). Jsc shows steady behavior over time in up and down polarization states for both top electrodes.

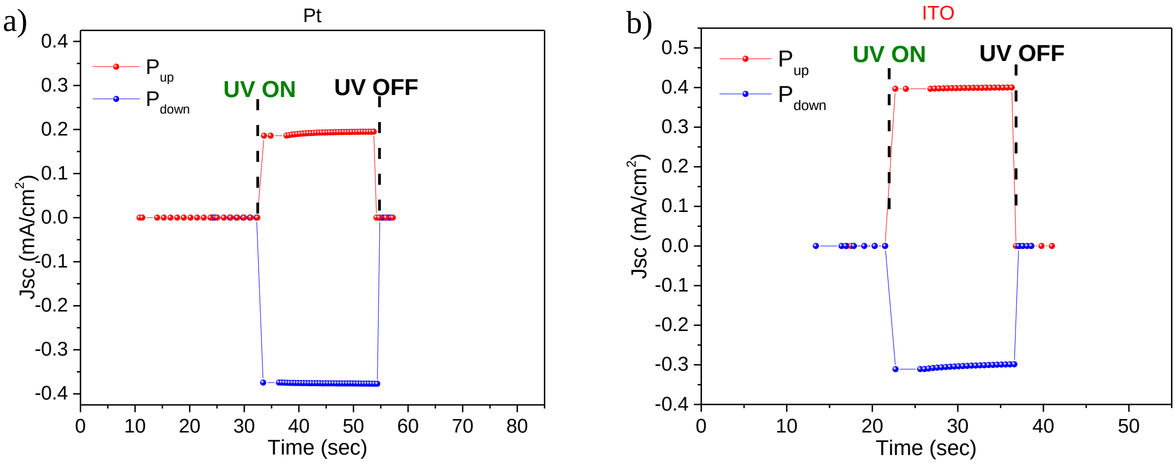

Figure 5.5. J-t measurement in up and down polarization state for a) Pt and b) ITO top electrode on PZT/SRO sample.

5.2.3 Jsc-Pr relation

The relationship between Pr and Jsc was already investigated quantitatively in chapter 4 for a SRO/PZT/Pt device, where Jsc shows a linear dependence with Pr. For the two devices here, the photocurrent has only been measured for the up and down states and not for intermediate polarization states. For the SRO/PZT/Pt device, the Jsc values extracted from the J-t measurements are plotted against Pr values extracted from a PUND protocol (Figure 5.6 a). For ITO-based device, however, the pulse sequence does not allow to remove efficiently the leakage contribution, as it can be seen in figure 5.6 b. The difficulty comes from the fact that the leakage current is quite high and overlaps the switching current peak for positive applied voltage. The leakage current was too high to apply voltage above 5 V, and this voltage was insufficient to measure completely the polarization switching by positive pulse (due to the shift of P-V loop). With the actual data for ITO device, it is thus not possible to extract Pr values and study the dependence of Jsc with Pr.

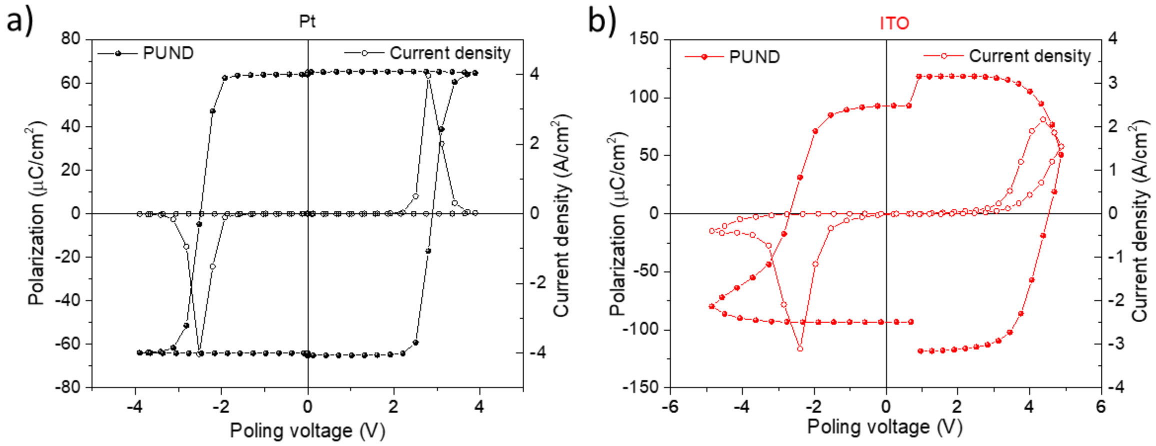

Figure 5.6. PUND ferroelectric hysteresis loop for top electrode a) Pt and b) ITO on PZT/SRO.

The plot of Jsc-Pr for Pt/PZT (120nm)/SRO device in Figure 5.7 (a) is showing a similar trend as Pt/PZT (100nm)/SRO device analyzed in chapter 4. Here also, there is an indication of a non-switchable polarization pointing downwards. Using the slope of the Jsc-Pr plot, the screening efficiency has been extracted and will be further discussed in the comparison part (table 5.2).

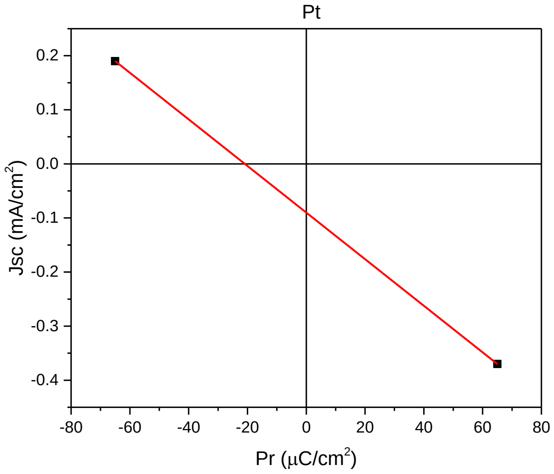

Figure 5.7. Photocurrent (Jsc) as a function of the measured remanent polarization (Pr) in Pt/PZT/SRO based capacitor device in both up and down polarization (after pre-poling under ±4V).

5.3 LSMO/PZT with Pt or ITO top electrodes

In this section effect of Pt and ITO top electrodes with the LSMO bottom electrode is evaluated on ferroelectric and photovoltaic properties. The capacitors with top Pt and top ITO electrodes have also been patterned on the same PZT/LSMO sample.

5.3.1 Ferroelectric measurements

Figure 5.8 shows the ferroelectric hysteresis loop of Pt, ITO/PZT/LSMO based capacitor devices with 100x100 μm^2 (Pt) and 30x30 μm^2 (ITO) lateral size. The Pt-based device shows a symmetric loop with Pr and Vc values of ±60 μC/cm^2 and ±2.4V. In Figure 5.7 (b), the ITO device shows a similar hysteresis loop as the ITO/PZT/SRO device. The ITO current loop also indicates a significant leakage for positive applied voltage and a positive shift of 0.7V for Vc.

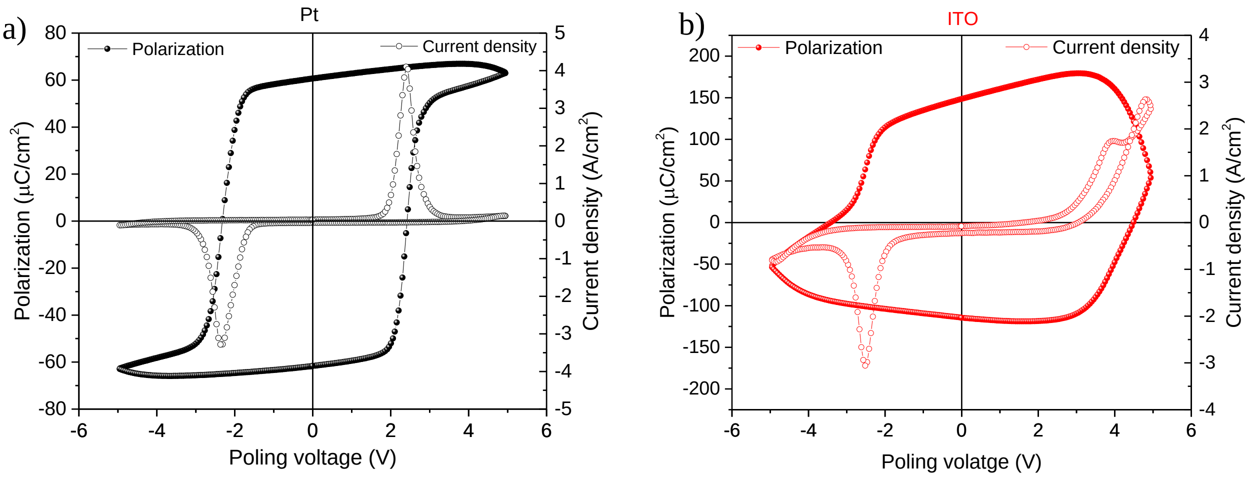

Figure 5.8. Ferroelectric hysteresis loop for a) Pt and b) ITO PZT/LSMO devices.

Ferroelectric measurements under UV illumination

Under illumination at 365nm (at a driving current of 350 mA of the diode), the Pt/PZT/LSMO device shows changes in Pr and Vc (see Figure 5.9 a), which are more visible in the PUND loop (see Figure 5.9 b).

Under illumination, the dynamic hysteresis loop is shifted to the negative side (left) in Figure 5.9 (a), and the PUND loop is moved to the positive side (right) in Figure 5.9 (b). Note that for both measurement methods, the loop has been first measured in dark condition, then the UV illumination has been switched on and the loop has been measured again. However, while DHM measurement ends with a positive applied voltage, PUND measurement ends with a negative applied voltage. The sample was thus in a P down polarization state before shining light and measuring the DHM loop, while the sample was in a P up polarization state before shining light and measuring the PUND loop. This difference in initial P state could explain why the photoinduced shift of the loop is in opposite direction in both cases. Similar results have been previously reported and attributed to the trapping of photoinduced charge carriers near the film/electrode interfaces in order to compensate the depolarizing field [109,110]. Here, in P down state (after DHM loop in dark), photoinduced charges will migrate along the up depolarizing field, inducing a down built-in field. An increased negative applied voltage will then be required to compensate for this built-in field, as it is indeed evidenced on the shifted DHM loop under illumination in Figure 5.9 (a). In P up state, however (after the PUND loop in dark), photoinduced charges will migrate along the down depolarizing field, inducing an up built-in field. The increased positive applied voltage will be required to compensate for this built-in field, as it is indeed evidenced on the shifted PUND loop under illumination in Figure 5.9 (b). When applying voltage pulses under illumination, the trapped charges can be released so the maximum shift should be observed for the first pulses under UV. This is maybe why a shift is only seen for the negative branch of the DHM loop, and why the shift is bigger for the positive branch of the PUND loop.

Regarding the polarization values, on the DHM loop, more leakage current is measured under light, as a result of photoconductivity, inducing an apparent increase of polarization under the light. In the PUND loop, this is also the case for the positive branch where the compensation of non-ferroelectric current is not perfect. In the negative branch, where there is no leakage contribution, no change in polarization value is observed under the light. Overall, the effect of light on the polarization values is thus difficult to single out due to leakage current contribution.

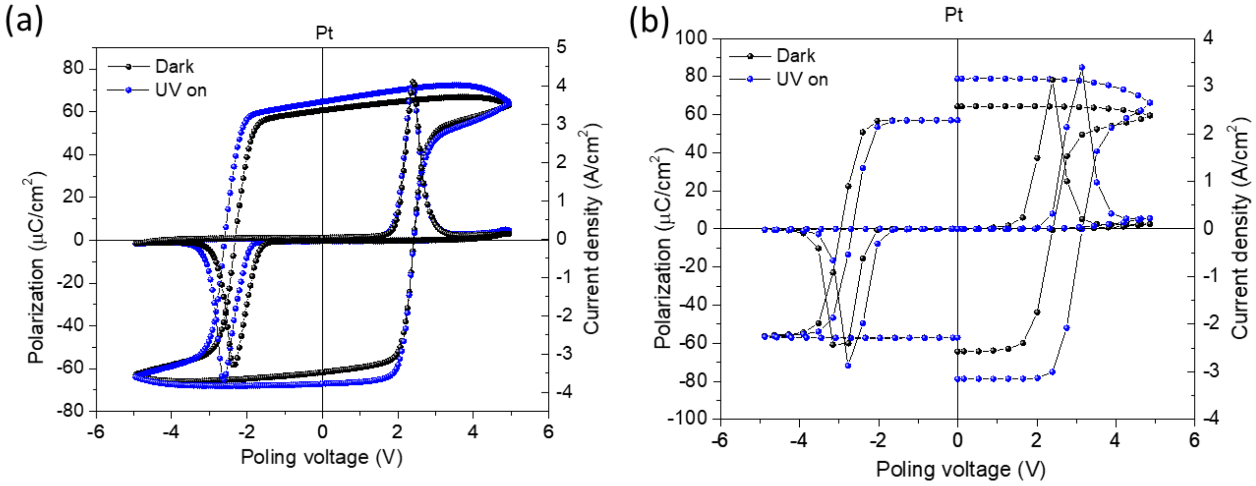

Figure 5.9. a) Ferroelectric hysteresis loop and b) PUND loop for Pt/PZT/LSMO in dark and under illumination at 365nm wavelength.

5.3.2 Photovoltaic measurements

I-V measurement

In Figure 5.10 (a), for Pt top electrode, the Jsc value is slightly higher in absolute value for the P_{down} state (-0.22 mA/cm^2) in comparison to the P_{up} state (0.19 mA/cm^2) and the Voc values show the opposite trend with a slightly higher value for the P_{up} state (-0.66V) than the P_{down} state (0.51V). In the case of ITO (see Figure 5.10 b), Jsc and Voc values are (0.55 mA/cm^2, -1V) and (-0.13 mA/cm^2, 0.2V) for up and down polarization states. The Jsc and Voc values are thus higher in absolute value in the case of polarization up state. These differences between Pt and ITO will be further discussed in the last part.

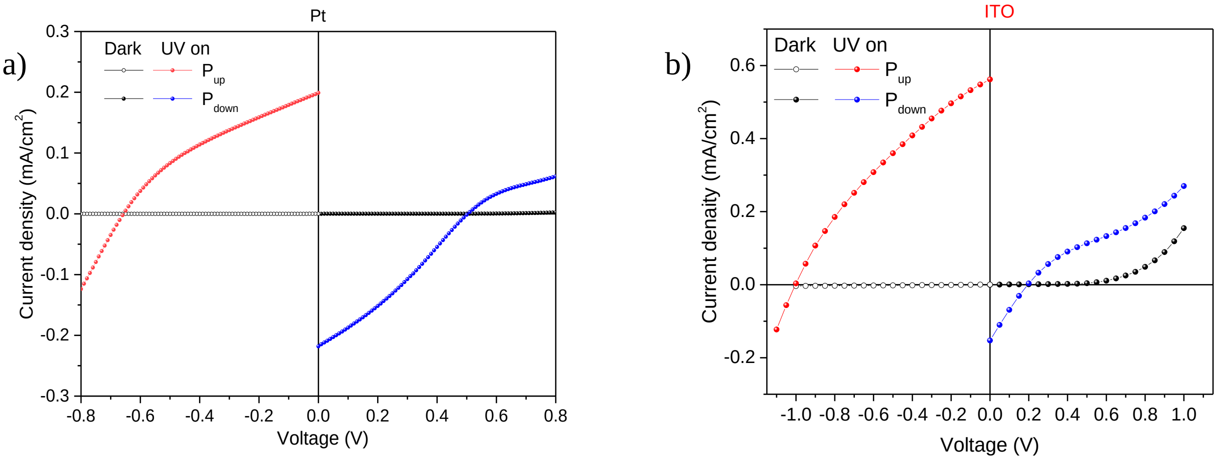

Figure 5.10. J-V measurement in up and down polarization state for a) Pt and b) ITO top electrode on PZT/LSMO composition under dark and UV illumination.

Effect of intensity of diode

The photocurrent was measured, for Pt top electrode, in the up (shades of red) and down (shades of blue) polarization state at different increasing intensity of diode currents ranging from 100 mA to 700 mA at 365nm wavelength (see Figure 5.11 a). Jsc and Voc values obtained from Figure 5.11 (a) were plotted as a function of the diode current intensities in Figure 5.11 (b-c). Jsc values increase linearly with increasing current intensity of the diode due to an increment in the generation of e-h pairs producing higher photocurrent, in agreement with the results obtained in chapter 3 also showing a linear increase of the photocurrent as function of the fluence.

Voc values do not depend on the diode intensity and show a saturation effect, already for diode intensity of 100 mA. This is different than the results obtained in chapter 3 where saturation of Voc was observed for diode intensities above 450 mA. This difference could be attributed to the fact that the diode was positioned closer to the sample in these measurements (chapter 5) than in the previous intensity studies (chapter 3), resulting in a higher incident power possibly reaching probably already the high intensity regime with saturation of Voc.

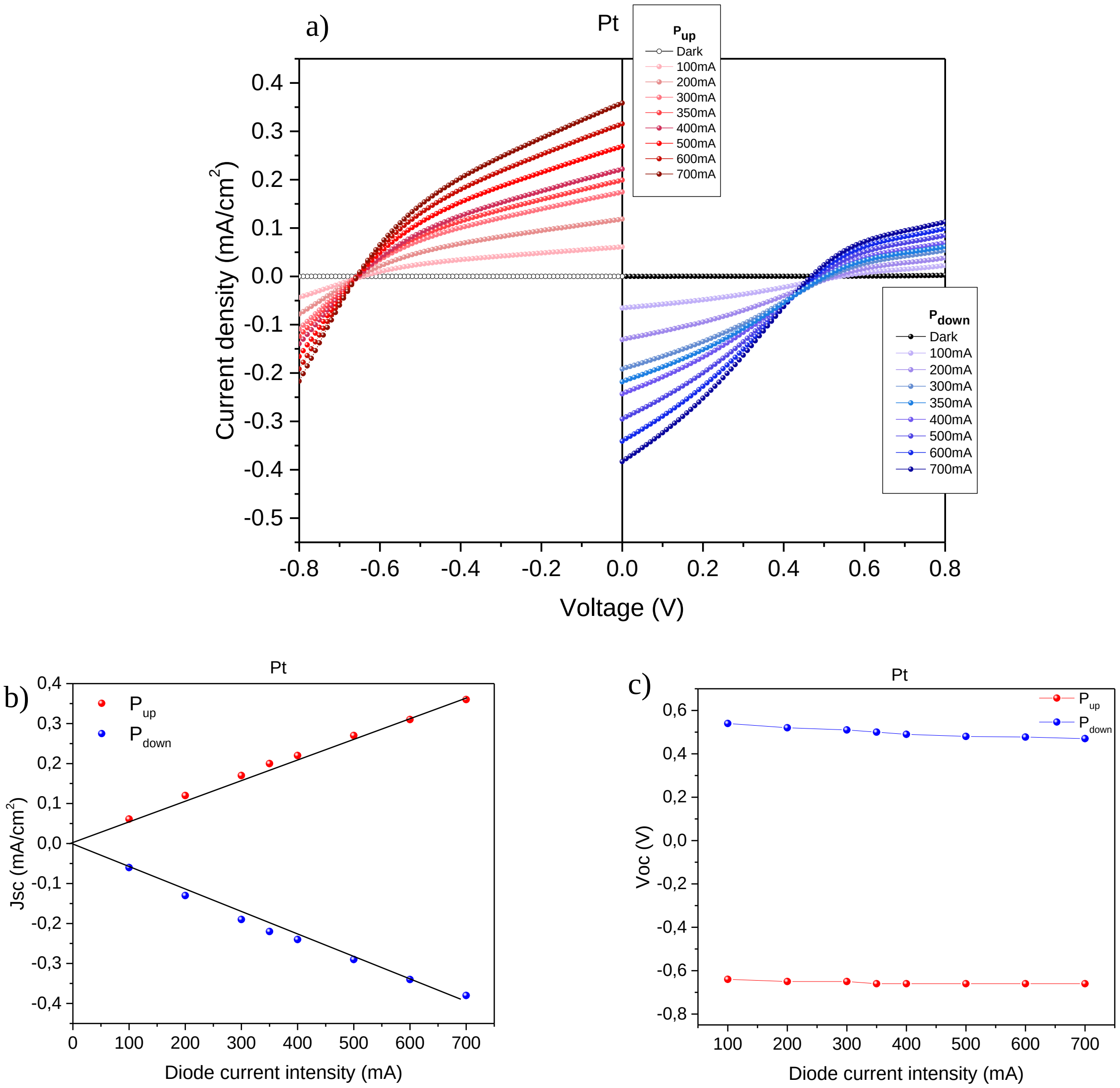

Figure 5.11. a) Photocurrent density for Pt/PZT/LSMO device measured at different driving current intensities of 365 nm UV LED, b) Jsc, and c) Voc as a function of diode current intensity in up and down polarization state.

I-T measurement

Time-dependent photocurrents were measured for Pt, ITO/PZT/LSMO devices in the up and down polarization state. The Jsc values are similar to the J(V) measurements. In the case of Pt, Jsc values are 0.19 mA/cm^2 and -0.24 mA/cm^2 in Figure 5.12 (a). For ITO, Jsc values are 0.55 mA/cm^2 and -0.13 mA/cm^2 in Figure 5.12 (b). The Jsc measurements for intermediate states close to switching were also performed for Pt device. The Pt-based device shows a slightly transient behavior, whereas the ITO-based device shows steady photocurrent. Note that the poling procedure is done following the protocol mentioned in chapter 4.

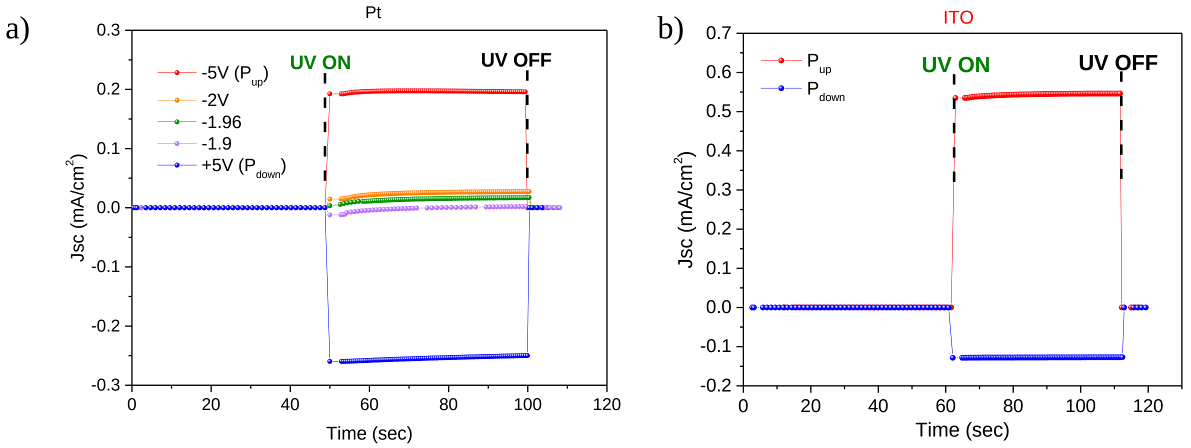

Figure 5.12. J-t measurement in up and down polarization state for a) Pt and b) ITO top electrode on PZT/LSMO composition. Measurements were also performed in some intermediate states for Pt device.

5.3.3 Jsc-Pr relation

To quantitatively study the relationship between Pr and Jsc, Jsc values are plotted against Pr. Note that the Jsc and Pr values are extracted using the same protocol as in chapter-4 for the Pt device. As seen for SRO/PZT/ITO device, due to the strong leakage for positive voltage for the LSMO/PZT/ITO device, it was not possible to extract with confidence Pr values and to plot the Jsc-Pr dependence for this device. The Pt-based device shows similar results as Pt/PZT/SRO device. There is also an indication of non-switchable polarization pointing downward in Figure 5.13. Using the slope of the Jsc-Pr plot, the screening efficiency was obtained (see table 5.2).

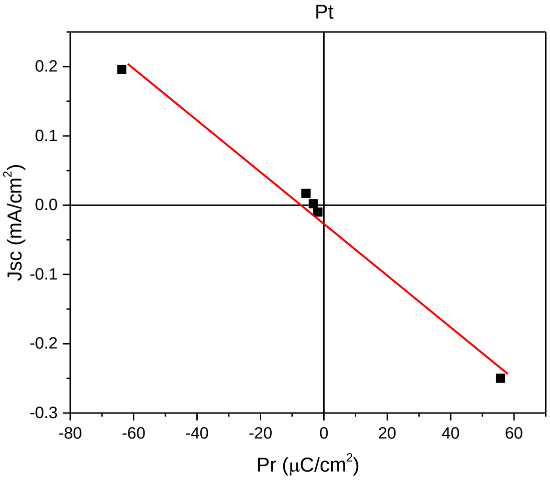

Figure 5.13. Linear dependence of photocurrent (Jsc) with the measured remanent polarization (Pr) in Pt/PZT/LSMO based capacitor device from the measurements in figure 5.12.

5.4 STO top buffer layer

In this section, a 1nm thick STO buffer layer is inserted at the interface between PZT and the electrode. The purpose is to study its effect on the screening of the PZT ferroelectric polarization which should be less efficient. Note that a 2 nm STO buffer layer was also put between PZT and top electrode, but no ferroelectric behavior was observed (only very resistive properties). The data presented here are for a SRO/PZT/STO(1 nm) sample with Pt top electrode. Preliminary results obtained on SRO/STO(1 nm)/SRO/PZT with Pt and ITO top electrodes are shown in annex.

5.4.1 Ferroelectric measurements

Figure 5.14 shows ferroelectric hysteresis loop measured up to 5V for the Pt/STO(1nm)/PZT/SRO device and gives high remanent polarization values similar to Pt/PZT/SRO device. The ±Vc values are obtained as +2.8V and -3V, and the ±Pr values are ±77 μC/cm^2 after leakage removal (PUND method).

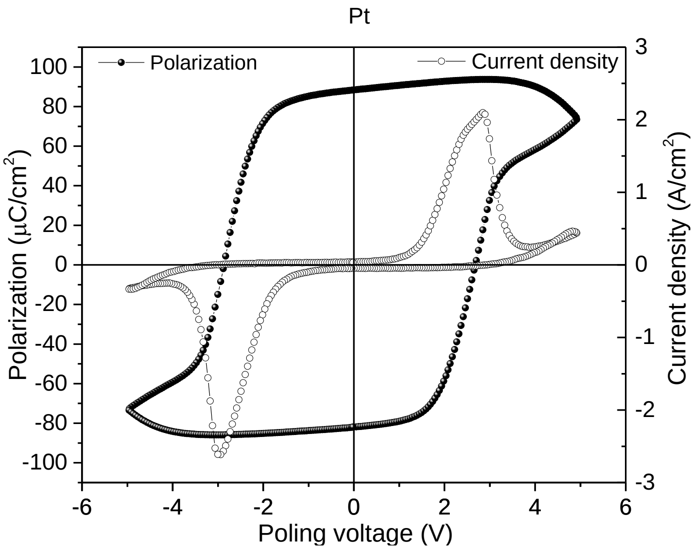

Figure 5.14. Ferroelectric hysteresis loop for Pt/STO(1nm)/PZT/SRO device.

5.4.2 Photovoltaic measurements

To see the effect of buffer layer at top interface, photovoltaic measurements were performed on Pt/STO(1nm)PZT/SRO device. J-V and J-t measurement were obtained in up and down polarization after poling by ±5V in Figure 5.15 (a-b). The Jsc and Voc values extracted from J-V curves are (-0.7 mA/cm^2, 1.3V) for the P_{down} state in comparison to (0.6 mA/cm^2, -1.4V) for the P_{up} state. These Jsc values are consistent with the J-t measurements, giving -0.6 mA/cm^2 and 0.5 mA/cm^2 in the up and down polarization state. The Pt/STO(1nm)PZT/SRO device presents thus similar trend as Pt/PZT/SRO in chapter 3.

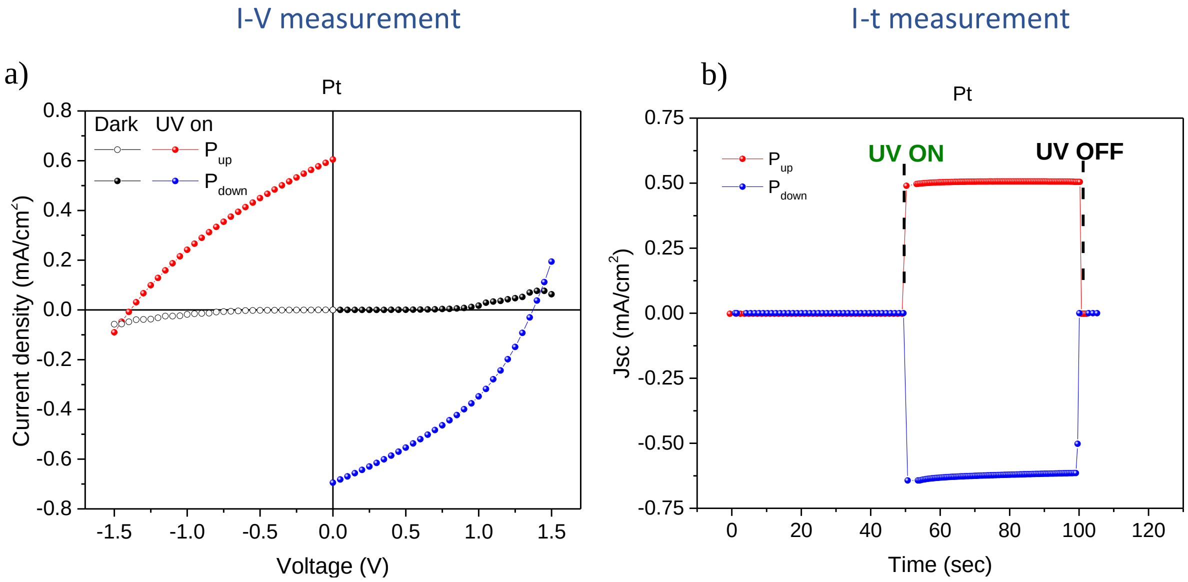

Figure 5.15. a) J-V measurement and b) J-t measurement in up and down polarization state for Pt/STO(1nm)PZT/SRO device under dark and UV illumination.

5.4.3 Jsc-Pr

Jsc as a function of Pr curve for Pt/STO(1nm)/PZT/SRO can be seen in Figure 5.16. These results are also consistent with previously mentioned results on Pt/PZT/SRO stack. There is a small non-switchable polarization pointing downward. The slope of Jsc-Pr curve is used to calculate the screening efficiency.

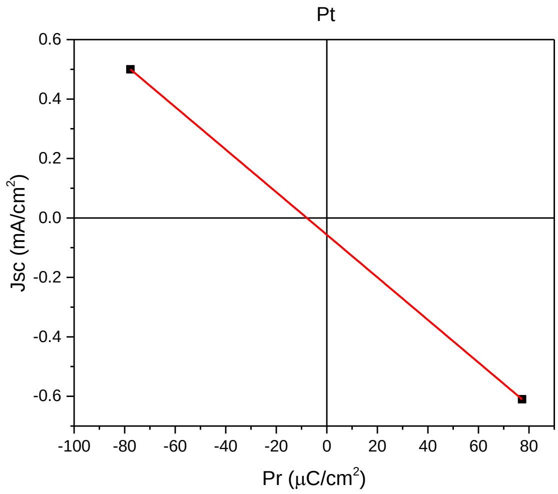

Figure 5.16. Extrapolated linear dependence of photocurrent (Jsc) with the measured remanent polarization (Pr) in Pt/STO(1nm)/PZT/SRO based capacitor device.

5.5 Summary: Comparison

5.5.1 Leakage

Bottom interfaces (SRO/PZT and LSMO/PZT) as well as top interfaces (PZT/Pt, PZT/ITO, and PZT/STO/Pt) have different potential barriers, and this necessarily affect the transport of current through the devices. The work function Φ_m and barrier height Φ_0 for all interfaces are listed in table 5.1. The electron affinity of PZT is χ =3.5 eV [111]. The barrier height is taken as $\Phi_0 = \Phi_m - \chi$.

Electrode	Work function (eV)	Stack	Barrier height $\phi_\circ$ (eV)
Pt	5.3 [40]	Pt/PZT	1.8
ITO	4.5 [112]	ITO/PZT	1
SRO	5 [40]	PZT/SRO	1.5
LSMO	4.8 [113]	PZT/LSMO	1.3

Table 5.1. List of work functions and barrier heights used in the thesis.

This is the order expected going from lowest to highest barrier height: PZT/ITO < LSMO/PZT < SRO/PZT < PZT/Pt. Note that experimentally the barrier heights are much smaller than the values obtained by the calculation due to the presence of interface states which pin Fermi level. From previous analysis of transport mechanism through PZT films grown in our group, Pt/PZT, PZT/SRO and ITO/PZT interfaces exhibit experimental barrier heights of 0.72 eV, 0.38 eV and 0.23 eV, respectively [114]. However, these barrier heights can be strongly affected by the quality of the interfaces and may vary from one sample to another one, especially for different PZT targets and electrode deposition techniques.

From polarization loops, a low leakage is measured in SRO/PZT/Pt device and the symmetry in current between both voltage polarities hints towards relatively high and similar potential barriers at both interfaces (figure 5.3 a). Note that for the LSMO/PZT/Pt device, symmetric curve is also observed while both barriers are expected to be more different than for the SRO/PZT/Pt case.

For SRO/PZT/ITO device, the barrier heights at top and bottom are expected to be more asymmetric than for the SRO/PZT/Pt device. The lowest barrier height is at the top and much current is measured for positive applied voltage (figure 5.3 b). This points towards a p-type PZT in which the blocking Schottky contact is the top one when positive voltage is applied to it. PZT can act as a n-type semiconductor when majority carriers are electrons (which could be the case when oxygen vacancies play a major role in the conduction). Here, PZT seems rather to act as a p-type semiconductor and other type of defects (probably Pb defects) could explain this behavior. In the literature, both cases are reported.

The leakage behavior in LSMO/PZT/ITO device (figure 5.8 b) is similar to the SRO/PZT/ITO device with much current for positive applied voltage due to the lowest top barrier.

Due to the very small thickness of STO top buffer (1 nm) and to the surface roughness of 2 nm, it could be that the STO buffer (used in the SRO/PZT/STO/Pt device) is not continuous, which would explain why the results are comparable to the SRO/PZT/Pt device (symmetric current transport and similar PV properties). More work on the growth to reduce the roughness and a series of samples with different thicknesses of STO buffer will be required to continue this study.

Finally, to get experimental values of barrier heights in our devices, transport measurements should be performed as a function of applied bias and temperature, to define the transport mechanism and Schottky barrier height of each interface in these particular devices.

5.5.2 J-Pr

Five different devices with Pt, ITO top, SRO, LSMO bottom electrodes and top STO buffer layer are compared in terms of ferroelectric, photovoltaic, dielectric parameters such as Pr, (Jsc, Voc), photocurrent switchability (S), conductivity (σ), relative permittivity (Ɛr), extracted non-switchable polarization (P_{NS}) and fraction of unscreened polarization α, as listed in table 5.2. The conductivity (σ) was measured from the slope of the I-V measurements under light. The permittivity (Ɛ) is extracted from capacitance values measured under light. The screening efficiency is extracted using the protocol mentioned in chapter 4. Photocurrent switchability is obtained using the formula below (as mentioned in chapter 1).

$$S = \left| \frac{Jup - Jdown}{2\max\left(|Jup|, |Jdown|\right)} \right|$$

The P_{NS} values were obtained using Jsc-Pr curves.

Parameter		Pt/PZT/SRO (4Vpoling)	ITO/PZT/SRO (5V poling)	Pt/PZT/LSMO (5V poling)	ITO/PZT/LSMO (5V poling)	Pt/STO/PZT/SRO (5V poling)
Device size (μm^2)		100x100	100x100	100x100	30x30	200x200
Pr (μC/cm^2)	P_{up}	-65	-	-63	-	-77.6
	P_{down}	65	-	55	-	77.2
Jsc(mA/cm^2)	P_{up}	0.19	0.39	0.19	0.55	0.5
	P_{down}	-0.37	-0.24	-0.24	-0.13	-0.6
Voc (V)	P_{up}	-0.84	-1.5	-0.66	-1	-1.4
	P_{down}	0.76	0.48	0.51	0.2	1.3
S		76%	81%	90%	62 %	92%
σ (nS cm^{-1})	P_{up}	2.2	2.7	2.5	8.9	4.2
	P_{down}	4.6	6.3	4.3	5.5	3.9
Ɛr		184	-	131	271	104
ΔVc (V)		0.15	0.95	0	0.7	-0.1
~P_{NS} (μC/cm2)		20	-	11	-	11
α		0.02	-	0.012	-	0.016

Table 5.2. List of parameters Pr, Jsc, Voc, switchability (S), photoconductivity (σ), relative permittivity (Ɛr), shift of coercive voltage (ΔVc), extracted non-switchable polarization (P_{NS}) and fraction of unscreened polarization (α) for Pt, ITO/PZT/SRO, Pt, ITO/PZT/LSMO and Pt/STO(1nm)/PZT/SRO capacitor devices.

For each P_r state, corresponding ε and σ values have thus been considered and the J_S ε /σ product has been plotted as a function of P_r in Figure 5.17.

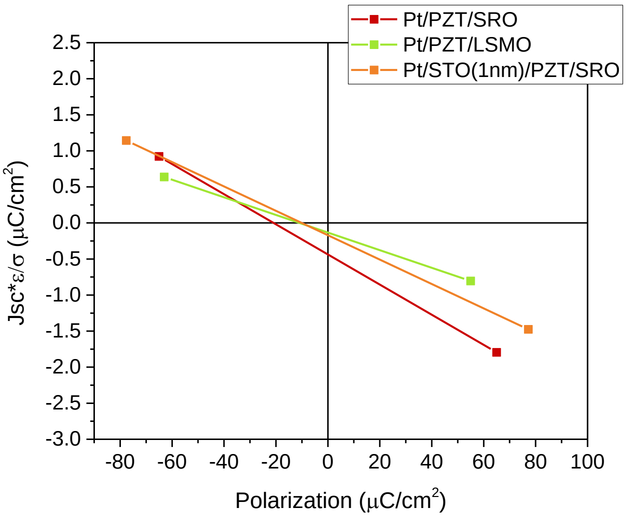

Figure 5.17 J_S ε /σ values plotted as function of P_r, using the Jsc-Pr data of Pt/PZT/SRO, Pt/PZT/LSMO, and Pt/STO(1nm)/PZT/SRO devices.

Photocurrent switchability

The averaged values of Jsc and Voc (for up and down states) are in the same range for all samples. While for all samples Pt devices, remanent values for up and down polarization are quite similar, the photocurrent switchability is the lowest for the SRO/PZT/Pt device (76%) and the highest for SRO/PZT/STO/Pt (92%). No correlation can be seen between the photocurrent switchability and the shift of the polarization loop (the SRO/PZT/ITO device shows a high switchability of 87% while the loop is strongly shifted). The shift of the loop is stronger for ITO top electrode and could be related to the trapping of charged defects at the top interface during the electrode deposition by sputtering (annealing tests could be performed on the sample to investigate that). In summary, as reported in chapter 4, the polarization loop does not provide any indication about the expected photocurrent response and switchability of the sample.

Fraction of unscreened polarization

The fraction of unscreened polarization is between 1.2% and 2% for all the Pt devices. Note that the low apparent dielectric constant for the STO/PZT stack stems from the series capacitor formed by STO and PZT layers, with a very low value for ultrathin STO, and does not reflect the value for PZT alone. If we consider the ε value taken as the one measured for PZT in the other PZT/SRO sample, the fraction of unscreened polarization increases to 2% but is still in the same range. The ultrathin STO (1 nm) barrier is probably polarized by the PZT and does not affect the screening efficiency in the device. As SRO is a better conductor than LSMO, one would expect a better screening efficiency for SRO/PZT/Pt than for LSMO/PZT/Pt, but this is not observed experimentally (2% of unscreened polarization vs. 1.2%). The use of LSMO or SRO top electrodes to build a full oxide capacitor would be interesting to investigate, or of other conducting electrode in order to find one that would affect more the screening of polarization.

Equivalent non switchable polarization

As seen in figure 5.17, positive P_{NS} values (down polarization) are extracted for all Pt devices: SRO/PZT/Pt, LSMO/PZT/Pt and SRO/PZT/STO/Pt devices (the P_{NS} value of Pt/PZT/SRO device in chapter 4 was 12µC/cm²) and account for the highest photocurrent achieved in P down state while Pr value in this state is not higher than for the P up state. Non switchable down polarization would result indeed in a up internal electric field that would favor negative photocurrent as measured for these devices. For SRO/PZT/ITO and LSMO/PZT/ITO devices, even if the study of Jsc-Pr dependence was not possible, the highest photocurrent achieved in the P up state could indicate the presence of a down internal electric field.

For all Pt devices, P_{NS} values are not bigger than 20 µC/cm², which is reasonable. Adding Pr and P_{NS} does not give polarization value higher than 90 µC/cm².

Chapter-6

Conclusion and perspectives

The ferroelectric materials have the ability to switch photovoltaic (PV) properties to achieve 100% switchability. This switchability can be affected by intrinsic parameters such as polarization and extrinsic parameters such as electrodes/interfaces and defects. This work focuses on the investigation of FE thin films, not only to achieve switchable PV properties but also to better understand their ferroelectric response, which indeed is beneficial for future photo-ferroelectric memory devices.

The first part of the thesis presents the state-of-the-art of ferroelectric materials in all aspects related to the photovoltaic effect in ferroelectrics, the different PV mechanisms playing a role in the generation of photocurrent, and factors that affect the switchable PV parameters (Jsc, Voc). The second part provides a general introduction of techniques used for the epitaxial growth by PLD of oxide thin films, and for patterning of PZT(20/80) layers (100-120nm thickness) into capacitor devices with different top and bottom electrodes (Pt, ITO, or Pt/STO as top, and SRO, LSMO or STO/SRO as bottom). Techniques and experimental conditions are also presented for the analysis of the ferroelectric, dielectric, and photovoltaic properties using two UV sources (UV LED 365nm) and Xe lamp (300-400nm wavelength range).

The third part focuses on the study of the Pt/PZT (20/80) (100 nm)/SRO device. The surface topography and crystal quality of the PZT 20/80 film are both excellent. Ferroelectric behavior is demonstrated in the device, which has symmetric and high remanent polarization values of 70 µC/cm2. Open and short circuit conditions for both up and down polarization states in dark display good polarization retention. According to the C(V) measurements, the 20/80 PZT has a conventional butterfly loop with a dielectric constant of approximately 200 at the ferroelectric switching. The ferroelectric polarization loop is not affected by UV illumination above the PZT bandgap, but the dielectric constant is observed to be affected by light when measured at low frequency (1 kHz), indicating that slow charged carriers are probably migrating and trapped under illumination. The device's photovoltaic properties have been thoroughly investigated and evaluated: (i) First, by switching the polarization between the down and up polarization states, it is possible to achieve switchability of the short-circuit current Jsc and the open-circuit voltage Voc (switchability of 87% for Jsc). (ii) Jsc and photoconductivity are found to rise linearly with the UV fluence in both polarization states, while Voc reaches saturation when the UV fluence is high enough to cause the photoconductivity to become significantly greater than the dark conductivity. According to the literature, this relationship between PV characteristics and light fluence is consistent with what is expected for a traditional FE material with good insulating properties. (iii) With a bandgap of 3.3 eV, the wavelength dependence of the measured photocurrent is consistent with the optical absorption of PZT 20/80. At photon energies below the bandgap, no measurable photocurrent can be obtained. (iv) Under illumination, the time evolution of photocurrent demonstrates a very stable behavior in both the up and down polarization states. It is possible that the photocurrent exhibits more prominent transient behavior in intermediate states with low polarization values because the depolarizing field, which drives the photocurrent for both up and down polarization states is virtually zero in these states. If charged carriers become trapped at interfaces and the polarization values are modified, the photocurrent in the short-circuit situation and disordered polarization state can be primarily affected by the potential barrier for mobile carriers and its evolution over time at both interfaces.

The fourth part of this thesis presents a quantitative study of the relationship between remanent polarization and short-circuit photocurrent in a Pt/PZT (100nm)/SRO device for electrically written and stable intermediate remanent polarization states. A linear relationship is measured between photocurrent and remanent polarization, and quantitative examination of these results revealed the presence of a pinned component of polarization in the layer, which impacts photocurrent switchability. While the linear relationship cannot be used to determine the source of the photocurrent (which might be bulk PV or driven by depolarizing field), the established method can be used to disclose unswitchable polarization in a ferroelectric layer. Pinned polarization could be linked to defects, particularly at electrode interfaces. While the traditional ferroelectric loop only gives a limited picture of the switchable polarization, this study provides essential insights into ferroelectric behavior in all sorts of ferroelectric layers and the polarization dependence of the photocurrent could serve as an efficient tool to characterize the quality of any ferroelectric film integrated in capacitor.

The fifth part of this work investigates different types of electrode materials in order to find out how they can affect the part of unswitchable polarization, and if different screening efficiencies can be achieved and quantified. For this purpose, devices with asymmetric interfaces were fabricated namely (Pt, ITO/PZT) on SRO, (Pt, ITO/PZT) on LSMO, and Pt/STO/PZT/SRO. All devices present photocurrent switchability above 60%. The main message is that the classical ferroelectric polarization loop does not provide any indication about the expected photocurrent response and switchability of the sample. Only by measuring quantitatively the polarization dependence of the photocurrent can we understand the PV properties of a FE device.

The devices with Pt top electrodes were analyzed using the mentioned protocol in chapter 4. For the Pt-based devices, the ferroelectric loop is more or less symmetric with negligible leakage, except for the top STO buffer device, for which leakage contribution to polarization could be removed using our voltage pulse protocol. These results for the Pt devices are consistent with the results presented in chapter 4 on another Pt/PZT/SRO device (using another PZT target). The average values of Jsc and Voc are in the same range. The highest switchability of photocurrent was measured in the device with the top STO buffer layer. The part of unscreened polarization extracted in these devices is in the range of 1.2% to 2%. For all Pt devices, a component of non-switchable polarization is evidenced, inducing an up electric field (similar to the study in chapter 4) and explaining why the photocurrent is not 100% switchable, and why the current is higher in the down polarization state. One should emphasize here that the non-switchable polarization is not related to imprint-induced fast back switching of very mobile domains, since the hysteresis loop for the remanent polarization (Pr) exhibits similar values for both poling directions. It can then be referred to as a pinned polarization which is not probed by the ferroelectric hysteresis measurements but revealed by the photocurrent measurements. Note that the origin of this pinned part of polarization is beyond the scope of this study and would deserve more investigation. It could be related to an inhomogeneous distribution of charged defects within the film and/or to the asymmetry between the potential barriers for mobile charge carriers at bottom and top interfaces.

In the case of ITO-based devices, the ferroelectric loop is shifted towards positive voltage, indicating an imprint field in the up direction. However, the photocurrent switchability can reach 87% in SRO/PZT/ITO device. Higher photocurrent was achieved in the up polarization state for both ITO devices (in opposite direction compared to the Pt devices results) and this asymmetry measured between the photocurrent in up and down polarization states does not seem to be related to the imprint field. The higher photocurrent in up state could be related to some contribution of Schottky-barrier effect, as the barrier at PZT/ITO interface is very different from the PZT/Pt one, from measurements performed with both devices on the same PZT film. It was not possible to extract precisely the Pr values due to the huge contribution of leakage at the switching even using the pulse protocol, preventing us from studying quantitatively the polarization dependence of the photocurrent in ITO devices.

Future work can be done on the optimization of the devices with the careful use of electrodes and heterostructures. For example, the use of LSMO or SRO top electrodes to build a full oxide capacitor would be interesting to investigate, as well as inserting different STO barriers, in order to measure its effect on the screening of polarization. More generally, the developed method can be used to reveal pinned polarization in ferroelectric layers, which is otherwise difficult to probe. It can thus be used to study and optimize the ferroelectric behavior in integrated ferroelectric layers. In this particular research field of PV in ferroelectrics, the results presented here provide a general approach to study and optimize the switchability of photocurrent, which could have far-reaching implications for future photo-ferroelectric memory applications.

Annex

Annex A) STO bottom buffer layer

Further work has to be done on the optimization of the growth on the bottom STO buffer layer and the structural characterization of the sample. Here, preliminary results on the STO buffer layer inserted at the bottom interface between PZT and SRO are presented. All the ferroelectric and photovoltaic measurements were carried out under the same conditions as chapter 5.

A.1) Surface and structural characterization

A.1.1) Atomic force microscopy

The surface morphology was analyzed by atomic force microscopy (AFM). The AFM measurements show a smooth surface for PZT/STO(1nm)/SRO on (001) STO substrate, as shown in Figure A.1.

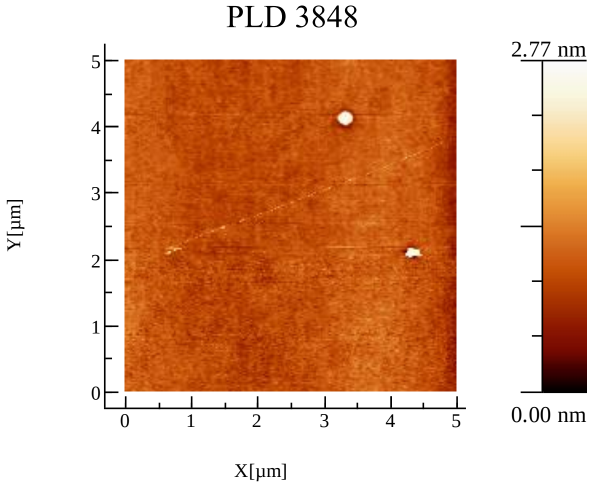

Figure A.1. AFM topography image of PZT/STO(1nm)/SRO/STO.

A.1.2) X-ray diffraction

High-quality epitaxial PZT films that have been obtained can be seen in θ-2θ scans, showing only the (00l) family of Bragg peaks for PZT, as well as the bottom electrode layer SRO and the STO substrate (Figure A.2). The full-width half-maximum of PZT (FWHW) is 0.08° in the rocking curve. The c lattice parameter of PZT is 0.412 nm.

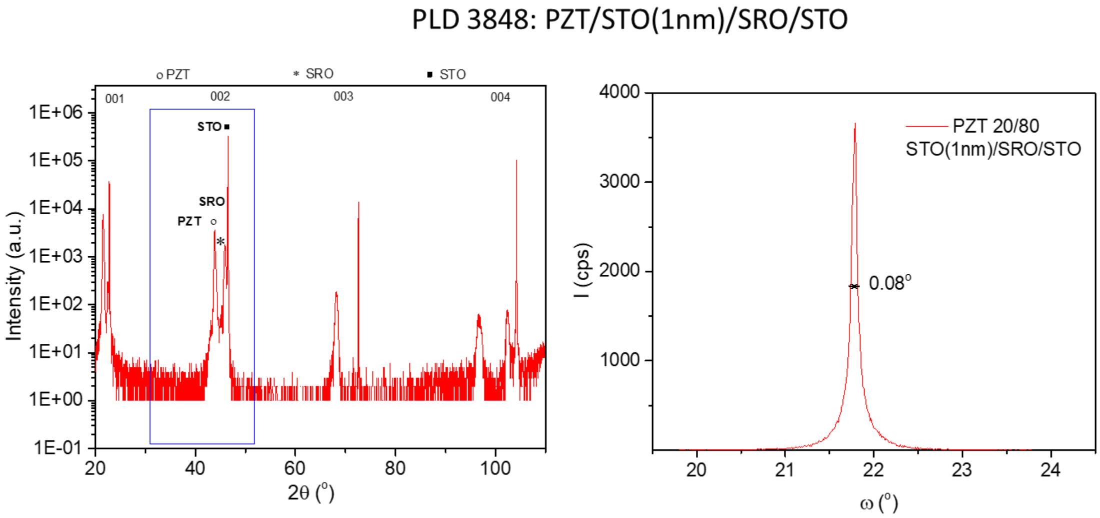

Figure A.2. θ-2θ XRD curve and corresponding rocking curve around the (002) PZT Bragg peak for PZT/STO(1nm)/SRO/STO.

A.2) Ferroelectric measurements

Ferroelectric hysteresis loop for Pt, ITO/PZT/STO(1nm)/SRO device is presented in Figure A.3 (a-b). Both the devices indicated a huge shift in the hysteresis loop to the negative side (left) (ΔVc= -2.45 V for Pt and -1,8 V for ITO), which indicates the presence of a big imprint field pointing downward. The switching of polarization from up to down happens for the negative applied voltage for ITO device and starts also before applying positive voltage for the Pt device, preventing from stabilizing a P up state in both devices. For both devices, a huge leakage current is measured for the negative applied voltage.

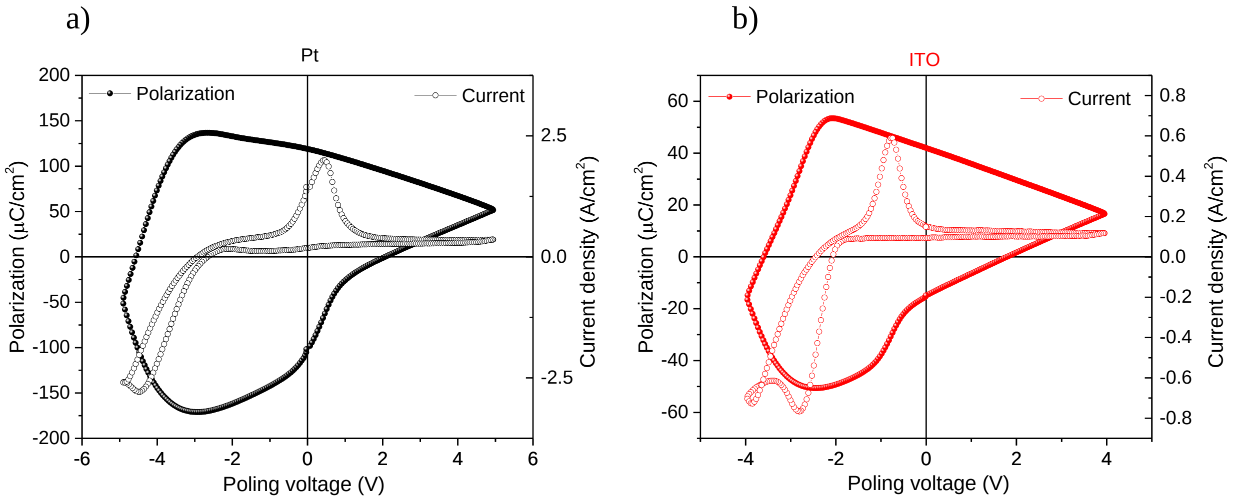

Figure A.3. Ferroelectric hysteresis loop for top electrode a) Pt and b) ITO on PZT/STO(1nm)/SRO device.

A.3) Photovoltaic measurements

I-V measurement

The photovoltaic properties of Pt, ITO/PZT/STO(1nm)/SRO devices were measured to see the effect of the 1nm STO buffer layer at the bottom interface. In both the devices Jsc and Voc are not switchable which is not surprising because the polarization cannot be switched by poling. In Pt-based device Jsc is negative and Voc is positive for both poling (+5V and -5V) in Figure A.4 (a-b). In contrast, the ITO-based device has positive Jsc and negative Voc for both poling (+4V and -4V). Surprisingly, the two devices exhibit different signs of Jsc and Voc, while the shift in the P-V loops is in the same direction. The list of all the Jsc and Voc values are listed for the Pt and ITO-based devices in table A.1. Note that the photocurrent densities are much lower than the values measured for the other devices in chapter 5. Due to the big shift of the P-V loop, it was impossible to access the value of remanent polarization after both poling which prevented us from investigating in more detail the PV properties of this device.

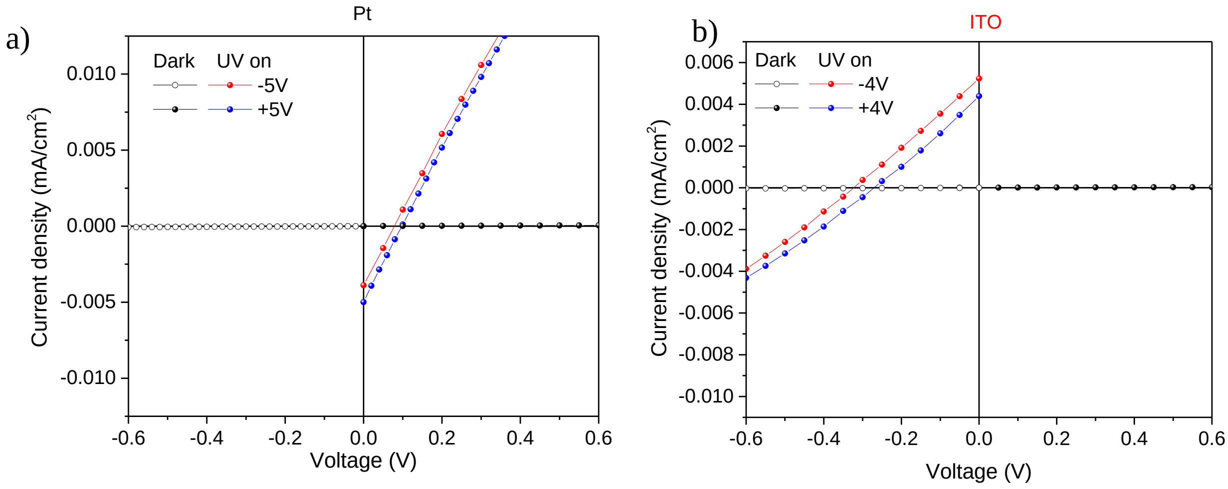

Figure A.4. J-V measurement in up and down polarization state for a) Pt and b) ITO on PZT/STO(1nm)/SRO device under dark and UV illumination.

Stack	**Jsc (µA/cm^2)**		**Voc (V)**	
	P_{up}	**P_{down}**	**P_{up}**	**P_{down}**
Pt/PZT/STO(1nm)/SRO	-5	5	0.08	0.1
ITO/PZT/STO(1nm)/SRO	-4	4	-0.33	-0.28

Table A.1 List of Jsc and Voc values for the Pt and ITO on PZT/STO(1nm)/SRO stacks.

I-t measurement

The time-dependent photocurrent measurement for Pt and ITO on PZT/STO(1nm)/SRO was carried out. The results are clearly similar to the J-V measurements above. In Pt-based device, Jsc values are -3.8 μA/cm2 and -4.5 μA/cm^2 for up and down polarization state in Figure A.5 (a). In ITO-based device, Jsc values are 4 μA/cm2 and 3.8 μA/cm^2 for up and down polarization state in Figure A.5 (b).

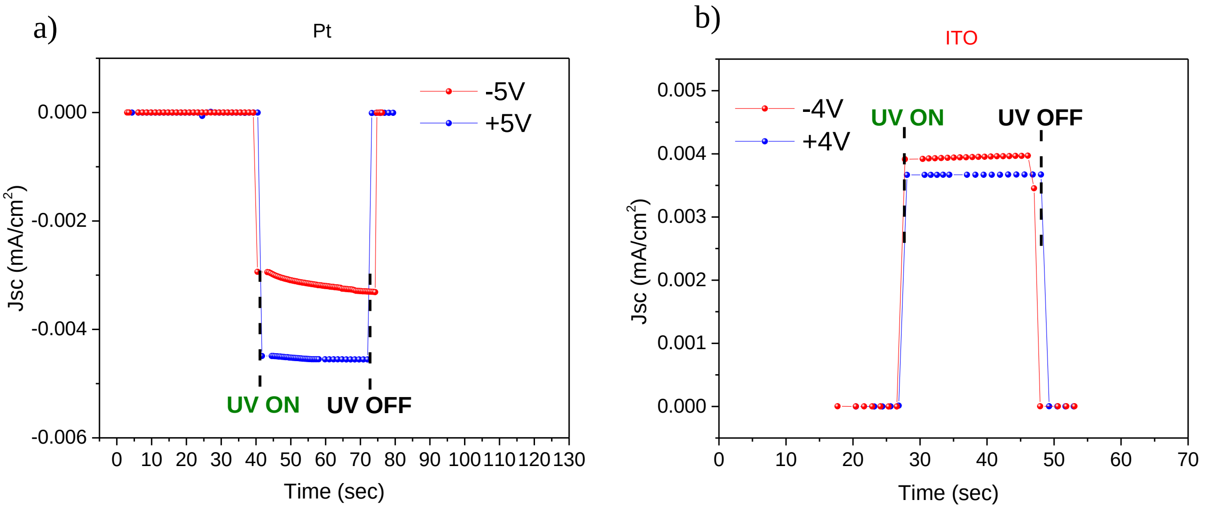

Figure A.5. J-t measurement after positive and negative poling for a) Pt and b) ITO on PZT/STO(1nm)/SRO device under dark and UV illumination.

Résumé en français

Propriétés photovoltaïques commutables dans des couches minces ferroélectriques de PZT

Les ferroélectriques (FE) sont généralement des matériaux ayant une constante diélectrique élevée, ce qui les rend idéaux pour des applications en tant que condensateurs. Ils montrent une commutation de polarisation spontanée, une phototension au-dessus de la bande interdite et des caractéristiques optiques qui peuvent être utilisées pour créer des dispositifs optoélectroniques de nouvelle génération [1]. L'objectif principal de cette thèse est d'étudier les propriétés photovoltaïques (PV) commutables des couches minces d'oxyde ferroélectrique (PZT) intégrées dans une géométrie condensateur. Dans ce travail, trois objectifs ont été visés. Tout d'abord, quantifier la relation entre la polarisation ferroélectrique et le photocourant, en outre, le comportement commutable et non commutable de la polarisation, la façon dont ils affectent la commutation du photocourant et la cause première de ce comportement sont discutés. Le deuxième objectif était d'étudier différents effets PV possibles impliqués dans les dispositifs FE, car l'un d'eux peut être la source dominante du photocourant. Puisque la commutation peut être affectée par des propriétés intrinsèques telles que la polarisation et des propriétés extrinsèques telles que les électrodes / interfaces et les défauts. Notre troisième objectif était d'étudier différentes interfaces avec différentes électrodes supérieures et inférieures ainsi que l'insertion d'une couche tampon isolante (hétérostructures).

Ce travail permet l'optimisation des films minces FE, non seulement pour obtenir des propriétés PV commutables, mais aussi pour comprendre leur réponse ferroélectrique qui est en effet bénéfique pour les futurs dispositifs de mémoires photoferroélectriques.

Ce travail de thèse se compose de 6 chapitres décrits ci-dessous :

Le premier chapitre comprend l'état de l'art des matériaux ferroélectriques dans tous les aspects liés à l'effet photovoltaïque dans les ferroélectriques, en mettant l'accent sur le PZT, les différents mécanismes photovoltaïques jouant un rôle dans la génération de photocourants et les facteurs qui affectent les paramètres photovoltaïques commutables (Jsc, Voc). La deuxième partie fournit une introduction générale des techniques utilisées pour la croissance épitaxiale, les couches minces $PbZr_{(1-x)}Ti_{(x)}O_3$ (PZT) ont été élaborées par croissance épitaxiale par la technique d'ablation laser pulsé (PLD), et pour la structuration des couches PZT (20/80) (100-120nm d'épaisseur) dans des dispositifs de type condensateurs avec différentes électrodes supérieures et inférieures (Pt, ITO ou Pt / STO en haut, et SRO, LSMO ou STO/SRO en bas). La cristallinité et la morphologie des films ont été analysées à l'aide de la diffraction des rayons

X (XRD) et de la microscopie à force atomique (AFM). Toutes les techniques et conditions expérimentales sont également présentées pour l'analyse des propriétés ferroélectriques, diélectriques et photovoltaïques à l'aide de deux sources UV (LED UV 365nm, et lampe Xe dans la gamme de longueurs d'onde 300-400nm).

La troisième partie se concentre sur l'étude du dispositif Pt/PZT (20/80) (100 nm)/SRO. La topographie de surface et la qualité cristalline du film PZT 20/80 sont toutes deux excellentes. Le comportement ferroélectrique est démontré dans le dispositif, la figure 1a montre le cycle d'hystérésis ferroélectrique typique avec des valeurs de polarisation rémanentes élevées de 70 μC / cm^2. Les deux états de polarisation rémanente présentent une bonne rétention en l'absence d'éclairement UV, à la fois en condition de circuit ouvert et en court-circuit. Selon les mesures C(V), le PZT 20/80 présente une courbe en papillon conventionnelle avec une constante diélectrique d'environ 200 au retournement de polarisation ferroélectrique. Le cycle de polarisation ferroélectrique n'est pas affecté par l'éclairement UV au-dessus de la bande interdite du PZT, mais la constante diélectrique est affectée par la lumière lorsqu'elle est mesurée à basse fréquence (1 kHz), ce qui indique que les porteurs chargés migrent probablement lentement et sont piégés sous éclairement. Les propriétés photovoltaïques du dispositif ont été soigneusement étudiées et évaluées: (i) Tout d'abord, en commutant la polarisation entre les états de polarisation vers le bas et vers le haut, il est possible d'obtenir la commutabilité du courant de court-circuit Jsc et de la tension en circuit ouvert Voc (la figure 1b montre une commutabilité de 87% pour Jsc). (ii) On constate que le photocourant en court-circuit Jsc et la photoconductivité augmentent linéairement avec la fluence UV dans les deux états de polarisation, tandis que Voc atteint la saturation lorsque la fluence UV est suffisamment élevée pour que la photoconductivité devienne significativement supérieure à la conductivité dans le noir. Selon la littérature, cette relation entre les caractéristiques PV et la fluence de la lumière est cohérente avec ce qui est attendu pour un matériau FE traditionnel avec de bonnes propriétés isolantes. iii) Avec une bande interdite de 3,3 eV, la dépendance mesurée du photocourant en fonction de la longueur d'onde est compatible avec l'absorption optique de PZT 20/80. À des énergies de photons inférieures à la bande interdite, aucun photocourant mesurable ne peut être obtenu. (iv) Sous éclairement, l'évolution temporelle du photocourant démontre un comportement très stable dans les états de polarisation haut et bas. Il est possible que le photocourant présente un comportement transitoire plus important dans les états intermédiaires avec de faibles valeurs de polarisation, car le champ dépolarisant, qui entraîne le photocourant pour les états de polarisation haut et bas, est très faible dans ces états. Une autre origine possible de cette dépendance temporelle du photocourant pourrait être liée au piégeage de porteurs chargés aux interfaces modifiant les valeurs de polarisation et affectant le photocourant en court-circuit et dans un état de polarisation désordonné – ce photocourant pouvant être principalement affecté par la barrière de potentiel et son évolution au fil du temps aux deux interfaces.

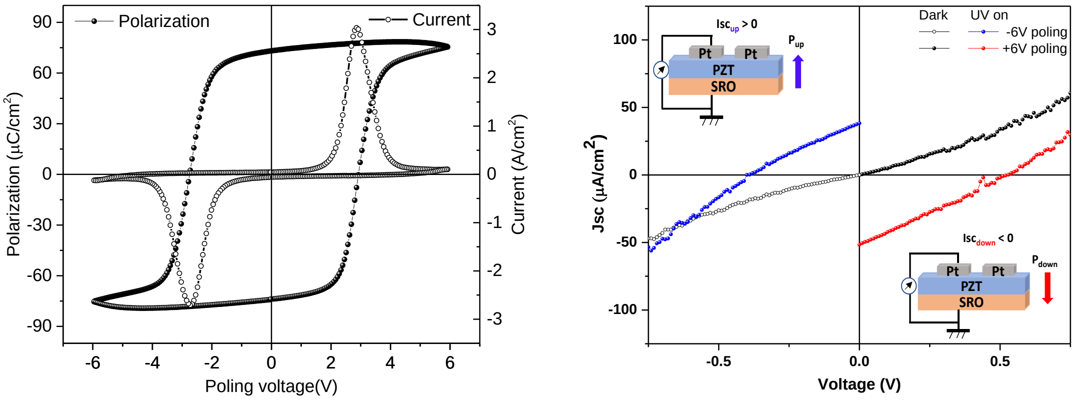

Graphique 1. a) Cycle d’hystérésis ferroélectrique typique, b) Mesure de photocourant dans l’obscurité et sous éclairement UV pour des états de polarisation haut et bas (sans comportement commutable à 100%).

La quatrième partie de cette thèse présente une étude quantitative de la relation entre la polarisation rémanente et le photocourant de court-circuit dans un dispositif Pt/PZT (100nm)/SRO à l’aide d’un protocole conçu pour des états de polarisation rémanente intermédiaires écrits électriquement et stables. Le lien entre l’état de polarisation et le courant de court-circuit est démontré de manière convaincante : où le photocourant (Jsc) montre une relation linéaire en fonction de la polarisation rémanente (Pr) (présenté dans la figure 2), et l’examen quantitatif de ces résultats ont révélé la présence d’une composante bloquée de polarisation dans la couche, désignée comme polarisation non commutable ($P_{NS} = 12 \mu C/cm^2$), ce qui a un impact sur la commutation des photocourants. Bien que la relation linéaire ne puisse pas être utilisée pour déterminer l’origine physique du photocourant (qui peut être lié au mécanisme PV bulk ou induit par un champ dépolarisant), la méthode établie peut être utilisée pour révéler une partie de polarisation non commutable dans une couche ferroélectrique. La polarisation bloquée pourrait être liée à des défauts, en particulier aux interfaces des électrodes. Le champ électrique dépolarisant (E_{dep} = 85 kV/cm) et l’efficacité d’écrantage (0,01%) peuvent être calculés quantitativement à partir de cette procédure de mesure de photocourant pour un ensemble spécifique d’électrodes inférieures et supérieures. Alors que le ccyle ferroélectrique traditionnel ne donne qu’une image limitée de la polarisation commutable, cette étude fournit des informations essentielles sur le comportement ferroélectrique dans toutes sortes de couches ferroélectriques et la dépendance à la polarisation du photocourant pourrait servir d’outil efficace pour caractériser la qualité de tout film ferroélectrique intégré dans un dispositif type condensateur.

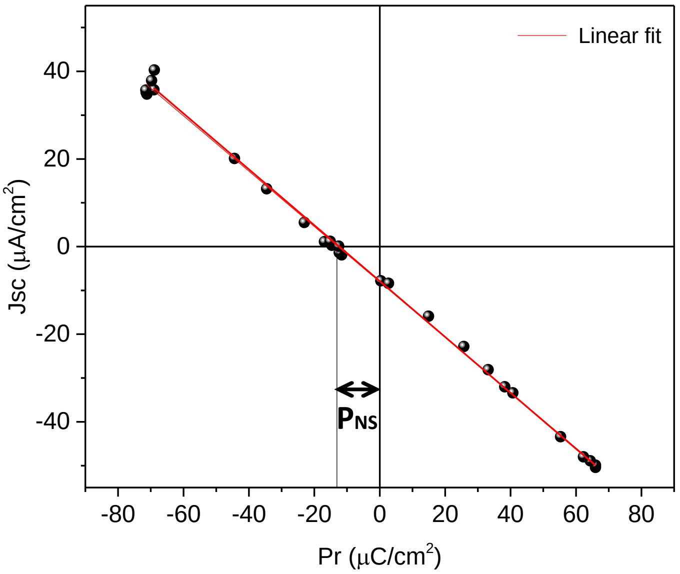

Graphique 2. Diagramme de la relation linéaire Jsc Vs Pr indiquant la présence d'une polarisation non commutable, P_{NS}.

La cinquième partie de ce travail étudie différents types de matériaux d'électrodes afin de déterminer comment ils peuvent affecter la partie de polarisation non commutable, et si différentes efficacités d'écrantage peuvent être atteintes et quantifiées. À cette fin, des dispositifs avec des interfaces asymétriques ont été fabriqués, à savoir (Pt, ITO/PZT) sur SRO, (Pt, ITO/PZT) sur LSMO et Pt/STO/PZT/SRO. Les mesures électriques sur tous ces dispositifs ont été réalisés de façon similaire, en suivant le protocole de mesures décrit au chapitre 4. Tous les dispositifs présentent une commutation de photocourant supérieure à 60%. Le message principal est que le cycle de polarisation ferroélectrique classique ne fournit aucune indication sur la réponse en photocourant attendue et la commutabilité de l'échantillon. Ce n'est qu'en mesurant quantitativement la dépendance du photocourant avec la polarisation que nous pouvons comprendre les propriétés PV d'un dispositif FE.

Les dispositifs présentant des électrodes supérieures de Pt ont été analysés à l'aide du protocole mentionné au chapitre 4. Pour les dispositifs à base de Pt, le cycle ferroélectrique est plus ou moins symétrique avec des fuites de courant négligeables, à l'exception du dispositif avec tampon supérieur de STO, pour lequel la contribution des fuites à la polarisation a pu être supprimée à l'aide de notre protocole d'application d'impulsions de tension. Ces résultats pour les dispositifs Pt sont cohérents avec les résultats présentés au chapitre 4 sur un autre dispositif Pt/PZT/SRO (utilisant une autre cible PZT). Les valeurs moyennes de Jsc et de Voc se situent dans la même plage. La plus grande commutabilité du photocourant a été mesurée dans le dispositif avec la couche tampon supérieure de STO. La part de polarisation non écrantée extraite dans ces dispositifs est de l'ordre de 1,2% à 2%. Pour tous les dispositifs Pt, une composante de polarisation non commutable est mise en évidence, induisant un champ électrique vers le haut (similaire à l'étude du chapitre 4) et expliquant pourquoi le photocourant n’est pas commutable à 100% et pourquoi le courant est plus élevé dans l’état de polarisation vers le bas. Il convient de souligner ici que la polarisation non commutable n’est pas liée au retournement rapide de domaines très mobiles qui pourrait être induit par un décalage du cycle d’hystérésis, car le cycle d’hystérésis présente des valeurs similaires de polarisation rémanente (Pr) pour les deux directions de polarisation. On peut alors parler de polarisation bloquée qui n’est pas sondée par les mesures d’hystérésis ferroélectrique mais révélée par les mesures de photocourant. Notez que l’origine de cette part de polarisation bloquée dépasse le cadre de cette étude et mériterait plus d’investigation. Elle pourrait être liée à une distribution inhomogène des défauts chargés dans le film et/ou à l’asymétrie entre les barrières de potentiel pour les porteurs de charge mobiles aux interfaces inférieure et supérieure.

Dans le cas des dispositifs à base d’ITO, le cycle ferroélectrique est décalé vers les tensions positives, indiquant un champ de décalage vers l’électrode haute. Cependant, la commutation de photocourant peut atteindre 87% dans le dispositif SRO / PZT / ITO. Un photocourant plus élevé a été obtenu dans l’état de polarisation bas pour les deux dispositifs ITO (dans la direction opposée par rapport aux résultats des dispositifs Pt) et cette asymétrie mesurée entre le photocourant dans les états de polarisation haut et bas ne semble pas être liée au champ de décalage. Le photocourant plus élevé dans l’état de polarisation haut pourrait être lié à une certaine contribution de l’effet de la barrière Schottky, car la barrière de potentiel à l’interface PZT / ITO est très différente de celle PZT / Pt, d’après les mesures effectuées avec les deux dispositifs sur le même film PZT. Il n’a pas été possible d’extraire avec précision les valeurs de polarisation rémanente Pr en raison de l’énorme contribution des courants de fuite, même en utilisant le protocole de mesures, nous empêchant d’étudier quantitativement la dépendance du photocourant avec la polarisation dans les dispositifs ITO.

En fin de compte, la thèse a été conclue au chapitre 6 avec des perspectives futures mentionnant que plus de recherche est nécessaire pour comprendre les paramètres influençant le photocourant et l’efficacité d’écrantage de la polarisation, incluant les conditions de croissance et la température. Aussi, il est crucial d’étudier plus en détails le mécanisme de génération du photocourant ainsi que l’efficacité d’écrantage de la polarisation aux interfaces grâce à l’optimisation des dispositifs passant par un choix avisé des électrodes et des hétérostructures. Par exemple, l’utilisation d’électrodes supérieures LSMO ou SRO pour construire une hétérostructure tout oxyde serait intéressante à étudier.

Les résultats présentés suite à ce travail de recherche dans le domaine du photovoltaïque dans les ferroélectriques fournissent une approche générale pour étudier et optimiser la commutabilité du photocourant, ce qui pourrait avoir des implications de grande portée pour les futures applications de mémoires photo-ferroélectriques.

Bibliography

[1] Paillard C, Bai X, Infante I C, Guennou M, Geneste G, Alexe M, Kreisel J and Dkhil B 2016 Photovoltaics with Ferroelectrics: Current Status and Beyond *Advanced Materials* **28** 5153–68

[2] Micheron F 1978 Dependence of the photovoltaic effect upon polarization in oxygen octaedra ferroelectrics *Ferroelectrics* **21** 607–9

[3] Lee D, Baek S H, Kim T H, Yoon J-G, Folkman C M, Eom C B and Noh T W 2011 Polarity control of carrier injection at ferroelectric/metal interfaces for electrically switchable diode and photovoltaic effects *Phys. Rev. B* **84** 125305

[4] Pintilie L, Vrejoiu I, Le Rhun G and Alexe M 2007 Short-circuit photocurrent in epitaxial lead zirconate-titanate thin films *Journal of Applied Physics* **101** 064109

[5] Yang Y S, Lee S J, Yi S, Chae B G, Lee S H, Joo H J and Jang M S 2000 Schottky barrier effects in the photocurrent of sol–gel derived lead zirconate titanate thin film capacitors *Appl. Phys. Lett.* **76** 774–6

[6] Cheng S, Fan Z, Zhao L, Guo H, Zheng D, Chen Z, Guo M, Jiang Y, Wu S, Zhang Z, Gao J, Lu X, Zhou G, Gao X and Liu J-M 2019 Enhanced photovoltaic efficiency and persisted photoresponse switchability in $LaVO_3/Pb(Zr_{0.2}Ti_{0.8})O_3$ perovskite heterostructures *J. Mater. Chem. C* **7** 12482–90

[7] Wu L, Burger A M, Bennett-Jackson A L, Spanier J E and Davies P K 2021 Polarization-Modulated Photovoltaic Effect at the Morphotropic Phase Boundary in Ferroelectric Ceramics *Adv. Electron. Mater.* **7** 2100144

[8] Belhadi J, Yousfi S, El Marssi M, Arnold D C and Bouyanfif H 2020 Tailoring the photovoltaic effect in (1 1 1) oriented $BiFeO_3/LaFeO_3$ superlattices *J. Phys.: Condens. Matter* **32** 135301

[9] Pintilie L 2011 Charge Transport in Ferroelectric Thin Films *Ferroelectrics - Physical Effects* ed M Lallart (InTech)

[10] Fang L, You L, Zhou Y, Ren P, Shiuh Lim Z and Wang J 2014 Switchable photovoltaic response from polarization modulated interfaces in $BiFeO_3$ thin films *Appl. Phys. Lett.* **104** 142903

[11] Gao R L, Yang H W, Chen Y S, Sun J R, Zhao Y G and Shen B G 2014 Oxygen vacancies induced switchable and nonswitchable photovoltaic effects in $Ag/Bi_{0.9}La_{0.1}FeO_3/La_{0.7}Sr_{0.3}MnO_3$ sandwiched capacitors *Appl. Phys. Lett.* **104** 031906

[12] Bai Z, Geng W, Zhang Y, Xu S, Guo H and Jiang A 2017 The abnormal photovoltaic effect in BiFeO3 thin films modulated by bipolar domain orientations and oxygen-vacancy migration *Appl. Phys. A* **123** 561

[13] Fridkin V M 1979 *Photoferroelectrics* (Berlin, Heidelberg: Springer Berlin Heidelberg)

[14] Lines M E and Glass A M 2001 *Principles and Applications of Ferroelectrics and Related Materials* (Oxford University Press)

[15] Uchino K 2010 *Ferroelectric devices* (Boca Raton: CRC Press)

[16] Valasek J 1921 Piezo-Electric and Allied Phenomena in Rochelle Salt *Phys. Rev.* **17** 475–81

[17] Wadhawan V 2000 *Introduction to Ferroic Materials* (CRC Press)

[18] Scott J F 2000 *Ferroelectric Memories* vol 3 (Berlin, Heidelberg: Springer Berlin Heidelberg)

[19] Uchino K 2010 *Ferroelectric devices* (Boca Raton: CRC Press)

[20] Chynoweth A G 1956 Surface Space-Charge Layers in Barium Titanate *Phys. Rev.* **102** 705–14

[21] Fridkin V M, Grekov A A, Kosonogov N A and Volk T R 1972 Photodomain effect in BaTiO3 *Ferroelectrics* **4** 169–75

[22] Glass A M, von der Linde D and Negran T J 1974 High-voltage bulk photovoltaic effect and the photorefractive process in LiNbO $_3$ *Appl. Phys. Lett.* **25** 233–5

[23] Tatsuzaki I, Itoh K, Ueda S and Shindo Y 1966 Strain Along c Axis of SbSI Caused by Illumination in dc Electric Field *Phys. Rev. Lett.* **17** 198–200

[24] Brody P S 1983 Optomechanical bimorph actuator *Ferroelectrics* **50** 27–32

[25] Poosanaas P, Tonooka K and Uchino K 2000 Photostrictive actuators *Mechatronics* **10** 467–87

[26] Kundys B, Viret M, Colson D and Kundys D O 2010 Light-induced size changes in BiFeO3 crystals *Nature Mater* **9** 803–5

[27] Kundys B 2015 Photostrictive materials *Applied Physics Reviews* **2** 011301

[28] Paillard C, Bai X, Infante I C, Guennou M, Geneste G, Alexe M, Kreisel J and Dkhil B 2016 Photovoltaics with Ferroelectrics: Current Status and Beyond *Advanced Materials* **28** 5153–68

[29] Lee D, Baek S H, Kim T H, Yoon J-G, Folkman C M, Eom C B and Noh T W 2011 Polarity control of carrier injection at ferroelectric/metal interfaces for electrically switchable diode and photovoltaic effects *Phys. Rev. B* **84** 125305

[30] Matzen S, Guillemot L, Maroutian T, Patel S K K, Wen H, DiChiara A D, Agnus G, Shpyrko O G, Fullerton E E, Ravelosona D, Lecoeur P and Kukreja R 2019 Tuning Ultrafast Photoinduced Strain in Ferroelectric-Based Devices *Adv. Electron. Mater.* **5** 1800709

[31] Guo R, You L, Zhou Y, Shiuh Lim Z, Zou X, Chen L, Ramesh R and Wang J 2013 Non-volatile memory based on the ferroelectric photovoltaic effect *Nat Commun* **4** 1990

[32] Setter N, Damjanovic D, Eng L, Fox G, Gevorgian S, Hong S, Kingon A, Kohlstedt H, Park N Y, Stephenson G B, Stolitchnov I, Taganstev A K, Taylor D V, Yamada T and Streiffer S 2006 Ferroelectric thin films: Review of materials, properties, and applications *Journal of Applied Physics* **100** 051606

[33] Jaffe B 2014 *Piezoelectric Ceramics.* (Saint Louis: Elsevier Science)

[34] Noheda B, Cox D E, Shirane G, Gonzalo J A, Cross L E and Park S-E 1999 A monoclinic ferroelectric phase in the Pb(Zr1−xTix)O3 solid solution *Appl. Phys. Lett.* **74** 2059–61

[35] Noheda B 2000 The monoclinic phase in PZT: New light on morphotropic phase boundaries *AIP Conference Proceedings* Fundamental physics of ferroelectrics 2000 vol 535 (Aspen, Colorado (USA): AIP) pp 304–13

[36] Ragini, Ranjan R, Mishra S K and Pandey D 2002 Room temperature structure of Pb(ZrxTi1−xO3) around the morphotropic phase boundary region: A Rietveld study *Journal of Applied Physics* **92** 3266–74

[37] Bouzid A, Bourim E M, Gabbay M and Fantozzi G 2005 PZT phase diagram determination by measurement of elastic moduli *Journal of the European Ceramic Society* **25** 3213–21

[38] Guillemot L and Lecoeur P 2018 *Dynamics and engineering of photostriction in microdevices based on epitaxial ferroelectric oxides thin films, Dynamique et ingénierie de la photostriction dans des microdispositifs à base de films minces épitaxiés d'oxydes ferroélectriques* (Université Paris Saclay (COmUE))

[39] Sze S M 1981 *Physics of semiconductor devices* (New York, N.Y.: Wiley)

[40] Filip L D and Pintilie L 2016 Metal-ferroelectric-metal current-voltage characteristics: A charge flow balance through interfaces approach *Eur. Phys. J. B* **89** 44

[41] Pintilie L and Alexe M 2005 Metal-ferroelectric-metal heterostructures with Schottky contacts. I. Influence of the ferroelectric properties *Journal of Applied Physics* **98** 124103

[42] Pintilie L, Boerasu I, Gomes M J M, Zhao T, Ramesh R and Alexe M 2005 Metal-ferroelectric-metal structures with Schottky contacts. II. Analysis of the experimental current-voltage and capacitance-voltage characteristics of Pb(Zr,Ti)O3 thin films *Journal of Applied Physics* **98** 124104

[43] von Baltz R and Kraut W 1981 Theory of the bulk photovoltaic effect in pure crystals *Phys. Rev. B* **23** 5590–6

[44] Shockley W and Queisser H J 1961 Detailed Balance Limit of Efficiency of *p-n* Junction Solar Cells *Journal of Applied Physics* **32** 510–9

[45] Fridkin V M and Popov B N 1978 Anomalous photovoltaic effect in ferroelectrics *Sov. Phys. Usp.* **21** 981–91

[46] Belinicher V I and Sturman B I 1980 The photogalvanic effect in media lacking a center of symmetry *Sov. Phys. Usp.* **23** 199–223

[47] Zenkevich A, Matveyev Yu, Maksimova K, Gaynutdinov R, Tolstikhina A and Fridkin V 2014 Giant bulk photovoltaic effect in thin ferroelectric BaTiO 3 films *Phys. Rev. B* **90** 161409

[48] Gu Z, Imbrenda D, Bennett-Jackson A L, Falmbigl M, Podpirka A, Parker T C, Shreiber D, Ivill M P, Fridkin V M and Spanier J E 2017 Mesoscopic Free Path of Nonthermalized Photogenerated Carriers in a Ferroelectric Insulator *Phys. Rev. Lett.* **118** 096601

[49] Chen F S 1969 Optically Induced Change of Refractive Indices in LiNbO $_3$ and LiTaO $_3$ *Journal of Applied Physics* **40** 3389–96

[50] Qin M, Yao K, Liang Y C and Shannigrahi S 2007 Thickness effects on photoinduced current in ferroelectric (Pb0.97La0.03)(Zr0.52Ti0.48)O3 thin films *Journal of Applied Physics* **101** 014104

[51] Fridkin V M 2001 Bulk photovoltaic effect in noncentrosymmetric crystals *Crystallogr. Rep.* **46** 654–8

[52] Sturman B I and Fridkin V M 1992 *The photovoltaic and photorefractive effects in noncentrosymmetric materials* (Philadelphia: Gordon and Breach Science Publishers)

[53] Kraut W and von Baltz R 1979 Anomalous bulk photovoltaic effect in ferroelectrics: A quadratic response theory *Phys. Rev. B* **19** 1548–54

[54] Glass A M, von der Linde D and Negran T J 1974 High-voltage bulk photovoltaic effect and the photorefractive process in LiNbO $_3$ *Appl. Phys. Lett.* **25** 233–5

[55] Moubah R, Rousseau O, Colson D, Artemenko A, Maglione M and Viret M 2012 Photoelectric Effects in Single Domain BiFeO $_3$ Crystals *Adv. Funct. Mater.* **22** 4814–8

[56] Mehta R R, Silverman B D and Jacobs J T 1973 Depolarization fields in thin ferroelectric films *Journal of Applied Physics* **44** 3379–85

[57] Batra I P, Wurfel P and Silverman B D 1973 Phase Transition, Stability, and Depolarization Field in Ferroelectric Thin Films *Phys. Rev. B* **8** 3257–65

[58] Wurfel P and Batra I P 1973 Depolarization-Field-Induced Instability in Thin Ferroelectric Films—Experiment and Theory *Phys. Rev. B* **8** 5126–33

[59] Qin M, Yao K and Liang Y C 2008 High efficient photovoltaics in nanoscaled ferroelectric thin films *Appl. Phys. Lett.* **93** 122904

[60] Qin M, Yao K and Liang Y C 2009 Photovoltaic mechanisms in ferroelectric thin films with the effects of the electrodes and interfaces *Applied Physics Letters* **95** 022912

[61] Pintilie L 2011 Charge Transport in Ferroelectric Thin Films *Ferroelectrics - Physical Effects* ed M Lallart (InTech)

[62] Yi H T, Choi T, Choi S G, Oh Y S and Cheong S-W 2011 Mechanism of the Switchable Photovoltaic Effect in Ferroelectric BiFeO3 *Adv. Mater.* **23** 3403–7

[63] Yuan Y, Xiao Z, Yang B and Huang J 2014 Arising applications of ferroelectric materials in photovoltaic devices *J. Mater. Chem. A* **2** 6027–41

[64] Zheng F, Xu J, Fang L, Shen M and Wu X 2008 Separation of the Schottky barrier and polarization effects on the photocurrent of Pt sandwiched Pb(Zr0.20Ti0.80)O3 films *Appl. Phys. Lett.* **93** 172101

[65] Yang S Y, Seidel J, Byrnes S J, Shafer P, Yang C-H, Rossell M D, Yu P, Chu Y-H, Scott J F, Ager J W, Martin L W and Ramesh R 2010 Above-bandgap voltages from ferroelectric photovoltaic devices *Nature Nanotech* **5** 143–7

[66] Seidel J, Fu D, Yang S-Y, Alarcón-Lladó E, Wu J, Ramesh R and Ager J W 2011 Efficient Photovoltaic Current Generation at Ferroelectric Domain Walls *Phys. Rev. Lett.* **107** 126805

[67] Alexe M and Hesse D 2011 Tip-enhanced photovoltaic effects in bismuth ferrite *Nat Commun* **2** 256

[68] Choi T, Lee S, Choi Y J, Kiryukhin V and Cheong S-W 2009 Switchable Ferroelectric Diode and Photovoltaic Effect in BiFeO $_3$ *Science* **324** 63–6

[69] Bhatnagar A, Roy Chaudhuri A, Heon Kim Y, Hesse D and Alexe M 2013 Role of domain walls in the abnormal photovoltaic effect in BiFeO3 *Nat Commun* **4** 2835

[70] Liu F, Fina I, Gutiérrez D, Radaelli G, Bertacco R and Fontcuberta J 2015 Selecting Steady and Transient Photocurrent Response in BaTiO $_3$ Films *Advanced Electronic Materials* **1** 1500171

[71] Yang Y, Xu W, Xu X, Wang Y, Yuan G, Wang Y and Liu Z 2016 The enhanced photocurrent of epitaxial BiFeO $_3$ film at 130 °C *Journal of Applied Physics* **119** 044102

[72] Yao K, Gan B K, Chen M and Shannigrahi S 2005 Large photo-induced voltage in a ferroelectric thin film with in-plane polarization *Appl. Phys. Lett.* **87** 212906

[73] Micheron F 1978 Dependence of the photovoltaic effect upon polarization in oxygen octaedra ferroelectrics *Ferroelectrics* **21** 607–9

[74] Thakoor S and Maserjian J 1994 Photoresponse probe of the space charge distribution in ferroelectric lead zirconate titanate thin film memory capacitors *Journal of Vacuum Science & Technology A* **12** 295–9

[75] Kholkin A, Boiarkine O and Setter N 1998 Transient photocurrents in lead zirconate titanate thin films *Applied Physics Letters* **72** 130–2

[76] Blom P W M, Wolf R M, Cillessen J F M and Krijn M P C M 1994 Ferroelectric Schottky Diode *Phys. Rev. Lett.* **73** 2107–10

[77] Yuan G-L and Wang J 2009 Evidences for the depletion region induced by the polarization of ferroelectric semiconductors *Appl. Phys. Lett.* **95** 252904

[78] Ge C, Jin K-J, Wang C, Lu H-B, Wang C and Yang G-Z 2011 Numerical investigation into the switchable diode effect in metal-ferroelectric-metal structures *Appl. Phys. Lett.* **99** 063509

[79] Ge C, Wang C, Jin K, Lu H and Yang G 2013 Recent Progress in Ferroelectric Diodes: Explorations in Switchable Diode Effect *Nano-Micro Lett.* **5** 81–7

[80] Nechache R, Harnagea C, Licoccia S, Traversa E, Ruediger A, Pignolet A and Rosei F 2011 Photovoltaic properties of Bi2FeCrO6 epitaxial thin films *Appl. Phys. Lett.* **98** 202902

[81] Cheng S, Fan Z, Zhao L, Guo H, Zheng D, Chen Z, Guo M, Jiang Y, Wu S, Zhang Z, Gao J, Lu X, Zhou G, Gao X and Liu J-M 2019 Enhanced photovoltaic efficiency and persisted photoresponse switchability in $LaVO_3$ /$Pb(Zr_{0.2}Ti_{0.8})O_3$ perovskite heterostructures *J. Mater. Chem. C* **7** 12482–90

[82] Poosanaas P, Dogan A, Thakoor S and Uchino K 1998 Influence of sample thickness on the performance of photostrictive ceramics *Journal of Applied Physics* **84** 1508–12

[83] Yarmarkin V K, Gol'tsman B M, Kazanin M M and Lemanov V V 2000 Barrier photovoltaic effects in PZT ferroelectric thin films *Phys. Solid State* **42** 522–7

[84] Xing J, Jin K-J, Lu H, He M, Liu G, Qiu J and Yang G 2008 Photovoltaic effects and its oxygen content dependence in BaTiO3−δ/Si heterojunctions *Appl. Phys. Lett.* **92** 071113

[85] Shuai Y, Zhou S, Bürger D, Reuther H, Skorupa I, John V, Helm M and Schmidt H 2011 Decisive role of oxygen vacancy in ferroelectric versus ferromagnetic Mn-doped $BaTiO_3$ thin films *Journal of Applied Physics* **109** 084105

[86] Yang M, Bhatnagar A and Alexe M 2015 Electronic Origin and Tailoring of Photovoltaic Effect in $BiFeO_3$ Single Crystals *Adv. Electron. Mater.* **1** 1500139

[87] Piskunov S, Heifets E, Eglitis R I and Borstel G 2004 Bulk properties and electronic structure of SrTiO3, BaTiO3, PbTiO3 perovskites: an ab initio HF/DFT study *Computational Materials Science* **29** 165–78

[88] Nechache R, Harnagea C, Li S, Cardenas L, Huang W, Chakrabartty J and Rosei F 2015 Bandgap tuning of multiferroic oxide solar cells *Nature Photon* **9** 61–7

[89] Grinberg I, West D V, Torres M, Gou G, Stein D M, Wu L, Chen G, Gallo E M, Akbashev A R, Davies P K, Spanier J E and Rappe A M 2013 Perovskite oxides for visible-light-absorbing ferroelectric and photovoltaic materials *Nature* **503** 509–12

[90] Kawasaki M, Takahashi K, Maeda T, Tsuchiya R, Shinohara M, Ishiyama O, Yonezawa T, Yoshimoto M and Koinuma H 1994 Atomic Control of the SrTiO3 Crystal Surface *Science* **266** 1540–2

[91] Kim S S, Kang T S and Je J H 2001 Structural evolution of epitaxial SrRuO3 thin films grown on SrTiO3(001) *Journal of Applied Physics* **90** 4407–10

[92] Španková M, Štrbík V, Chromik Š, Zheng D N, Li J, Machajdík D, Kobzev A P, Plecenik T and Sojková M 2017 Characterization of Epitaxial LSMO Films Grown on STO Substrates *Acta Phys. Pol. A* **131** 848–50

[93] Dawber M, Rabe K M and Scott J F 2005 Physics of thin-film ferroelectric oxides *Rev. Mod. Phys.* **77** 1083–130

[94] Everhardt A S, Noheda Pinuaga B, Rijksuniversiteit Groningen, and Zernike Institute for Advanced Materials (Groningen) 2017 *Novel phases in ferroelectric in BaTiO3 thin films: enhanced piezoelectricity and low hysteresis*

[95] Hiboux S, Muralt P and Maeder T 1999 Domain and lattice contributions to dielectric and piezoelectric properties of Pb(Zr x , Ti $_{1-x}$)O $_3$ thin films as a function of composition *J. Mater. Res.* **14** 4307–18

[96] Zenkevich A, Matveyev Yu, Maksimova K, Gaynutdinov R, Tolstikhina A and Fridkin V 2014 Giant bulk photovoltaic effect in thin ferroelectric BaTiO 3 films *Phys. Rev. B* **90** 161409

[97] Rani K, Matzen S, Gable S, Maroutian T, Agnus G and Lecoeur P 2021 Quantitative investigation of polarization-dependent photocurrent in ferroelectric thin films *J. Phys.: Condens. Matter*

[98] Pintilie L, Vrejoiu I, Le Rhun G and Alexe M 2007 Short-circuit photocurrent in epitaxial lead zirconate-titanate thin films *Journal of Applied Physics* **101** 064109

[99] Yang Y S, Lee S J, Yi S, Chae B G, Lee S H, Joo H J and Jang M S 2000 Schottky barrier effects in the photocurrent of sol–gel derived lead zirconate titanate thin film capacitors *Appl. Phys. Lett.* **76** 774–6

[100] Wu L, Burger A M, Bennett-Jackson A L, Spanier J E and Davies P K 2021 Polarization-Modulated Photovoltaic Effect at the Morphotropic Phase Boundary in Ferroelectric Ceramics *Adv. Electron. Mater.* **7** 2100144

[101] Cao D, Zhang H, Fang L, Dong W, Zheng F and Shen M 2011 Polarization effect on the photocurrent of Pt sandwiched multi-crystalline ferroelectric films *Materials Chemistry and Physics* **129** 783–6

[102] Quattropani A, Makhort A S, Rastei M V, Versini G, Schmerber G, Barre S, Dinia A, Slaoui A, Rehspringer J-L, Fix T, Colis S and Kundys B 2018 Tuning photovoltaic response in Bi $_2$ FeCrO $_6$ films by ferroelectric poling *Nanoscale* **10** 13761–6

[103] Liu F, Fina I, Gutiérrez D, Radaelli G, Bertacco R and Fontcuberta J 2015 Selecting Steady and Transient Photocurrent Response in BaTiO $_3$ Films *Advanced Electronic Materials* **1** 1500171

[104] Setter N, Damjanovic D, Eng L, Fox G, Gevorgian S, Hong S, Kingon A, Kohlstedt H, Park N Y, Stephenson G B, Stolitchnov I, Taganstev A K, Taylor D V, Yamada T and Streiffer S 2006 Ferroelectric thin films: Review of materials, properties, and applications *Journal of Applied Physics* **100** 051606

[105] Mehta R R, Silverman B D and Jacobs J T 1973 Depolarization fields in thin ferroelectric films *Journal of Applied Physics* **44** 3379–85

[106] Batra I P, Wurfel P and Silverman B D 1973 Phase Transition, Stability, and Depolarization Field in Ferroelectric Thin Films *Phys. Rev. B* **8** 3257–65

[107] Glinchuk M D, Zaulychny B Y and Stephanovich V A 2005 Depolarization Field in Thin Ferroelectric Films With Account of Semiconductor Electrodes *Ferroelectrics* **316** 1–6

[108] Han M-G, Marshall M S J, Wu L, Schofield M A, Aoki T, Twesten R, Hoffman J, Walker F J, Ahn C H and Zhu Y 2014 Interface-induced nonswitchable domains in ferroelectric thin films *Nat Commun* **5** 4693

[109] Dimos D, Warren W L, Sinclair M B, Tuttle B A and Schwartz R W 1994 Photoinduced hysteresis changes and optical storage in (Pb,La)(Zr,Ti)O_3 thin films and ceramics *Journal of Applied Physics* **76** 4305–15

[110] Kholkin A L, Iakovlev S O and Baptista J L 2001 Direct effect of illumination on ferroelectric properties of lead zirconate titanate thin films *Appl. Phys. Lett.* **79** 2055–7

[111] Scott J F 1999 Device Physics of Ferroelectric Thin-Film Memories *Jpn. J. Appl. Phys.* **38** 2272–4

[112] Park Y, Choong V, Gao Y, Hsieh B R and Tang C W 1996 Work function of indium tin oxide transparent conductor measured by photoelectron spectroscopy *Appl. Phys. Lett.* **68** 2699–701

[113] Kudo T, Tachiki M, Kashiwai T and Kobayashi T 1998 Band Diagram of Metal-Insulator-Magnetic Semiconductor (La0.85Sr0.15MnO3) Structure at Room Temperature *Jpn. J. Appl. Phys.* **37** L999–1001

[114] Guillemot L and Lecoeur P 2018 *Dynamics and engineering of photostriction in microdevices based on epitaxial ferroelectric oxides thin films, Dynamique et ingénierie de la photostriction dans des microdispositifs à base de films minces épitaxiés d'oxydes ferroélectriques* (Université Paris Saclay (COmUE))